MURINE *IN VITRO* MODEL OF THE BLOOD-BRAIN BARRIER USING A NANOFABRICATED POLY(HYDROXY STYRENE) MEMBRANE AND IDENTIFICATION OF THERAPEUTIC BIOMARKERS OF ALZHEIMER'S DISEASE IN RELATION TO INTRAVENOUS IMMUNOGLOBULIN THERAPY

A Dissertation

Presented to the Faculty of the Graduate School

of Cornell University

In Partial Fulfillment of the Requirements for the Degree of

Doctor of Philosophy

by

Gilda Shayan

May 2010

MURINE *IN VITRO* MODEL OF THE BLOOD-BRAIN BARRIER USING A NANOFABRICATED POLY(HYDROXY STYRENE) MEMBRANE AND IDENTIFICATION OF THERAPEUTIC BIOMARKERS OF ALZHEIMER'S DISEASE IN RELATION TO INTRAVENOUS IMMUNOGLOBULIN THERAPY

Gilda Shayan, Ph.D.

Cornell University 2010

Currently, there are over 5.3 million people in the United States diagnosed with Alzheimer's disease, with the disease being the sixth leading cause of death in the country. Current drugs on the market for the treatment of Alzheimer's disease are lipophilic small molecules that cross the blood-brain barrier by passive diffusion and none have been clinically useful in reversing the symptoms of the disease. Immunotherapy with intravenous immunoglobulin (IVIg) is one of several treatment strategies now being studied as part of efforts to discover safe and more effective treatment paradigms for Alzheimer's disease.

In 2005, Weill Cornell Medical College initiated the phase I clinical trial of IVIg for the treatment of Alzheimer's disease, and the clinical outcomes indicated improvements in the cognitive abilities of subjects beyond expectations. This dissertation will address combining proteomics and statistical approaches with novel designs for *in vitro* blood-brain barrier models with an attempt to understand the molecular basis for the disease-modifying effects of IVIg in Alzheimer's disease.

The first part of the thesis focuses on the development of a new *in vitro* model of the blood-brain barrier based on a co-culture between primary mouse

brain microvascular endothelial cells and primary rat astrocytes on commercially available polyester membranes and nanofabricated poly(hydroxyl styrene) membranes. This model serves as a successful platform technology for evaluating molecular transport across the blood-brain barrier. The permeability of central nervous system drugs across this *in vitro* model correlated well with *in* vivo data, with the correlation coefficient being 0.98. The second part of this thesis provides examples of proteomics approaches coupled with advanced statistical modeling that can be utilized to identify therapy induced biomarkers in the cerebrospinal fluid. Specifically, cerebrospinal fluid samples from Alzheimer's subjects who underwent IVIg immunotherapy were analyzed using gel-based proteomics and the results were analyzed using a statistical model to identify 25 therapeutically relevant biomarkers in response to IVIg. These proteins have been previously implicated in Alzheimer's disease and the changes in their concentration is consistent with previous reports regarding the expression of them in the brain of Alzheimer's subjects compared to normal individuals.

BIOGRAPHICAL SKETCH

Gilda was born in northern Tehran, Iran three hours prior to the Persian New Year on March, 1984. Even though her close family members shared a deep appreciation for mathematics and engineering, as a child she always dreamed of becoming a dentist and this dream further transformed into becoming a physician by the time she was in high school. While a biology major in high school, she became passionate about probability and statistics and how it relates to biology.

She immigrated to the United States at the age of seventeen and attended North Harris Community College in Houston, TX. She then transferred to Cornell University to pursue an undergraduate degree in Genetics at the College of Arts and Sciences. While the transition proved challenging, she thinks attending Cornell was the best decision she has ever made. She has never seen before the enormous enthusiasm and pride her community college Professors took in her when she was admitted to Cornell.

She started her undergraduate research in the laboratory of Dr. Timothy Huffaker in Molecular and Cell Biology, and by the time she was half-way through her studies, she realized that she performs best in an area that has a more immediate impact on healthcare. This marked the beginning to pursue a graduate degree in biomedical engineering. She took core mathematics and engineering classes side by side with genetics courses and graduated *cum laude* in December 2005. She later joined the laboratory of Professor Kelvin Lee at Department of Chemical Engineering as a research assistant working on a nanotechnology-based *in vitro* model of the blood-brain barrier inspired by a new treatment strategy for Alzheimer's disease. On August 2006,

Professor Lee kindly and generously admitted her as a Ph.D. candidate in Biomedical Engineering to his laboratory. She spent three years in Ithaca and finished her final year at Delaware Biotechnology Institute where Professor Lee has recently moved.

Gilda has immensely enjoyed working on her thesis project thanks to the support from her professors, Cornell community, and the interdisciplinary nature of her research. Besides from science and engineering, she is passionate about law and philosophy, political history, and music. She plays the piano professionally and hopes to start taking advanced lessons again after she graduates.

Dedicated to Iran's Young Participants in the Green Movement

ACKNOWLEDGMENTS

I would like to thank my thesis adviser, Professor Kelvin Lee, for his thoughtful advice, patience, and generous support. I am grateful and humbled to be mentored by such an extraordinary scientist who acknowledged my work and passion for studying biomedical engineering and helped me to become an independent scientist. I never hesitated to share all that I had on my mind with him so I want to specially thank him for having my back throughout graduate school. I also want to thank my committee members, Professor Michael Shuler for his advice and generous hosting when my group moved to the University of Delaware, and Professor Christopher Ober for his mentorship and reassurance on the nanofabrication aspects of my project. Special thanks go to Dr. Norman Relkin at Weil Medical College for useful discussions about Alzheimer's disease, and Professor Eric Shusta at University of Wisconsin for primary culture trainings.

Many individuals have contributed significantly to the completion of this project. I want to thank former and current Lee group members, especially Leila Choe for her fulltime support and valuable comments on my thesis, Dr. Yong Choi for his assistance on mass spectrometry, Jeffrey Foltz for his help with two-dimensional gels, and Dr. Erin Finehout for her previous work on two-dimensional gels. I also want to thank Dr. Stephanie Hammond and her husband for kindly allowing me to stay with them during the times of commute. I thank Shuler group members, Paula Miller for cell culture training and assistance, and Dr. Sarina Harris Ma for initiating the construction of *in vitro* BBB models on nanofabricated materials. Special thanks go to Ober group members, Dr. Nelson Felix, Dr. Margarita Chatzichristidi, and Jaewook Seok

for their contributions towards material synthesis and nanofabrication. Professor David Putnam, Dr. Sara Yazdi, and Dr. Sharon Wong have made significant contributions on material synthesis and characterization. I also want to acknowledge Cornell Nanofabrication Facility (CNF) staff members, Glenn Swan at Chemical Engineering Machine Shop, Anthony Condo at CCMR, Carol Bayles at CLC, and Professor James Booth at CSCU.

Completion of this project went beyond Biomedical and Chemical Engineering Departments at Cornell University. I thank Professor John Schimenti and Robert Munroe at the College of Veterinary Medicine, Professor William Shain and Dr. John Frampton at the Wadsworth Center, Dr. Angela Jones at University of Wisconsin-Madison, and Professor Ulhas Naik and Meghna Naik at University of Delaware all for contributions on primary cell culture and animal protocols.

Financial support was provided in part by the New York State Office for Science, Technology, and Academic Research (NYSTAR), the National Science Foundation through the Nanobiotechnology Center (NBTC-BDA12), the National Institute of Health (NIH R01 MH59926) and the Institute for the Study of Aging (ISOA 281001).

My friends have contributed tremendously to different aspects of my success in graduate school. Special thanks go to Dr. Shahriar Beigi for his insightful advice and support in the past four years. I thank Mrs. Parvin Mortazavi for the times we spent together at her house. Dr. Sara Yazdi, Dr. Behfar Ardehali, Emily Chandler, Daniel Brooks, Joseph Califano, and John Nguyen made Ithaca a fun place to be outside of the lab.

My dear grandmother, Mrs. Mehrangiz Manouchehri is largely responsible for who I am today. She is the most independent and graceful

person that I have known in my life and she has always been a source of motivation. My parents, Mehrnaz and Javad Shayan have made immense sacrifices to make my life experience better than theirs so I thank them for never denying me an opportunity, for always pushing me to be at my best, and for allowing me the freedom to make my own decisions. My sister, Golnaz has always been a source of motivation and she never denied me a chance to take the lead even though she is older than me. She has been a patient listener at hard times and my beautiful nephew, Koen has brought smile to my face at tough times, so I want to thank both for making life even better.

TABLE OF CONTENTS

Biographical Sketch **iii**

Dedication **v**

Acknowledgements **vi**

List of Figures **xv**

List of Tables **xvii**

List of Abbreviations **xviii**

Chapter 1 Introduction **1**

1.1 Background and Motivation 1

1.2 Project Goals 3

1.3 Scope of Work 3

References 5

Chapter 2 The Blood-Brain Barrier **10**

2.1 The Physiology of the BBB 10

2.2 The Role of BBB in Alzheimer's Disease 15

2.3 Static *In Vitro* Models of the BBB 17

2.4 Physical and Biological Limitations of Current Static BBB Models 18

References 21

Chapter 3 The Effects of Astrocytes on the Induction of Barrier Properties in Aortic Endothelial Cells **26**

3.1 Preface 26

3.2 Abstract 26

3.3 Introduction 27

3.4 Materials and Methods 30

3.4.1 Chemicals and Supplies 30

3.4.2 Isolation of Rat Astrocytes 31
3.4.3 Bovine Aortic Endothelial Cells (BAEC) 31
3.4.4 Isolation of Murine Brain Microvascular Endothelial Cells 32
3.4.5 Co-Culture Setup 33
3.4.6 Transendothelial Electrical Resistance Measurements 36
3.4.7 Fluorescein Sodium Permeability Measurements 36
3.4.8 Uptake of DiI-Ac-LDL 37
3.4.9 Immunocytochemistry 37
3.4.10 Statistical Analysis 38
3.5 Results 39
3.5.1 Effect of Cultivation Period on TEER 39
3.5.2 Effect of Astrocytes on TEER 39
3.5.3 Effect of Astrocytes on Permeability 43
3.5.4 Immunocytochemical Characterization 44
3.6 Discussion 44
3.7 Conclusion 50
3.8 Acknowledgements 51
References 52
Chapter 4 Synthesis and Characterization of High-Throughput Nanofabricated Poly(Hydroxy Styrene) Membranes for *In Vitro* Models of Barrier Tissue 55
4.1 Preface 55
4.2 Abstract 55
4.3 Introduction 56
4.4 Materials and Methods 58
4.4.1 Chemicals and Supplies 58

4.4.2 Polymer Synthesis 59
4.4.3 Polymer Characterization 59
4.4.4 Nanofabrication Process 61
4.4.5 Cell Culture Maintenance 63
4.4.6 Cell Culture on Nanofabricated Membranes 64
4.4.7 Immunocytochemistry 66
4.4.8 Cell Metabolism and Viability Assays 67
4.4.9 Flux Measurements 68
4.5 Results and Discussion 68
4.5.1 Synthesis and Characterization of PHOST 69
4.5.2 Characterization of Nanofabricated Membranes 71
4.5.3 Cell Viability, Rate of Metabolism, and Differentiation 77
4.5.4 Flow Resistance Across Nanofabricated Membranes 81
4.6 Conclusion 83
4.7 Acknowledgements 83
References 84
Chapter 5 Murine *In Vitro* Model of the Blood-Brain Barrier For Evaluating Drug Transport 87
5.1 Preface 87
5.2 Abstract 87
5.3 Introduction 88
5.4 Materials and Methods 90
5.4.1 Chemicals and Supplies 90
5.4.2 Polymer Synthesis 92
5.4.3 Nanofabrication Process 92
5.4.4 Isolation of Rat Astrocytes 94

5.4.5 Isolation of BMEC 94
5.4.6 Co-Culture Setup 97
5.4.7 Transendothelial Electrical Resistance Measurements 98
5.4.8 Sodium Fluorescein Permeability Measurements 98
5.4.9 Uptake of DiI-Ac-LDL 99
5.4.10 Immunocytochemistry 99
5.4.11 Western Blotting 100
5.4.12 *In Vitro* Drug Permeability Study 101
5.4.13 LC-MS Analysis 101
5.4.14 Statistical Analysis 103
5.5 Results 104
5.5.1 Immunocytochemical Characterization 104
5.5.2 Paracellular Permeability of the Co-Cultures 104
5.5.3 Expression of Transporters and Tight Junction Proteins 106
5.5.4 Drug Permeability and Correlation with In Vivo Data 112
5.6 Discussion 112
5.7 Acknowledgements 118
References 119
Chapter 6 Intravenous Immunoglobulin Immunotherapy in Autoimmune and Neurologic Diseases 123
6.1 Introduction 123
6.2 Components of IVIg 124
6.3 Mechanisms of Action of IVIg 125
6.3.1 Fc Receptor Mediated Effects 125
6.3.2 Anti-idiotypic Effects 125
6.3.3 Effects on Complement Proteins 126

6.3.4 Effects on the Cytokine Network 126
6.4 Protein Targets of IVIg in the CSF 127
6.4.1 Immunoprecipitation with Magnetic Beads 127
6.4.2 1D Gel Electrophoresis and Western Blot 130
6.4.3 2D Gel electrophoresis and Western Blot 133
6.5 Idiotypic Network Theory in Autoimmunity 136
6.6 Conclusion 139
6.7 Supplemental Methods 140
6.7.1 Immunoprecipitation with Dynabeads® 140
6.7.2 1D Western Blot 140
6.7.3 2D Western Blot 141
6.8 Acknowledgements 142
References 143
Chapter 7 Proteomic Analysis of Diagnostic Biomarkers for Alzheimer's Disease Related to Intravenous Immunoglobulin Therapy 148
7.1 Preface 148
7.2 Abstract 148
7.3 Introduction 149
7.4 Materials and Methods 151
7.4.1 Cerebrospinal Fluid Samples 151
7.4.2 Two-Dimensional Gel Electrophoresis 151
7.4.3 Statistical Analysis 153
7.5 Results 154
7.6 Discussion 158
7.7 Acknowledgements 160
References 161

Chapter 8 Effects of Intravenous Immunoglobulin on Cerebrospinal Fluid Proteome in Alzheimer's Disease **163**

8.1 Preface 163

8.2 Abstract 163

8.3 Introduction 164

8.4 Materials and Methods 166

8.4.1 Cerebrospinal Fluid Samples 166

8.4.2 2D Gel Electrophoresis 167

8.4.3 Statistical Analysis 169

8.4.4 Protein Identification 170

8.5 Results 171

8.6 Discussion 177

8.7 Acknowledgements 179

References 180

Chapter 9 Conclusions and Future Work **183**

9.1 Summary of Conclusions 186

9.2 Recommendations for Future Work 189

9.2.1 BMEC and Astrocyte Co-Cultures on Membrane with Larger Pores 189

9.2.2 Dynamic *In Vitro* Model of the BBB 190

9.2.3 Understanding the Disease-Modifying Effects of IVIg 191

9.3 Conclusions 191

References 193

LIST OF FIGURES

2.1 Cellular and Molecular Components of the BBB 11

2.2 Pathways Across the BBB 14

2.3 Involvement of the Neurovascular Unit in the Pathogenesis of AD 16

2.4 Transwell® Culture Systems 19

3.1 Schematic of Two Different BBB Models 34

3.2 Design of the In-house Multi-well Dish 35

3.3 TEER of BAEC and Astrocytes Over Time 40

3.4 TEER of Model 1 or Model 2 with BAEC or BMEC 41

3.5 Immunocytochemical Characterization of EC and Astrocytes 45

3.6 Immunocytochemistry of Occludin in BAEC and BMEC 46

4.1 Synthesis of PHOST 60

4.2 Nanofabrication Scheme 62

4.3 Cell Culture Support Device 65

4.4 ^{1}H-NMR Spectrum of Poly(*tert*-butoxy styrene) and PHOST 70

4.5 FTIR Spectra of Poly(tert-butoxy styrene) and PHOST 72

4.6 DSC Analysis of Poly(tert-butoxy styrene) and PHOST 73

4.7 TGA Analysis of Poly(tert-butoxy styrene) and PHOST 74

4.8 Top and Cross-Sectional Views of the Porous Membrane 76

4.9 Alamar Blue Assay Showing Cellular Rate of Metabolism on PHOST 79

4.10 Cell Attachment, Growth, and Differentiation on PHOST 80

4.11 Rate of Transport Across PHOST 82

5.1 Cell Culture Support Device 95

5.2 Immunocytochemical Characterization 105

5.3 TEER of BMEC and Astrocytes 107

5.4 Immunocytochemistry of Tight Junctions 110

5.5 Expression Levels of Tight Junction Proteins and Transporters 111

5.6 Drug permeability Correlation Studies 113

5.7 Astrocyte Foot Processes Clog 400 nm Pores 116

6.1 Immunoprecipitation of CSF 128

6.2 Reactivity of IVIg with CSF using 1D Western Blot 131

6.3 Reactivity of IVIg with CSF using 2D Western Blot 134

6.4 Network of Antibodies 137

7.1 Fraction of Votes for Each CSF Sample 155

7.2 Fraction of AD Classification Normalized with Baseline 157

8.1 2DE Gel of CSF from Subject #7 172

LIST OF TABLES

5.1 List of Drugs Selected for Transport Studies 102

5.2 Sodium Fluorescein Permeability 109

7.1 Dosing and Sample Collection Information 152

8.1 Dosing and Sample Collection Information 168

8.2 2DE Spots that Show a Consistent Change 173

8.3 2DE Spots that Show a Significant Change in %Volume 176

LIST OF ABBREVIATIONS

Intravenous Immunoglobulin	IVIg
Central Nervous System	CNS
Blood-Brain Barrier	BBB
Alzheimer's Disease	AD
Amyloid Beta	Aβ
Cerebrospinal Fluid	CSF
Two-Dimensional Gel Electrophoresis	2DE
Brain Microvascular Endothelial Cells	BMEC
Endothelial Cells	EC
Interstitial Fluid	ISF
Transendothelial Electrical Resistance	TEER
Cerebral Blood Flow	CBF
Poly(Hydroxy Styrene)	PHOST

CHAPTER 1

INTRODUCTION

1.1 Background and Motivation

The development of therapeutics for the central nervous system (CNS) is one of the most challenging areas in drug development. This is primarily because, in addition to all of the other complications one faces in developing new drugs targeting peripheral sites, one must also consider the blood-brain barrier (BBB) [1-2]. Among prevalent forms of dementia, Alzheimer's disease (AD) is the leading cause in the elderly and affects over 5.3 million people in the United States [3]. Drugs currently on the market for AD are traditionally small, relatively lipid-soluble compounds. These drugs cross the BBB by means of transmembrane diffusion and they are not very effective in penetrating deep into the brain tissue and treating the symptoms of AD. As a result, immunotherapy is one of several treatment strategies now being studied as part of efforts to discover safe and more effective means of treating AD [4].

Abundant evidence suggests that a key event in AD pathogenesis is the conversion of the amyloid beta (Aβ) peptide from soluble to aggregated forms in the brain [5-13]. Active immunization with the Aβ peptide has been shown to decrease brain Aβ deposition in transgenic mouse models of AD [14], and certain peripherally administered anti-Aβ antibodies were shown to mimic this effect (i.e. passive immunization) [15].

Intravenous immunoglobulin (IVIg) is derived from the pooled immunoglobulins of healthy human blood donors and thus contains higher titers of polyclonal anti-Aβ antibodies than is typically found in the plasma of

AD patients. In addition, IVIg has other effects that are potentially relevant to AD treatment including anti-inflammatory actions related to down-regulation of pro-inflammatory cytokines, blockage of the complement cascade, and an increase in the cerebrospinal fluid (CSF) IgG content [16]. Thus, although the initial rationale for the efficacy of IVIg in AD is the presence of antibodies against Aβ, there may exist other IVIg components that are able to cross the BBB and have disease-modifying effects.

IVIg immunotherapy as it stands today, may not be a practical treatment strategy for AD for several reasons. First, IVIg is an expensive therapeutic product because the blood sera obtained from over a thousand individuals should go through rounds of purification, pathogen elimination, and sterilization. Second, since IVIg is a blood product, it is subject to blood donor and availability limitations. Third, it is difficult to keep the composition of IVIg consistent among batches due to variations in donors' blood compositions. Thus, identifying therapeutically relevant biomarkers in IVIg with respect to AD and studying the pharmacodynamics and pharmacokinetics of these biomarkers can potentially lead to the identification and development of new drug targets that can reduce the cost of therapy, and improve the accessibility, quality, and consistency of care.

Discovering a molecular mechanism for the disease-modifying effects of IVIg in AD can be approached in two phases. The first phase involves identifying therapeutically relevant IVIg protein targets in the CSF. Current advances in proteomics provide ample opportunities to address this issue [17-21]. There have been a large number of studies that apply two-dimensional gel electrophoresis (2DE) to the study of neurologic disease for the discovery of biomarkers and in the understanding of mechanism in a general sense.

Specifically, 2DE coupled to state-of-the-art methods in mass spectrometry and advanced statistical models can be used to profile changes in protein expression that results from therapy [17].

The second phase involves studying the pharmacodynamics and pharmacokinetics of the identified target biomarkers. Since successful drug delivery to the central nervous system is highly dependent on the molecule's physico-chemical properties and its interaction with the BBB, *in vitro* model systems of the BBB have long been used for mechanistic studies and permeability screens [22-28]. Therefore, an *in vitro* BBB model can be an effective platform technology for initial pharmacodynamics and pharmacokinetics studies. While the existing *in vitro* model systems of the BBB have answered questions about the physiological, pathological, and pharmacological relevance of the BBB, a new generation of models is required to integrate knowledge of the physical, biochemical, and transport properties of the BBB together with the knowledge of the cell biology [29-43].

1.2 Project Goals

The objective of this research is two-fold: 1) To improve the utility of current *in vitro* BBB models for molecular transport studies using new biochemical and nanofabrication techniques, 2) To discover the therapeutic targets of the IVIg in CSF by analyzing samples from AD subjects who underwent IVIg immunotherapy, using a combination of proteomics and statistical approaches.

1.3 Scope of the Work

This dissertation is organized in two sections. Chapters 2-5 explain development of new techniques and technologies to build a new generation *in*

vitro model of the BBB that addresses some of the limitations associated with current models. This model establishes the platform for future studies of IVIg transport. Chapter 2 provides a brief introduction on the BBB physiology, the importance of BBB in neurodegenerative disorders, especially AD, and current *in vitro* models and their limitations. *In vitro* BBB models are either based on primary brain microvascular endothelial cells (BMEC) or peripheral endothelial cells (EC). Chapter 3 provides comprehensive data on a co-culture model between aortic EC and astrocytes as an attempt to bypass the labor intensive isolation of primary BMEC. This study found that aortic EC are not induced by astrocytes' soluble factors and so are not an appropriate cell line for *in vitro* BBB models. Chapters 4 and 5 are devoted to nanofabrication techniques and biochemical interventions used to address some of the limitations associated with current BBB models, respectively. In particular establishment of mouse primary BMEC will be discussed.

Chapters 6-8 are devoted to IVIg immunotherapy in AD and its disease-modifying effects. Chapter 6 provides an overview of IVIg immunotherapy and its applications in neurologic and autoimmune disorders. Furthermore, it proposes possible proteomics approaches to understand the disease-modifying mechanisms of IVIg in neurologic diseases by incorporating the immunology network theory [44]. Chapter 7 explains a statistical analysis of the effects of IVIg on a panel of previously identified diagnostic biomarkers of AD [21]. Chapter 8 aims to provide a proteomics and statistical framework to identify the IVIg-induced biomarkers in the CSF of AD subjects who underwent immunotherapy. Additional conclusions and recommendations for future work are presented in Chapter 9.

REFERENCES

1. Begley, D. J., 2007. Delivery of therapeutic agents to the central nervous system: the problems and the possibilities. *Pharmacol. Ther.* 104, 29-45.
2. Banks, W. A., 2008. Developing drugs that can cross the blood-brain barrier: applications to Alzheimer's disease. *BMC Neuroscience* 9 (Suppl 3), S2.
3. 2009. Alzheimer's Disease facts and figures. *Alzheimer's & Dementia* 5, 234-270.
4. Relkin, N. R., Szabo, P., Adamiak, B., *et al.*, 2008. 18-Month study of intravenous immunoglobulin for treatment of mild Alzheimer disease. *Neurobiology of Aging*, In press.
5. Deane, R., Zlokovic, B. V., 2007. Role of blood-brain barrier in the pathogenesis of Alzheimer's disease. *Curr. Alzheimer Res*. 4, 191-197.
6. Hardy, J., 2006. A hundred years of Alzheimer's disease research. *Neuron* 52, 3-13.
7. Iadecola, C., 2004. Neurovascular regulation in the normal brain and in Alzheimer's disease. *Nat. Rev. Neurosci*. 5, 347-360.
8. Lee, V. M., Balin, B. J., *et al.*, 1991. A major subunit of paiered helical filaments and derivatized forms of normal Tau. *Science* 251, 675-678.
9. Rovelet-Lecrux, A., *et al.*, 2006. App locus duplication causes autosomal dominant early-onset Alzheimer's disease with cerebral amyloid angiopathy. *Nat. Genet*. 38, 24-26.
10. Santacruz, K., Lewis, J., *et al.*, 2005. Tau suppression in a neurodegenerative mouse model improves memory function. *Science* 309, 476-481.

11. Tanzi, R. E., 2005. The synaptic Abeta hypothesis of Alzheimer's disease. *Nat. Neurosci*. 8, 977-979.
12. Tanzi, R. E., Bertram, L., 2005. Twenty years of the Alzheimer's disease amyloid hypothesis: A genetic perspective. *Cell* 120, 545-555.
13. Zlokovic, B. V., 2005. Neurovascular mechanism of Alzheimer's neurodegeneration. *Trends Neurosci*. 28, 202-208.
14. Schenk D., Barbour R., Dunn W., *et al.*, 1999. Immunization with amyloid-beta attenuates Alzheimer-disease-like pathology in the PDAPP mouse. *Nature* 400, 173-177.
15. DeMattos, R. B., Bales, K. R., *et al.*, 2001. Peripheral anti-Aβ antibody alters CNS and plasma Aβ clearance and decreases brain Aβ burden in a mouse model of AD. *PNAS* 98, 8850-8855.
16. Kazatchkine, D., Kaveri, S. V., 2001. Immunomodulation of autoimmune and inflammatory diseases with intravenous immunoglobulin. *N. Engl. J. Med.* 345, 747-755.
17. Choe, L. H., Werner, B. G., Lee, K. H., 2006. Two-dimensional protein electrophoresis: From molecular pathway discovery to biomarker discovery in neurological disorders. *NeuroRx* 3, 327-335.
18. Finehout, E. J., Frank, Z., Lee, K. H., 2004. Towards two-dimensional electrophoresis mapping of the cerebrospinal fluid proteome from a single individual. *Electrophoresis* 25, 2564-2575.
19. D'Ascenzo, M., Relkin, N. R., Lee, K. H., 2005. Alzheimer's disease cerebrospinal fluid biomarker discovery: A proteomics approach. *Current Opinion in Molecular Therapeutics* 7, 557-564.

20. Finehout, E. J., Frank, Z., Relkin, N. R., Lee, K. H., 2006. Proteomic analysis of cerebrospinal fluid changes related to postmortem interval. *Clinical Chemistry* 52, 1906-1913.

21. Finehout, E. J., Frank, Z., Choe, L. H., Relkin, N. R., Lee, K. H., 2007. Cerebrospinal fluid proteomic biomarkers for Alzheimer's disease. *Ann. Neurol.* 61, 120-129.

22. Lundquist, S., Renftel, M., 2002. The use of *in vitro* cell culture models for mechanistic studies and as permeability screens for the blood-brain barrier in the pharmaceutical industry. *Vascular Pharmacology* 38, 355-364.

23. Deli, M. A., Abraham, C. S., Kataoka, Y., Niwa, M., 2005. Permeability studies on *in vitro* blood-brain barrier models: Physiology, pathology, and pharmacology. *Cellular and Molecular Neurobiology* 25, 59-127.

24. Cecchelli, R., Dehouck, B., *et al.*, 1999. *In vitro* model for evaluating drug transport across the blood-brain barrier. *Advanced Drug Delivery Reviews* 36, 165-178.

25. Cecchelli, R., *et al.*, 2007. Modeling of the blood-brain barrier in drug discovery and development. *Nature Reviews Drug Discovery* 6, 650-661.

26. Pardridge, W. M., 2007. Drug targeting to the brain. *Pharm. Res*. 24, 1733-1744.

27. Pardridge, W. M., 2005. The blood-brain barrier: Bottleneck in brain drug development. *NeuroRx* 2, 3-14.

28. Pardridge, W. M., 2003. Blood-brain barrier drug targeting: The future of brain drug development. *Molecular Interventions* 3, 90-105.

29. Calabria, A. R., Weidenfeller, C., Jones, A. R., *et al.*, 2006. Puromycin-purified rat brain microvascular endothelial cell cultures exhibit improved

barrier properties in response to glucocorticoid induction. *J. Neurochem*. 97, 922-933.

30. Cecchelli, R., *et al.*, 1999. *In vitro* model for evaluating drug transport across the blood-brain barrier. *Advanced Drug Delivery* 36, 165-178.
31. Cosine, C., *et al.*, 2005. Mouse syngenic *in vitro* blood-brain barrier model: a new tool to examine inflammatory events in cerebral endothelium. *Laboratory Investigation* 85, 734-746.
32. Dehouck, M. P., Meresse, S., *et al.*, 1990. An easier, reproducible, and mass-production method to study the blood-brain barrier *in vitro*. *J. Neurochem.* 54, 1798-1801.
33. Deli, M. A., Abraham, C. S., Niwa, M., Falus, A., 2003. *N,N*-diethyl-2-[4-(phenylmethyl)phenoxy]ethanamine increases the permeability of primary mouse cerebral endothelial cell monolayers. *Inflamm. Res.* 52, S39-S 40.
34. Demeuse, P., Kerkhofs, A., *et al.*, 2002. Compartmentalized co-culture of rat brain endothelial cells and astrocytes: a syngenic model to study the blood-brain barrier. *J. Neurosci. Meth*. 121, 21-31.
35. Gaillard, P. J., Voorwinden, L. H., *et al.,* 2001. Establishment and functional characterization of an *in vitro* model of the blood-brain barrier, comprising a co-culture of brain capillary endothelial cells and astrocytes. *Euro. J. Pharm. Sci.* 12, 215-222.
36. Gaillard, P.J., *et al.,* 2000. Astrocytes increase the functional expression of p-glycoprotein in an *in vitro* model of the blood-brain barrier. *Pharmaceutical Research* 17, 1198-1205.
37. Nakagawa, S., *et al.,* 2007. Pericytes from brain microvessels strengthen the barrier integrity in primary cultures of rat brain endothelial cells. *Cell Mol. Neurobiol.* 27, 687-694.

38. Nakagawa, S., *et al.,* 2009. A new blood-brain barrier model using primary rat brain endothelial cells, pericytes and astrocytes. *Neurochem. Int*. 54, 253-263.

39. Perriere, N., Demeuse, PH., *et al.,* 2005. Puromycin-based purification of rat brain capillary endothelial cell cultures. Effect on the expression of blood-brain barrier specific properties. *Journal of Neurochemistry* 93, 279-289.

40. Perriere, N., *et al.,* 2007. A functional *in vitro* model of rat blood-brain barrier for molecular analysis of efflux transporters. *Brain Research* 1150, 1-13.

41. Rubin, L. L., Hall, D. E., *et al.,* 1991. A cell culture model of the blood-brain barrier. *J. Cell Biol.*115, 1725-1735.

42. Weidenfeller, C., Schrot, S., *et al.,* 2005. Murine brain capillary endothelial cells exhibit improved barrier properties under the influence of hydrocortisone. *Brain Research* 1053, 162-174.

43. Weidenfeller, C., Svendsen, C. N., Shusta, E., 2007. Differentiating embryonic neural progenitor cells induce blood-brain barrier properties. *Journal of Neurochemistry* 101, 555-565.

44. Jerne, N.K., 1974. Towards a network theory of the immune system. *Ann. Immunol.* 125C, 373-389.

CHAPTER 2

THE BLOOD-BRAIN BARRIER

2.1 The Physiology of the Blood-Brain Barrier

The blood-brain barrier (BBB) is a unique, selective barrier formed by the endothelial cells (EC) that line cerebral capillaries and controls the molecular exchange between the blood and the brain interstitial fluid (ISF). The total length of brain capillaries in humans is estimated to be 650 km, with the total surface area between 10 – 20 m^2. This architecture provides an enormous surface area to maximize transcellular and paracellular transport if cerebral capillaries behaved similar to peripheral capillaries [1].

The EC that line these capillaries differ from those in the peripheral tissue in two ways. First, they have very few endocytotic vesicles, thereby limiting the transcellular flux. Second, they lack fenestrae and are coupled by tight junctions that restrict paracellular flux of water-soluble molecules [1-4]. This observation was first demonstrated by the German microbiologist Ehrlich who recognized the existence of the BBB. He observed that the central nervous system (CNS) was not stained by intravascular water-soluble vital dyes as opposed to peripheral tissue. However, the properties of the BBB are not exclusively due to the special cell biology of the capillary EC. It is evident that perivascular elements, such as closely associated astrocytic end-feet processes, microglia, perivascular neurons and pericytes, further induce the barrier properties of these EC (Figure 2.1) [1-3].

The complexity of the tight junctions in cerebral capillaries is due to the interaction of several transmembrane proteins including occludin, the claudins,

Figure 2.1 | Cellular and molecular components of the BBB. A | Brain capillary EC and pericytes are separated from astrocytes, microglia and neurons by the basement membrane. **B** | Simplified scheme of the molecular composition of the brain tight junctions. Occludin and claudins are the most important membranous components. This figure is adapted by permission from Macmillan Publishers Ltd: [Nature Reviews Neuroscience] (3), © (2006).

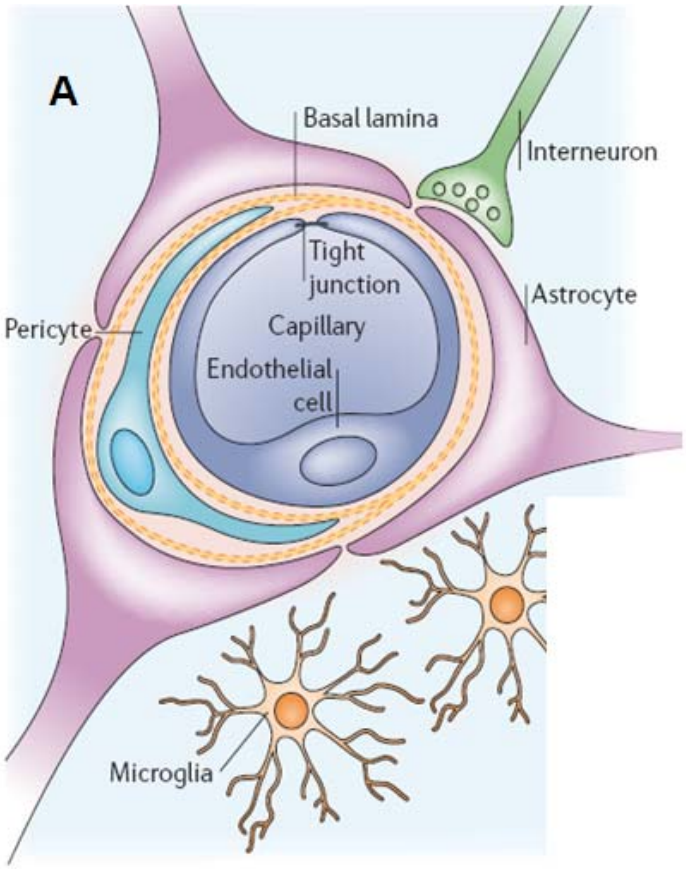
A
Basal lamina
Interneuron
Tight junction
Astrocyte
Pericyte
Capillary
Endothelial cell
Microglia

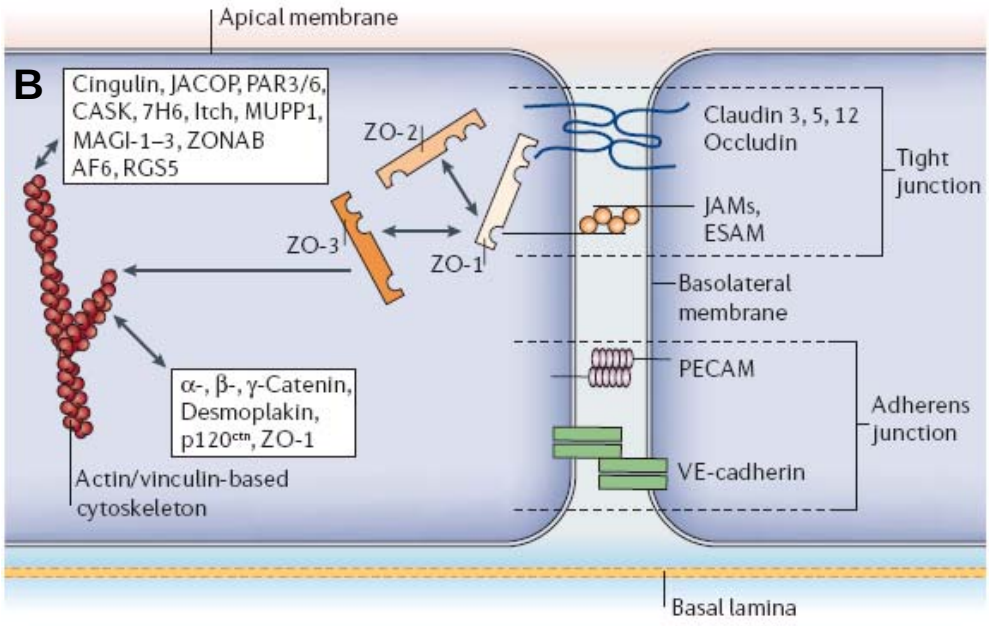
Apical membrane
B
Cingulin, JACOP, PAR3/6, CASK, 7H6, Itch, MUPP1, MAGI-1–3, ZONAB AF6, RGS5
ZO-2
ZO-3
ZO-1
Claudin 3, 5, 12
Occludin
Tight junction
JAMs, ESAM
Basolateral membrane
PECAM
Adherens junction
VE-cadherin
α-, β-, γ-Catenin, Desmoplakin, p120ctn, ZO-1
Actin/vinculin-based cytoskeleton
Basal lamina

and the junctional adhesion molecules (JAMS). A number of cytoplasmic accessory proteins, including zonula occludin protein 1 (ZO-1), ZO-2, and cingulin link the transmembrane proteins to the actin cytoskeleton. This allows paracellular transport to be modulated in response to different stimuli, therefore making the paracellular barrier dynamic (Figure 2.1) [5-6]. The tight junctions significantly restrict even the movement of small ions such as Na^+ and Cl^-, so that the transendothelial electrical resistance (TEER), which is typically 2–20 ($\Omega \times cm^2$) in peripheral capillaries, can be >1,000 ($\Omega \times cm^2$) in brain endothelium. Because the tight junctions make the brain inaccessible to water-soluble (polar) molecules, they are transferred by special transporters [7-9]. Examples of transporters include those for glucose, neutral amino acids, vitamins, and nucleosides (Figure 2.2). In addition, intracellular and extracellular enzymes regulate the metabolic activity at the BBB such as monoamine oxidase (MAO), γ-glutamyl transpeptidase (γ-GTP), alkaline phosphatase, specific peptidases, and nucleotidases [10-11].

It has been clear from the earliest histological studies that brain capillaries are surrounded by, or closely associated with, several cell types, and the influence of this microenvironment is believed to play a major role in inducing the capillary EC [12-13]. Structurally, the cell closest to brain capillary EC are the astrocytes and their foot processes cover much of the capillary's basal surface [14]. In 1987, Janzer *et al.* [15] investigated the notion that astrocytes might induce EC to adapt a brain like phenotype. They cultured rat astrocytes obtained from neonatal brain and transplanted them into a chick eye chamber and further assessed the barrier properties of the EC using cationic dyes that mark albumin flux. The results indicated that rat astrocytes are capable of causing chick peripheral EC to become less permeable to large

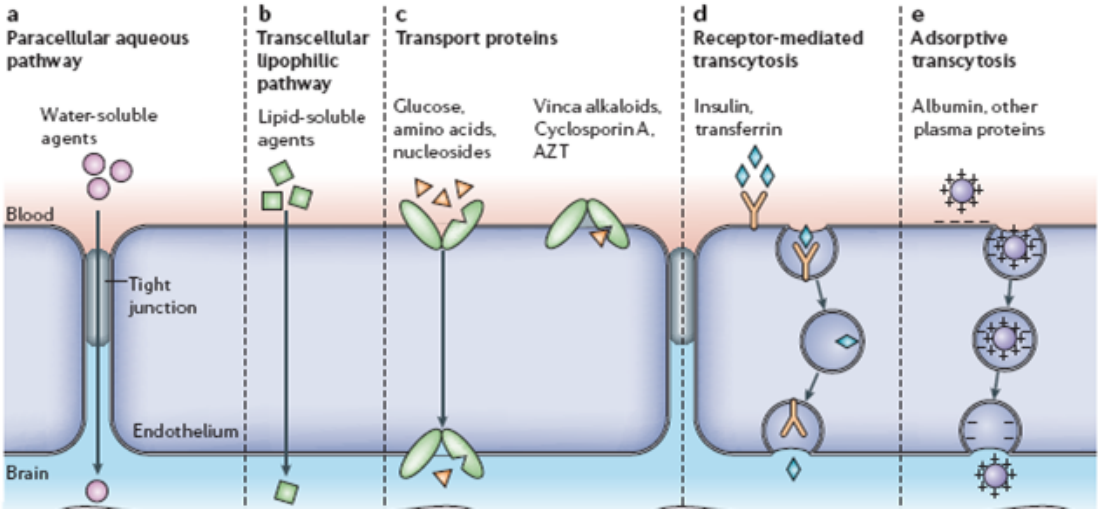

Figure 2.2 | Pathways across the BBB. The tight junctions severely restrict penetration of water-soluble compounds. However, lipid soluble molecules can freely diffuse across the lipid bilayer if they are smaller than 400 Da. The majority of molecules, including nutrients are transported actively. It is believed that larger proteins such as albumin and immunoglobulins are transported by adsorptive transcytosis. This figure is adapted by permission from Macmillan Publishers Ltd: [Nature Reviews Neuroscience] (3), © (2006).

molecules.

2.2 The Role of BBB in Alzheimer's Disease

BBB breakdown due to disruption of tight junctions, altered transport of molecules between blood and brain, aberrant angiogenesis, vessel regression, and inflammatory responses may initiate and/or contribute to a "vicious circle" of the disease process resulting in progressive synaptic and neuronal dysfunction and loss in disorders such as Alzheimer's disease, Parkinson's disease, amyotrophic lateral sclerosis, multiple sclerosis and others [12].

Alzheimer's disease (AD) is characterized by a progressive cognitive decline associated with neurovascular dysfunction, accumulation of neurotoxic amyloid beta (Aβ) on blood vessels and in the brain parenchyma, and intraneuronal lesions, or neurofibrillar tangles [16-24]. According to Figure 2.3, changes in the expression of key vascular genes and receptors in brain capillaries and small cerebral arteries may compromise (directly or indirectly) several BBB functions. This compromise, in turn, leads to reductions in the resting cerebral blood flow (CBF) and attenuated CBF responses to brain activation, accumulation of Aβ, and a neuroinflammatory response resulting in BBB breakdown. In an early disease phase, faulty clearance of Aβ at the BBB may favor accumulation of neurotoxic Aβ oligomers in the brain ISF. Aβ oligomers and focal reductions in the capillary blood flow can affect synaptic transmission, cause neuronal injury, and initiate recruitment of microglia from the blood or within the brain. At an early symptomatic stage, the BBB starts losing properties of an Aβ clearing membrane, and the activated endothelium secretes proinflammatory cytokines and CBF suppressors. This secretion

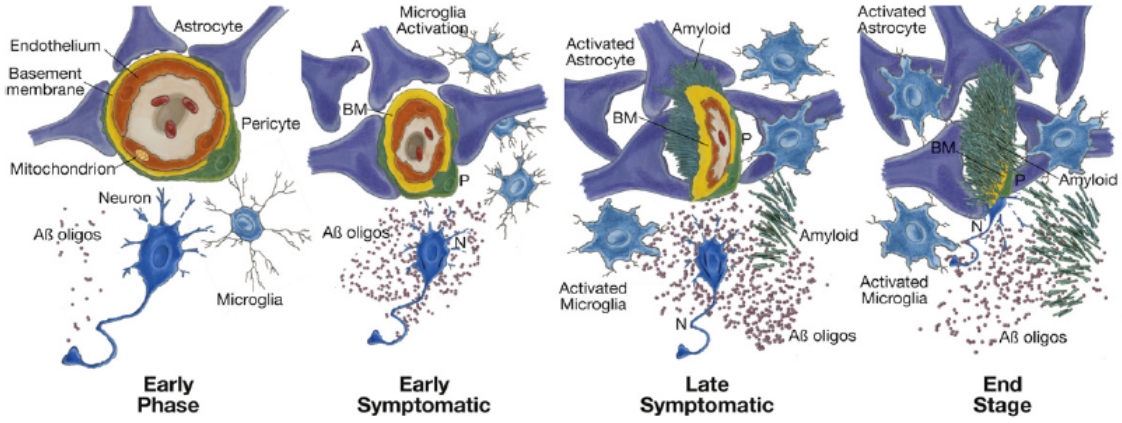

Figure 2.3 | Involvement of the neurovascular unit in the pathogenesis of AD. This figure is reprinted from [12] © (2008), with permission from Elsevier.

results in a more pronounced synaptic dysfunction, accumulation of intraneuronal tangles, and activation of microglia leading to the activation of immunoglobulins. At a late symptomatic stage, the capillary unit is distorted with the degenerated endothelial barrier. There is a severe loss of Aβ clearing capability, resulting in amyloid formation on the outer side of the capillary membrane, an increased number of neurofibrillary tangles, and an increased number of activated microglia and astrocytes. At the final stage, the capillary unit disappears under the amyloid deposits coupled with synaptic and neuronal loss.

2.3 Static In vitro Models of the BBB

Designing *in vitro* BBB models are important for two reasons. First, the BBB plays an important physiological role in a number of pathologies (i.e. stroke, traumatic injury, brain tumors, multiple sclerosis, AIDS dementia, Parkinson's disease, and AD) and the models provide an opportunity to identify the key factors that contribute to normal and pathological BBB [12,25]. Second, models help to predict drug permeability prior to animal studies due to inherent difficulties in performing molecular level studies on the BBB *in vivo* [1].

Several static *in vitro* models of the BBB have been developed with the aim to better understand the cell biology of the BBB and/or to predict potential therapeutic permeability into the brain [26-40]. Most of these models consist of a monolayer of endothelial cells, often isolated from brain capillaries (BMEC) or peripheral capillaries, grown on the top side of a polymeric membrane affixed to a cylindrical plastic insert (i.e. culture Transwell®). These microporous membranes are either made of polyester (partially transparent) or polycarbonate (translucent). They are 20 – 40 μm thick depending on the

manufacturer, and their pore diameter is either 0.4 μm, 1.0 μm, or 3.0 μm with their nominal pore density being 4×10^6 (polyester) and 1×10^8 (polycarbonate) pores/cm^2.

This insert is placed into a multi-well culture plate, dividing the well into luminal and abluminal chambers. Furthermore, to recreate the brain microenvironment, astrocytes or pericytes are cultured in the abluminal chamber to create co-cultures, or the brain EC are cultured in astrocyte conditioned medium [27-29,31-39]. The co-cultures are either contact co-cultures, where astrocytes or pericytes are directly seeded on the opposite side of the microporous membrane, or non-contact co-cultures where the glial cells are seeded on the multi-well culture plate (Figure 2.4). Finally, the barrier properties of the model are usually assessed by one or more of the following techniques: transendothelial electrical resistance (TEER) measurements, direct determination of molecular permeability coefficients, immunocytochemical characterization of tight junction proteins, and assessing the expression level of mRNA and proteins that are highly expressed at the BBB (P-glycoprotein, glucose transporter-1, γ-GTP).

2.4 Physical and Biological Limitations of Current Static BBB Models

As mentioned in Sections 2.1 and 2.3, because astrocyte foot processes surround the brain capillaries, many *in vitro* models have focused on recreating the brain microenvironment by incorporating astrocyte conditioned-medium or astrocyte contact or non-contact co-cultures. The purpose of creating the contact co-culture is to mimic the BBB anatomy by providing the astrocyte foot processes the opportunity to reach through the pores of the membrane and physically contact endothelial cells on the opposite side.

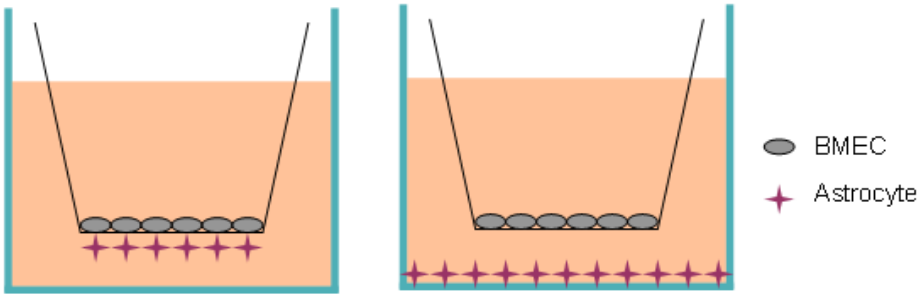

Figure 2.4 | Transwell® culture systems. Contact co-culture (left) and non-contact co-culture (right). The top compartment represents the luminal (blood) side and the bottom represents the abluminal (brain) side. BMEC stands for brain microvascular endothelial cells.

A key drawback of the commercial microporous membrane is the limited number of pore sizes, the low total porosity, and the relatively thick membrane. Furthermore, the process of fabrication of these membranes results in a random distribution in the size and placement of pores, and more importantly the resulting diffusion path is tortuous causing entrapment of biomolecules [41-42]. These characteristics and the relatively large thickness of the membrane may hinder cell to cell contact in co-cultures or the passage of soluble factors through the pores [42-43].

Furthermore, the majority of current *in vitro* models of the BBB are either based on immortalized brain EC or primary BMEC obtained from rat, bovine, or porcine. Use of such models may not be suitable for studies of BBB in brain cancer, neurodegenerative disorders, and inflammatory events involving the CNS because these diseases are generally studied in mouse models and thus an *in vitro* BBB model based on mouse BMEC may be more authentic and serve as a better surrogate to correlate with the *in vivo* studies [12,25].

REFERENCES

1. Cecchelli, R., Berezowski, V., Lundquist, S. *et al.*, 2007. Modeling of the blood-brain barrier in drug discovery and development. *Nature Rev. Drug Discovery* 6, 650-661.
2. Abbott, N. J., 2002. Astrocyte-endothelial interactions and blood-brain barrier permeability. *J. Anat*. 200, 629-638.
3. Abbott, N. J., Ronnback, L., Hansson, E., 2006. Astrocyte-endothelial interactions at the blood-brain barrier. Nature Rev. *Neuroscience* 7, 41-53.
4. Rubin, L. L., Staddon, J. M., 1999. The cell biology of the blood brain barrier. *Annu. Rev. Neurosci*. 22, 11-28.
5. Ballabh, P., Braun, A., Nedergaard, M., 2004. The blood brain barrier: an overview: structure, regulation, and clinical implications. *Neurobiol. Dis*. 16, 1-13.
6. Huber, J.D., Egleton, R.D., Davis, T.P., 2001. Molecular physiology and patho-physiology of tight junctions in the blood-brain barrier. *Trends Neurosci.* 12, 719-725.
7. Bradbury, M., 1979. The concept of a blood-brain barrier. Wiley, New York.
8. Pardridge, W.M., 1991. Peptide drug delivery to the brain. Raven Press, New York.
9. Pardridge, W.M., *et al.*, 1990. Comparison of *in vitro* and *in vivo* models of drug transcytosis through the blood-brain barrier. *J. Pharmacol Exp. Ther*. 253, 884-891.
10. Ghersi-Egea, J. F., Leninger-Muller, B., Suleman, G., Siest, G., Minn, A., 1994. Localization of drug metabolizing enzyme activities to blood-brain interfaces and circumventricular organs. *J. Neurochem*. 62, 1089-1096.

11. El-Bacha, R.S., Minn, A., 1999. Drug metabolizing enzymes in cerebrovascular endothelial cells afford a metabolic protection to the brain. *Cell. Mol. Biol*. 45, 15-23.
12. Zlokovic, B.V., 2008. The blood-brain barrier in health and chronic neurodegenerative disorders. *Neuron* 57, 178-201.
13. Davson, H., Oldendorf, W. H., 1967. Transport in the central nervous system. *Proc. R. Soc. Med*. 60, 326-328.
14. Kacem, K., Lacombe, P., *et al.*, 1998. Structural organization of the perivascular astrocyte endfeet and their relationship with the endothelial glucose transporter. *Glia* 23, 1-10.
15. Janzer, R. C., Raff, M. C., 1987. Astrocytes induce blood-brain barrier properties in endothelial cells. *Nature* 325, 253-257.
16. Deane, R., Zlokovic, B.V., 2007. Role of blood-brain barrier in the pathogenesis of Alzheimer's disease. Curr. *Alzheimer Res*. 4, 191-197.
17. Hardy, J., 2006. A hundred years of Alzheimer's disease research. *Neuron* 52, 3-13.
18. Iadecola, C., 2004. Neurovascular regulation in the normal brain and in Alzheimer's disease. *Nat. Rev. Neurosci*. 5, 347-360.
19. Lee, V.M., Balin, B.J., *et al.*, 1991. A major subunit of paired helical filaments and derivatized forms of normal Tau. *Science* 251, 675-678.
20. Rovelet-Lecrux, A., *et al.*, 2006. App locus duplication causes autosomal dominant early-onset Alzheimer's disease with cerebral amyloid angiopathy. *Nat. Genet*. 38, 24-26.
21. Santacruz, K., Lewis, J., *et al.,* 2005. Tau suppression in a neurodegenerative mouse model improves memory function. *Science* 309, 476-481.

22. Tanzi, R.E., 2005. The synaptic Amyloid beta hypothesis of Alzheimer's disease. *Nat. Neurosci*. 8, 977-979.

23. Tanzi, R.E., Bertram, L., 2005. Twenty years of the Alzheimer's disease amyloid hypothesis: A genetic perspective. *Cell* 120, 545-555.

24. Zlokovic, B.V., 2005. Neurovascular mechanism of Alzheimer's neurodegeneration. *Trends Neurosci*. 28, 202-208.

25. Nag, S., ed., 2003. The blood-brain barrier: biology and research protocols. Humana Press, New Jersey.

26. Calabria, A. R., Weidenfeller, C., Jones, A. R., *et al.,* 2006. Puromycin-purified rat brain microvascular endothelial cell cultures exhibit improved barrier properties in response to glucocorticoid induction. *J. Neurochem*. 97, 922-933.

27. Cecchelli, R., *et al.,* 1999. *In vitro* model for evaluating drug transport across the blood-brain barrier. *Advanced Drug Delivery* 36, 165-178.

28. Cosine, C., *et al.,* 2005. Mouse syngenic *in vitro* blood-brain barrier model: a new tool to examine inflammatory events in cerebral endothelium. *Laboratory Investigation* 85, 734-746.

29. Dehouck, M. P., Meresse, S., *et al.,* 1990. An easier, reproducible, and mass-production method to study the blood-brain barrier *in vitro*. *J. Neurochem.* 54, 1798-1801.

30. Deli, M. A., Abraham, C. S., Niwa, M., Falus, A., 2003. *N,N*-diethyl-2-[4-(phenylmethyl)phenoxy]ethanamine increases the permeability of primary mouse cerebral endothelial cell monolayers. *Inflamm. Res.* 52, S39-S 40.

31. Demeuse, P., Kerkhofs, A., *et al.,* 2002. Compartmentalized co-culture of rat brain endothelial cells and astrocytes: a syngenic model to study the blood-brain barrier. *J. Neurosci. Meth*. 121, 21-31.

32. Gaillard, P. J., Voorwinden, L. H., *et al.,* 2001. Establishment and functional characterization of an *in vitro* model of the blood-brain barrier, comprising a co-culture of brain capillary endothelial cells and astrocytes. *Euro. J. Pharm. Sci*. 12, 215-222.

33. Gaillard, P.J., *et al.,* 2000. Astrocytes increase the functional expression of p-glycoprotein in an *in vitro* model of the blood-brain barrier. *Pharmaceutical Research* 17, 1198-1205.

34. Nakagawa, S., *et al.,* 2007. Pericytes from brain microvessels strengthen the barrier integrity in primary cultures of rat brain endothelial cells. *Cell Mol. Neurobiol.* 27, 687-694.

35. Nakagawa, S., *et al.,* 2009. A new blood-brain barrier model using primary rat brain endothelial cells, pericytes and astrocytes. *Neurochem. Int.* 54, 253-263.

36. Perriere, N., Demeuse, PH., *et al.,* 2005. Puromycin-based purification of rat brain capillary endothelial cell cultures. Effect on the expression of blood-brain barrier specific properties. *Journal of Neurochemistry* 93, 279-289.

37. Perriere, N., *et al.,* 2007. A functional *in vitro* model of rat blood-brain barrier for molecular analysis of efflux transporters. *Brain Research* 1150, 1-13.

38. Rubin, L. L., Hall, D. E., *et al.,* 1991. A cell culture model of the blood-brain barrier. *J. Cell Biol.*115, 1725-1735.

39. Weidenfeller, C., Schrot, S., *et al.,* 2005. Murine brain capillary endothelial cells exhibit improved barrier properties under the influence of hydrocortisone. *Brain Research* 1053, 162-174.

40. Weidenfeller, C., Svendsen, C. N., Shusta, E., 2007. Differentiating embryonic neural progenitor cells induce blood-brain barrier properties. *Journal of Neurochemistry* 101, 555-565.

41. Harris, S., Shuler, M. L., 2003. Growth of endothelial cells on microfabricated silicon nitride membranes for an *in vitro* model of the blood-brain barrier. *Biotechnology and Bioprocess Engineering* 8, 246-251.

42. Harris, S., Lepak, L. A, *et al.*, 2005. An endothelial and astrocyte co-culture model of the blood-brain barrier utilizing an ultra-thin, nanofabricated silicon nitride membrane. *Lab on a chip* 5, 74-85.

43. Demeuse, P., Kerkhofs, A., *et al.*, 2002. Compartmentalized co-culture of rat brain endothelial cells and astrocytes: a syngenic model to study the blood-brain barrier. *J. Neurosci. Meth*. 121, 21-31.

CHAPTER 3

THE EFFECT OF ASTROCYTES ON THE INDUCTION OF BARRIER PROPERTIES IN AORTIC ENDOTHELIAL CELLS

3.1 Preface

This chapter is adapted from: Shayan, G., Shuler, M. L., Lee, K. H., 2009. The effect of astrocytes on the induction of barrier properties in aortic endothelial cells. *Biotechnology Progress*, submitted. It explores the possibility of using bovine aortic endothelial cells in co-culture with astrocytes to create an *in vitro* model of the blood-brain barrier.

3.2 Abstract

The establishment of a primary culture of brain microvascular endothelial cells (BMEC) for the construction of *in vitro* models of the blood-brain barrier (BBB) is difficult and time intensive in part due to a lack of culture purity, low yields, and cellular de-differentiation after the first passage. This problem has created interest in the substitution of BMEC with immortalized brain endothelial cells (EC), or peripheral EC such as bovine aortic EC (BAEC). These cultures are easier to establish, provide higher yields, and can be passaged. Many BBB models have focused on further inducing the brain and peripheral EC by incorporating astrocyte contact or non-contact co-cultures. However, previous studies demonstrating induction effects of astrocyte on BAEC in contact co-cultures, failed to recognize the extensive barrier properties of astrocytes alone, which can have a significant effect on interpreting the results. This manuscript reports the establishment of a contact and non-contact co-culture

between astrocytes and BAEC or BMEC (as a control) with primary focus on the properties of astrocytes alone and with an enhanced statistical methodology to interpret the results. Transendothelial electrical resistance (TEER) and permeability studies revealed that astrocytes can significantly increase the barrier tightening of BMEC, while having no effect on BAEC. Immunocytochemical studies also revealed the reorganization of BMEC occludin junctions in the presence of astrocytes, while indicating the absence of this junction protein in BAEC. In contrast to a previous report, here the statistical analysis revealed that observed decreases in permeability of BAEC in contact co-cultures is due to the addition of astrocytes' properties in series and not due to induction.

3.3 Introduction

Endothelium, comprising the single cell lining of all blood and lymph vessels, plays a variety of crucial roles in the cardiovascular system. The endothelium of different tissues however have further specialized functions. For instance, in the brain the endothelial cells (EC) that line the cerebral vasculature provide an important barrier (the blood-brain barrier, BBB) for protecting the brain from fluctuations in plasma composition [1]. Early studies have shown that the brain microenvironment plays a critical role in the differentiation of capillary EC. The close cell-cell associations between capillary EC and astrocytes in particular led to the suggestion that they could mediate specific features of the BBB phenotype [2].

Several *in vitro* models of the BBB have been developed to better understand the underlying cell biology, to predict drug permeability prior to animal studies, and to overcome the inherent difficulty in performing BBB

molecular level studies *in vivo* [3]. These *in vitro* models [4-12] serve as successful surrogates to *in vivo* experiments and provide a critical framework for BBB studies. Over time, these models have been updated and refined to improve their utility. These updates include improved techniques to isolate brain microvascular endothelial cells (BMEC) [6,10,12], and induction of BMEC with astrocytes or biochemical agents [4,7-11]. Despite these advances, a comparison of experimental results within the many published *in vitro* models remains a challenge because of differences with respect to cellular isolation procedures, culture configurations (mono/co-culture), the cell type used (origin and species), and model assessment techniques [13].

Many *in vitro* models are based on the isolation and culture of brain EC. However, the establishment of a primary culture of BMEC devoid of other brain contaminating cells (i.e. neurons, pericytes, and microglia) is difficult and time intensive, and depending on the source of brain (murine, rat, porcine, etc.) yields can be very low [13]. Furthermore, once BMEC are cultured *in vitro*, cellular de-differentiation results in a loss of many of the functions and markers observed *in vivo* thus limiting the use of cells to passages 0 -1 [4,14]. Although recently a few studies have successfully proposed new biochemical techniques to establish pure and functional cultures of BMEC [4,10,15], there still exists considerable interest in the substitution of BMEC with either immortalized brain EC, or peripheral EC such as human umbilical vein EC or bovine aortic EC (BAEC), because it is easier to obtain high yields, culture, and passage these cells [5,16-18].

Structurally, the cell type closest to brain capillary EC is the astrocyte and their processes form end-feet that collectively surround cerebral microvessels [5,7,9,18-20]. As a result, several models have focused on

recreating the brain microenvironment by incorporating astrocyte co-cultures, or astrocyte conditioned-medium to further induce BMEC, immortalized brain and peripheral EC. Traditionally, many models involve a contact, or often a non-contact, co-culture between EC and astrocytes on commercially available microporous filters. Furthermore, rat or bovine BMEC co-cultured with rat astrocytes were shown to have higher transendothelial electrical resistance (TEER) and lower permeability compared to BMEC cultures alone [5,7-10,12]. However, in the case of BAEC, conclusive studies on the properties of astrocytes alone and in co-culture is limited. Therefore, it is difficult to assess whether the improved barrier properties in contact co-cultures is due to induction of EC, or is due to the summation of the properties of these two cell lines individually.

The work presented here primarily emphasizes the properties of rat primary astrocytes alone and uses contact and non-contact co-cultures between BAEC and rat primary astrocytes to more accurately examine possible induction effects of astrocytes on this non-neuronal EC. With this new emphasis, we evaluated more accurately whether there is synergy in co-culture TEER and permeability. The results indicated that astrocytes' ability to grow in multiple layers can significantly affect TEER and permeability measurements in contact co-cultures. The linear contrast statistical analysis revealed that decrease in permeability across BAEC contact co-culture is due to the addition of astrocytes' resistance in series. The results also indicated that while BMEC recognizes the induction factors released by astrocytes in non-contact co-cultures, BAEC fails to do so.

3.4 Materials and Methods

3.4.1 Chemicals and Supplies

Poly-D-lysine and L-glutamine were purchased from Fisher Scientific (Pittsburg, PA, USA). Human fibronectin was purchased from Millipore (Billerica, MA, USA). Twelve and twenty four well Transwell® permeable support (polyester; thickness, 10 μm; pore size, 0.4 μm; pore density, $4x10^6$ pores/cm^2) was purchased from Corning (Lowell, MA, USA). EGM® MV and trypsin-EDTA were purchased from Lonza (Basel, Switzerland). Fetal bovine serum (FBS), Dulbecco's Modified Eagle Medium (DMEM, with l-glutamin, sodium pyruvate, and low glucose), Ham's F-12 nutrient mixture, and Penicillin-Streptomycin-Amphotercin (PSA) were purchased from Invitrogen (Carlsbad, CA, USA). Dulbecco's phosphate buffered saline (DPBS, without $CaCl_2$ and $MgCl_2$), gentamicin, HEPES sodium salt, fluorescein sodium salt, Heparin, bovine serum albumin, puromycin, hydrocortisone, collagen type IV, Triton X-100, and goat serum were purchased from Sigma (St. Louis, MO, USA). Percoll was purchased from Amersham Biosciences (Piscataway, NJ, USA). Type II collagenase and DNase I were purchased from Worthington Biochemical Corp. (Lakewood, NJ, USA). Collagenase-dispase and basic fibroblast growth factor were purchased from Roche Molecular Biochemicals (Indianapolis, IN, USA). Paraformaldehyde (16%) was purchased from Electron Microscopy Sciences (Ft. Washington, PA, USA). Acetylated low density lipoprotein labeled with 1,1'-dioctadecyl-3,3,3',3'-tetramethylindo-carbocyanine percholorate (DiI-Ac-LDL) and bovine platelet-poor plasma-derived serum were purchased from Biomedical Technologies (Stoughton, MA, USA). Polyclonal rabbit anti-glial fibrillary acidic protein (18-0063) antibody, rabbit anti-occludin (71-1500) antibody, Alexa Fluor® 488 goat anti-

rabbit IgG antibody (A11008), and 4',6-diamidino-2-phenylindole (DAPI) dihydrochloride nuclear stain were also purchased from Invitrogen (Carlsbad, CA, USA). Vectashield mounting medium was purchased from Vector Laboratories (Burlingame, CA, USA). EVOM voltohmmeter (STX2) was purchased from World Precision Instruments (Sarasota, FL, USA).

3.4.2 Isolation of Rat Astrocytes

Astrocytes isolated from 3 days old Wistar rat pups were provided by Dr. W. Shain (Wadsworth Center, Albany, NY) following established techniques [21]. Cells were maintained in DMEM (low glucose, with L-glutamine and sodium pyruvate) supplemented with 5% FBS and gentamicin at the supplier's recommended concentration. Cells were grown on 75 cm^2 tissue culture flasks at passage 0 and were fed every 3 days by completely replacing the medium. Cultures were maintained in a 37°C humidified cell culture incubator with 5% CO_2.

3.4.3 Bovine Aortic Endothelial Cells (BAEC)

Cryopreserved, single donor, bovine aortic endothelial cells were purchased from Lonza (Basel, Switzerland) at passage 1. Cells were thawed, maintained, and sub-cultured according to the supplier's recommendations. Briefly, cells were maintained in endothelial basal medium supplemented with bovine brain extract, heparin, human epidermal growth factor, hydrocortisone, gentamicin-amphotericin, and 10% fetal bovine serum (EGM® MV). Cells were grown on 25 cm^2 tissue culture flasks and used at passage 1-6 for experiments. Cultures were maintained in a 37°C humidified cell culture incubator with 5% CO_2.

3.4.4 Isolation of Murine Brain Microvascular Endothelial Cells (BMEC)

Isolation of murine BMEC was based on a modified protocol [4,11]. All animals were treated according to protocols evaluated and approved by the ethical committee of Cornell University. In summary, 10 adult female mice (B6CByF1) were euthanized under CO_2. Forebrains were collected and stored in DMEM on ice. The remainder of the isolation took place under aseptic conditions. The brains were cut sagittally into two haves and rolled on Whatman 3MM chromatography paper to remove the meninges. The cortices were dissected away and much of the white matter was removed. The cortices were smashed with forceps and completely triturated and digested with 0.65 mg/mL type II collagenase and 37.6 U/mL DNase I in DMEM for 1 hour in 37°C shaker (250 rpm). The enzyme solution was then diluted in DMEM and centrifuged at 1000 *g* for 8 minutes. To remove myelin the pellet was re-suspended in 20% (w/v) bovine serum albumin in DMEM and centrifuged at 1000 *g* for 20 minutes. The pellet was re-suspended and further digested with 0.69 mg/mL collagenase-dispase and 28.3 U/mL DNase I in DMEM for 1 hour in 37°C shaker (200 rpm). The microvessels were separated on a 33% continuous Percoll gradient, collected and plated in a 35mm petri-dish coated with collagen type IV and fibronectin. Cultures were maintained in DMEM supplemented with 4 µg/mL puromycin, 20% bovine platelet-poor plasma-derived serum, 1 ng/mL human basic fibroblast growth factor, 1 µg/mL heparin, 2 mM L-glutamine, and an antibiotic solution (100 U/mL penicillin, 100 µg/mL streptomycin, and 0.25 µg/mL amphotericin). Culture medium was completely replaced every day, and puromycin was removed from the medium on day 3. Cells were subcultured on day 3.5 and seeded on transwells coated with collagen type IV and fibronectin at 300,000 cells/cm^2. Cultures were maintained in Ham's F-

12:DMEM (1:1) supplemented with 2 mM L-glutamine, 550 nM hydrocortisone, and an antibiotic solution (100 U/mL penicillin, 100 µg/mL streptomycin, and 0.25 µg/mL amphotericin). Cultures were maintained in a 37°C humidified cell culture incubator with 5% CO_2.

3.4.5 Co-Culture Setup

For the BAEC study, two different models were created each including two types of co-cultures (contact and non-contact) (Figure 3.1). In model 1, BAEC were seeded 8 hours post astrocyte seeding; whereas in model 2, BAEC were seeded 3 days post astrocyte seeding. Model 2 was also replicated using murine BMEC as a control.

For better astrocyte attachment, the backside of the transwell or the bottom of the multi-well dish was treated with 5 µg/cm^2 of poly-D-lysine in DMEM without serum for one hour in the culture incubator. Before use, poly-D-lysine was aspirated and the surface was rinsed once with DPBS. Astrocytes (passage 1) were seeded at 10,000 cells/cm^2 either on the bottom of the dish (non-contact co-culture) or on the backside of the transwell (contact co-culture). For contact co-cultures, an in-house multi-well dish with deeper wells (Figure 3.2) was designed and fabricated. With this device, the transwell can be inverted inside the well without the membrane coming in contact with the lid, thus allowing for a longer time for astrocytes to attach with medium around the transwell. After 8 hours, all transwells were inverted inside a regular 12-well or 24-well culture dish containing DMEM supplemented with 5% FBS in the bottom compartment. If the top compartment was to be seeded with BAEC immediately (model 1), it was seeded at 84,000 cells/cm^2 (passage 5) in EGM® MV. In model 2, the top compartment was filled with EGM® MV or

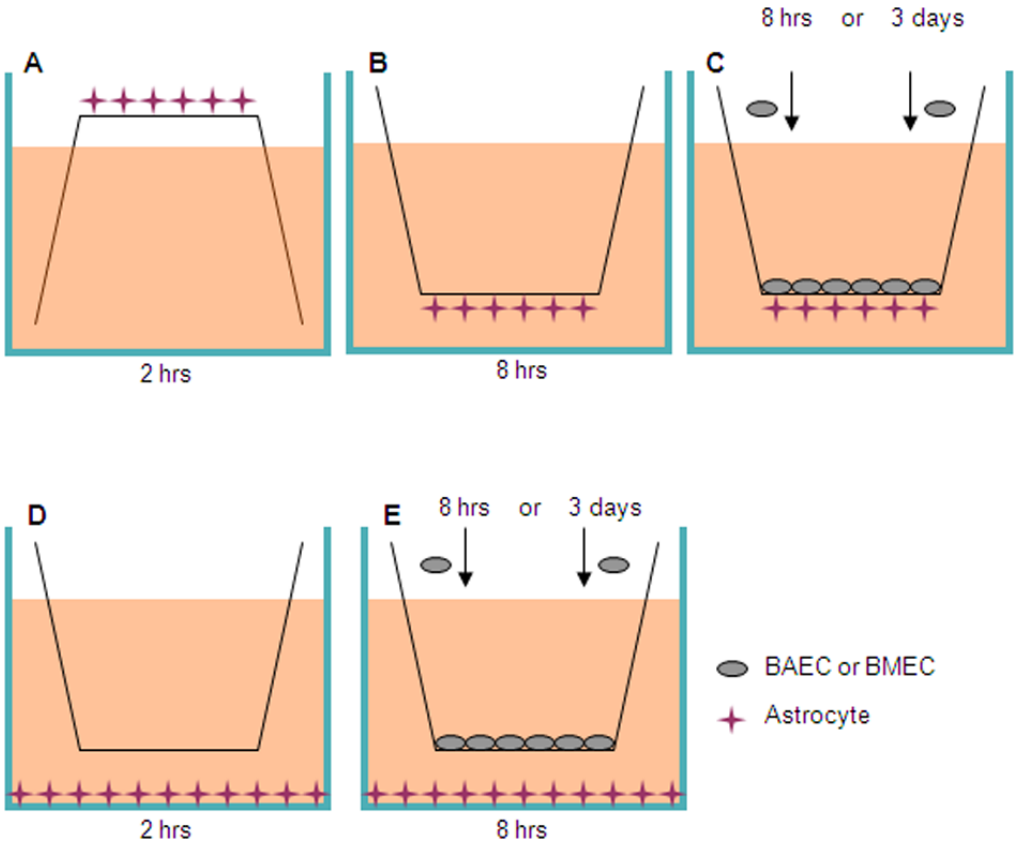

Figure 3.1 | Schematic of two different BBB models. (A-C) shows the contact co-culture. Astrocytes were seeded on the backside of the membrane for 2 hrs while the transwell was inverted inside the multi-well dish. The transwell was then placed inside a regular multi-well dish for 8 hrs after which BAEC was added (model 1). In Model 2, BAEC or BMEC was added 3 days after the attachment of astrocytes. **(D-E)** shows that non-contact co-culture with the same culture conditions as the contact co-culture.

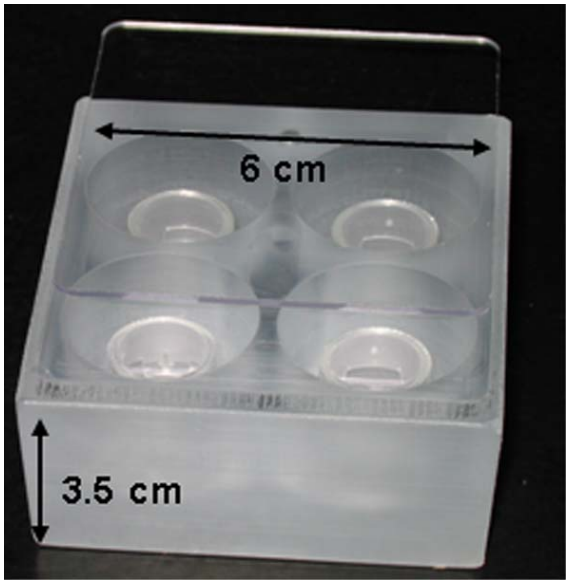

Figure 3.2 | Design of the in-house multi-well dish. The multi-well dish provides significant head space above the transwell which facilitates astrocyte attachment and culture.

BMEC medium (Ham's F-12:DMEM (1:1) supplemented with 2 mM L-glutamine, 550 nM hydrocortisone, and an antibiotic solution) until day 3 when BAEC (passage 6) or murine BMEC were seeded as described above. Controls included empty transwell with the top-side of the membrane coated with collagen type IV and fibronectin and bottom-side coated with poly-D-lysine, BAEC only (in EGM® MV), murine BMEC only (in BMEC medium), and astrocyte only transwells. Culture medium in both compartments was replaced completely every 3 days.

3.4.6 Transendothelial Electrical Resistance Measurements

Transendothelial electrical resistance (TEER) was measured using an EVOM voltohmmeter (STX2) on days 2 and 3 following establishment of co-culture. Final resistance ($\Omega \times cm^2$) was calculated after subtracting the resistance of an empty filter. In the case of contact co-cultures, the resistance of astrocytes were also subtracted from the total resistance by the means of linear contrast analysis [22]. Three TEER measurements were made for each transwell at each time point and the arithmetic mean calculated. TEER measurements of three transwells for each culture condition were used to compute the mean and standard deviations reported.

3.4.7 Fluorescein Sodium Permeability Measurements

Prior to permeability studies, culture media from the top and bottom compartments was replaced with pre-equilibrated transport buffer (10 mM HEPES, 0.1% w/v bovine serum albumin, 4.5% w/v glucose). A solution of sodium fluorescein (376 Da) in transport buffer was then added to the upper compartment of the transwell to yield a final concentration of 1 μM. Two

hundred microliter aliquots were removed from the bottom compartment and the volume replaced with pre-equilibrated transport buffer every fifteen minutes over 60 minutes. Based on the rate of influx of sodium fluorescein into the bottom compartment, permeability coefficients were calculated [6].

3.4.8 Uptake of DiI-Ac-LDL

DiI-Ac-LDL was diluted to 10 µg/mL in EGM® MV or BMEC medium and added to the upper compartment containing BAEC or BMEC prior to other immunofluorescent studies. The cells were then incubated in a 37°C humidified cell culture incubator with 5% CO_2 for 4 hours. The cells were rinsed three times with DPBS and then fixed in 4% (w/v) paraformaldehyde at room temperature for 20 minutes.

3.4.9 Immunocytochemistry

All cultures were rinsed twice with DPBS followed by fixation in 4% paraformaldehyde for 20 minutes (all steps performed at room temperature unless stated otherwise). Following three 5 minute rinses in DPBS, astrocytes were permeabilized with 0.1% Triton X-100 in DPBS for 15 minutes, and BAEC or BMEC were permeabilized with 0.05% Triton X-100 for 5 minutes on ice. (BAEC and BMEC were also pre-permeabilized with 0.2% Triton X-100 for 2 minutes on ice if staining for occludin). After three 5 minute rinses in DPBS following permeabilization, astrocytes and EC were blocked in 10% goat serum in DPBS for 15 and 7 minutes, respectively. All subsequent steps were performed on a shaker. The following concentrations in 10% goat serum were used for primary antibodies: rabbit anti-GFAP 4 µg/mL, and rabbit anti-occludin 15 µg/mL. Primary antibodies were added to the appropriate

compartment for 1 hour followed by three 10 minutes rinses in 1% goat serum. Cells were incubated for 1 hour in 1:500 dilution of Alexa Fluor® 488 goat anti-rabbit IgG antibody followed by three 10 minutes rinses in 1% goat serum. DAPI was added in 300 nM for 3 minutes prior to mounting the membrane on a glass slide with a cover slip in Vectashield mounting medium. Samples were observed in a Leica SP2 scanning confocal misroscope (Leica Microsystems Inc., Bannockburn, IL, USA).

Control samples were treated exactly as stated above, except that the primary antibodies were replaced with a rabbit IgG fraction negative control. A secondary antibody-only control was also included.

3.4.10 Statistical Analysis

The statistical analysis was carried out using JMP® 7.0 (SAS Institute Inc., Cary, NC, USA). Statistical evaluation of the resistance and permeability data was performed using a least square linear regression model. All results are mean ± standard deviation (SD).

One-way analysis of variance (ANOVA) was used to evaluate the effect of cultivation period on the resistance of astrocytes and BAEC alone. The influence of astrocytes on the resistance and permeability of BAEC and BMEC in contact and non-contact co-cultures was also evaluated using one-way ANOVA with linear contrast. If the effect of any factor was significant, pair-wise comparisons were made using the Tukey honestly significant difference (HSD) test. The global risk was fixed at $p < 0.05$ for all tests.

3.5 Results

3.5.1 Effect of Cultivation Period on TEER of Astrocytes and BAEC

Before establishing the co-cultures, two separate experiments were performed to evaluate the changes in the resistance of astrocytes seeded on the backside of polyester transwells over time, as well as BAEC resistance seeded in the top compartment of the transwell. TEER was monitored starting on day 2 until a significant reduction was observed (Figure 3.3). TEER of BAEC significantly increased on day 3 followed by a significant reduction on day 4. TEER of astrocytes significantly increased on day 7 followed by a significant reduction on day 9.

3.5.2 Effect of Astrocytes on TEER of BAEC and Murine BMEC

Two different models, each including two types of co-cultures (contact and non-contact) (Figure 3.1, Figure 3.2) were created based on the TEER results from the previous experiment. The purpose of creating two models was to evaluate whether the age of astrocytes, and thus the concentration of astrocytes' soluble factors as well as their peak TEER, in both contact and non-contact co-culture has a significant effect on induction of BAEC.

TEER results from model 1 (Figure 3.4 A) illustrate that on day 3 when BAEC reach their peak TEER (20.3 ± 7.7 $\Omega \times cm^2$), the resistance of the contact and non-contact co-cultures are significantly less than the resistance of BAEC alone (1.8 ± 7.7 ; 4.2 ± 7.7 $\Omega \times cm^2$), suggesting that astrocytes reduce the resistance of BAEC if both cells are seeded within a few hours of each other. On the other hand in model 2, when BAEC are seeded 3 days after astrocytes (i.e. both cell types reaching their peak TEER concurrently), the resistance of the non-contact co-culture (25.7 ± 3.2 $\Omega \times cm^2$) is statistically

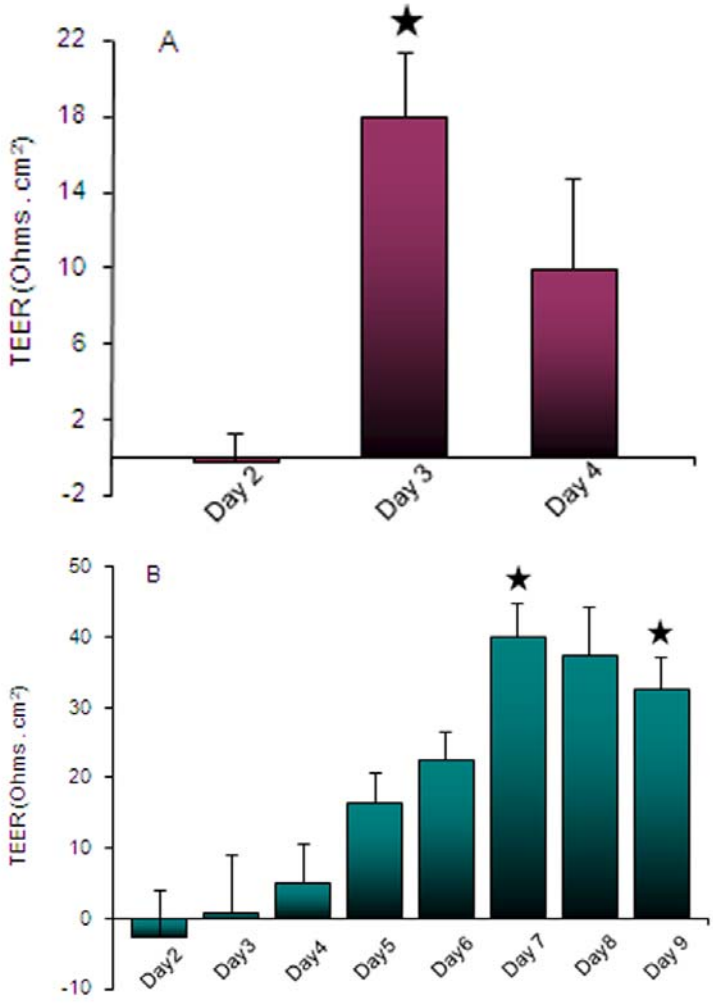

Figure 3.3 | TEER of BAEC (A) and astrocytes (B) over time. TEER was monitored starting one day after culture establishment and continued until a significant reduction was observed. Data is representative of two independent experiments. Results are the means ± SD of three transwells with three measurements each in three independent experiments. Statistical analysis of the data was performed by one-way ANOVA followed by Tukey honestly significant difference test which revealed significant differences ($p < 0.05$) on day 3 (A) and day 7(B). Star represents statistical significance.

Figure 3.4 | TEER of model 1 (A) and model 2 with BAEC (B) or BMEC (C). TEER was monitored on second and third day after EC culture establishment in both models. **(A)** In model 1 when both cell lines are seeded within 8 hrs of each other, TEER of contact (BAEC/Astro) and non-contact (BAEC-Astro) co-cultures are significantly less than TEER of BAEC alone on day 2 and 3. **(B)** In model 2 when BAEC is seeded 3 days after astrocyte culture establishment and both cells reach their peak resistance on day 3, TEER of contact and non-contact co-cultures are equal to TEER of BAEC alone. **(C)** In model 2, when murine BMEC is seeded 3 days after astrocyte culture establishment, TEER of contact co-culture is the same as BMEC alone while TEER of the non-contact co-culture increases 167% compared to BMEC alone. TEER in (A) and (B) is expressed as a normalized % of the BAEC on day 2, and in (C) as a normalized % of the BMEC on day 2. Results are the means ± SD of three transwells with three measurements each in three independent experiments. Statistical analysis of the data was performed by one-way ANOVA ($p < 0.05$) along with linear contrast analysis for contact co-cultures. Star represents statistical significance.

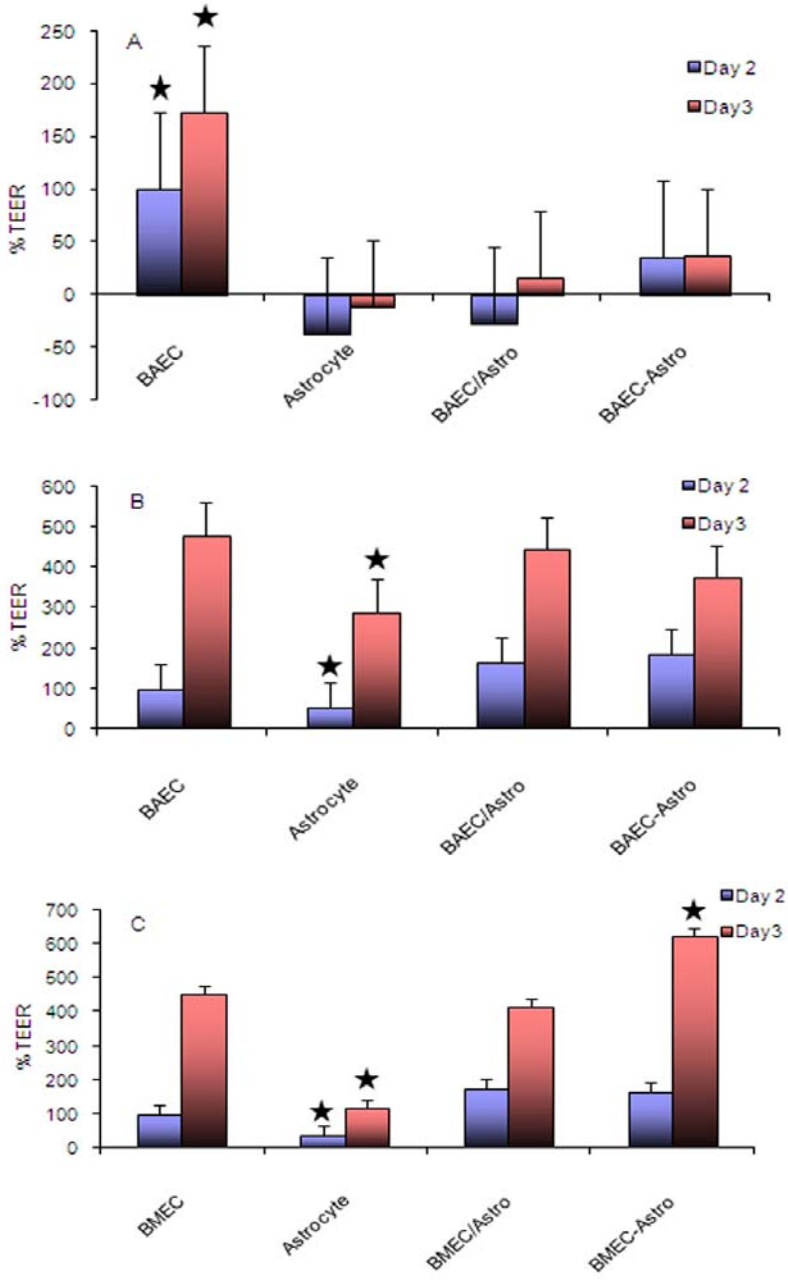
A
% TEER
250
200
150
100
50
0
-50
-100
Day 2
Day3
BAEC
Astrocyte
BAEC/Astro
BAEC-Astro
B
% TEER
600
500
400
300
200
100
0
Day 2
Day3
BAEC
Astrocyte
BAEC/Astro
BAEC-Astro
C
% TEER
700
600
500
400
300
200
100
0
Day 2
Day3
BMEC
Astrocyte
BMEC/Astro
BMEC-Astro

the same as BAEC alone (33.1 ± 5.1 Ω×cm^2) and the resistance of the contact co-culture (30.6 ± 9.1 Ω×cm^2) is not higher than the sum of the resistances of BAEC and astrocytes individually (Figure 3.4 B). However, when model 2 was replicated with murine BMEC (Figure 3.4 C), the resistance of the non-contact co-culture (107.8 ± 3.1 Ω×cm^2) was 167% higher than the BMEC alone (78.9 ± 7.4 Ω×cm^2) indicating induction by astrocytes while the resistance of the contact co-culture (72.1 ± 3.9 Ω×cm^2) was similar to BMEC alone.

3.5.3 Effect of Astrocytes on Permeability of BAEC and Murine BMEC

In both models, permeability of the endothelial layer was monitored by measuring the influx rate of sodium fluorescein from the top compartment of the transwell to the bottom. Representative influx rates over the transwell membrane area correspond to the permeability coefficient for each configuration . In both models, statistical analysis of the data revealed no significant difference between the permeability of BAEC alone (1.9 ± 0.26 10^{-5} cm/s) and non-contact co-cultures (1.92 ± 0.26 10^{-5} cm/s). However, in model 2 with murine BMEC, the permeability of the non-contact co-culture (0.62 ± 0.03 10^{-5} cm/s) decreased significantly compared to the BMEC alone (0.78 ± 0.008 10^{-5} cm/s). Linear contrast analysis revealed no significant difference between the permeability of contact co-cultures (0.696 ± 0.16; 0.54 ± 0.15 10^{-5} cm/s) and the sum of permeabilities of BAEC or BMEC and astrocytes (2.5 ± 0.45 10^{-5} cm/s) individually. Results are the means ± SD of three transwells with three measurements each in three independent experiments.

3.5.4 Immunocytochemical Characterization of BAEC, Murine BMEC, and Astrcoytes

BAEC cultured alone or in the presence of astrocytes displayed a characteristic cobblestone-like appearance upon reaching confluence (Figure 3.5 A), while BMEC displayed characteristic spindle shaped morphology (Figure 3.5 C). The BAEC and BMEC cultures in both models retained their phenotype as judged by the uptake of DiI-Ac-LDL (Figure 3.5 B, D) with the level of staining being higher in BMEC. Astrocytes cultured on the bottom side of the transwell as well as in the multi-well dish, attached and proliferated well and retained their phenotype as judged by GFAP antibody staining (Figure 3.5 E). BAEC alone or in co-culture failed to stain positive for occludin (Figure 3.6 B), indicating the presence of none or very few tight junctions. However, BMEC stained positive for occludin (Figure 3.6 A) and interestingly the patterns of staining in contact co-culture (Figure 3.6 C) and non-contact co-culture (Figure 3.6 D) differed from BMEC alone culture. This confirms the ability of astrocytes to affect BMEC.

3.6 Discussion

For the first time, a complete analysis of TEER, permeability, and immunocytochemistry results on contact and non-contact co-cultures of rat astrocytes and BAEC is provided. In contrast to a previous study [17] reporting that rat astrocytes can induce BBB properties in contact co-cultures with BAEC, we report here on the inability of BAEC to acquire BBB properties in contact and non-contact co-cultures based on study of TEER and permeability of astrocytes alone and linear contrast statistics. Immunocytochemical characterization also indicated minimum expression of junction protein

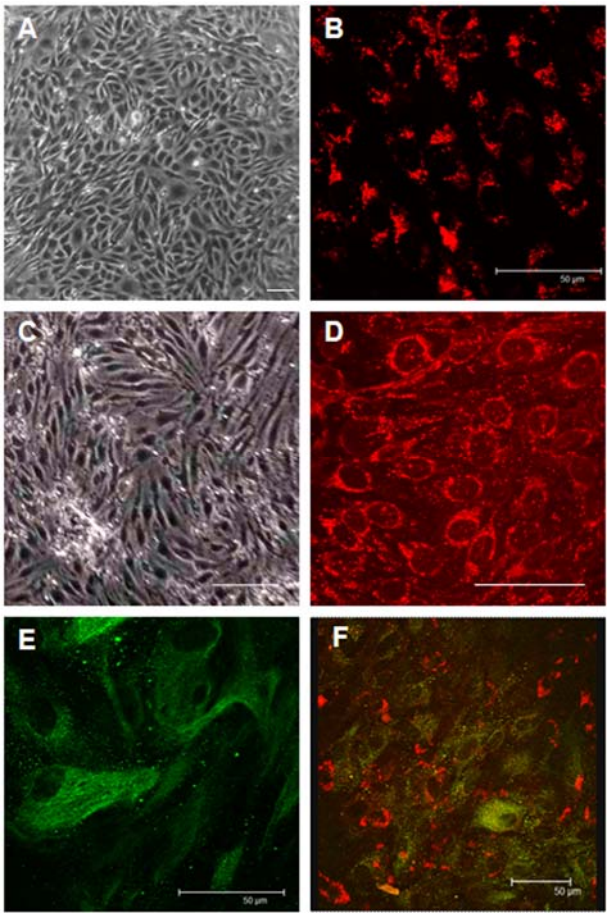

Figure 3.5 | Immunocytochemical characterization of EC and Astrocytes. **(A,C)** Phase contrast image of BAEC (A) and BMEC (C) in transwell. **(B,D)** Immunofluorescent confocal images of BAEC (B) and BMEC (D) probed for uptake of DiI-Ac-LDL. **(E)** Immunofluorescent confocal image of astrocytes probed for glial fibrillary acidic protein (GFAP). **(F)** Immunofluorescent confocal image of contact co-culture probed for uptake of DiI-Ac-LDL and GFAP. Scale bars represent 50 μm.

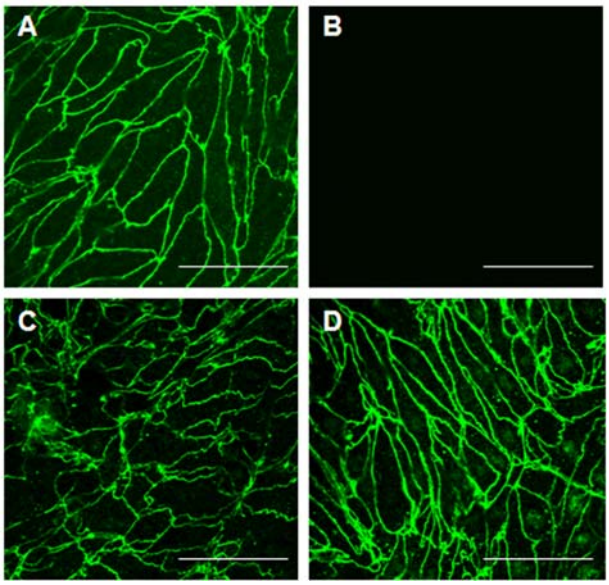

Figure 3.6 | Immunocytochemistry of occludin in BAEC and BMEC. (A-B) Confocal image of BMEC (A) and BAEC (B) stained for occludin. **(C-D)** Confocal image of BMEC in contact (C) and non-contact (D) co-culture with astrocytes stained for occludin. Scale bars represent 50 μm.

occludin, which is an essential component for making tight EC barriers. These results serve as a complement to previous studies reporting zero or very low activities of alkaline phosphatase and γ-glutamyl transpeptidase in BAEC, both of which are up-regulated markers in BMEC and important in *in vitro* BBB models [5,23].

The ability to use rat primary astrocytes to induce rat and bovine BMEC to make tighter junctions *in vitro* is well documented in the literature [5,7-10,12,18]. This induction appears to be due to both astrocytes' soluble factors, as evident in non-contact co-culture models or those that employ astrocyte conditioned-medium, and astrocytes' physical contact with EC, as evident in contact co-culture models [5,7,9,24]. These studies also show that induction seems to be independent of the species of origin of astrocytes and BMEC, meaning that rat astrocytes not only induce rat BMEC, but also bovine BMEC. Here, we have shown for the first time that rat astrocytes can also induce murine BMEC in non-contact co-cultures. This control study with murine BMEC, and previous studies with bovine BMEC, indicated positive induction by rat astrocytes. Thus, it seems plausible that the lack of BAEC induction is a result of the inability of this peripheral EC (i.e. aortic EC) to recognize the induction factors released by astrocytes *in vitro*, and not a result of the heterologous nature of this co-culture. Although Janzer and Raff (1987) provided direct evidence that astrocytes are capable of inducing BBB properties in non-neuronal EC (capillaries of the anterior eye chamber) *in vivo,* our study suggests that care must be taken in applying this conclusion to *in vitro* studies.

In contrast to the previous report [17], this study evaluated the TEER and permeability of the contact co-cultures based on linear contrast statistics.

The previous report [17] failed to subtract the resistance of astrocytes alone culture from contact co-culture results. These measurements help ensure that any change in the TEER and permeability of the contact co-culture is not a result of the addition of astrocytes' and BAEC/BMEC resistance in series, but a result of induction. In the case of BMEC cultures, the use of puromycin provides higher purity cultures so that measurements reflect the TEER and permeability of endothelial cells and not possible neuronal or non-neuronal contaminants [4]. Moreover, we measured how the electrical resistance of astrocytes changes over time. Figure 3.3 B demonstrates that this resistance can reach as high as 40 (Ω x cm^2) (possibly due to the ability of astrocytes to form multi-layers), which is very close to the TEER of rat BMEC without any cellular or biochemical induction [4,18]. This TEER value for astrocytes further emphasizes the importance of statistical methods to analyze co-culture results. Furthermore, this change in astrocytes' resistance properties motivated the creation of two co-cultures to further investigate the quality of the models when both cell lines reach their peak electrical resistance concurrently (model 2) as compared to BAEC reaching their peak but not astrocytes (model 1).

As discussed, the two models are interesting because of the difference in the time when BAEC were co-cultured with astrocytes. Astrocytes used in both models were derived from the same culture batch, while BAEC used in model 2 was one passage older than the one in model 1. We did not expect that BAEC in the two models would behave differently as a result of the difference in passage number, but TEER data (Figure 3.4) indicate that the BAEC used in model 2 had a slightly higher TEER.

Permeability data in both models, and TEER data in model 2 revealed no significant difference between the resistance of co-cultures and the BAEC alone, but TEER data in model 1 (Figure 3.4 A) illustrated that the resistance of co-cultures are significantly less than BAEC alone. We speculated that it is possible that if BAEC are seeded within a few hours of astrocytes' seeding, some soluble factors released by astrocytes may negatively affect BAEC, or that astrocytic proliferation may deplete some nutrients needed by BAEC from the system.

Although this study revealed no significant difference between the properties of BMEC alone and in contact co-culture, care must be used before making general conclusions about whether physical contact is necessary in these models. Properties of the transwell membrane, such as thickness, pore size, and pore density play an important role in determining whether sufficient physical contact, and therefore induction, occurs [7,24]. The pore diameter of the membranes in this study was 400 nm, and the observation regarding the lack of BMEC induction in contact co-culture indicate that this pore size is not large enough to promote extension of astrocyte foot processes, and may even block the passage of soluble factors. This observation is consistent with a previous report by Demeuse *et al.* [7] that indicated astrocyte foot processes did not cross membranes through pores of 450 nm, and therefore did not induce brain EC.

The immunocytochemical characterizations in this study lead to several interesting observations. First, immunostaining against occludin in BAEC revealed that this junctional protein is either not expressed, or expressed at very low levels. Hirase [25] also showed no or minimal expression of occludin in primary aortic EC measured by immunostaining and immunoblotting

compared to brain EC. It is less likely that our observation is due to de-differentiation of BAEC due to passaging because the positive staining for uptake of the Ac-LDL is consistent with BAEC that have not lost their characteristic properties. Second, the change in morphology of the occludin immunostaining in BMEC co-cultures provides further evidence on the inducing effects of astrocytes on BMEC. This morphological change may correlate with increases at the gene expression level, increases at the protein level, or structural changes in occludin such as phosphorylation. Perriere [15] indicated that BMEC co-cultured with astrocytes have higher occludin mRNA levels compared to BMEC alone. However, future characterizations at the protein level are needed to correlate this increased mRNA level with relevant protein levels.

3.7 Conclusion

This study evaluated the induction effects of astrocytes on BAEC, with an emphasis on the resistance properties of astrocytes. The linear contrast statistical analysis revealed that previously reported decrease in permeability of BAEC contact co-cultures, is likely due to the addition of astrocytes' resistance in series and not due to induction. Including BMEC as a control, it was also demonstrated that the EC tissue of origin plays a critical role with respect to induction by astrocytes compared to the species of origin of the two cells (i.e. heterologous models). The lack of occludin expression in BAEC provided further evidence that aortic EC are too leaky to be useful for constructing *in vitro* BBB models.

3.8 Acknowledgements

This work was funded in part by the New York State Office for Science, Technology, and Academic Research (NYSTAR) and the National Science Foundation through the Nanobiotechnology Center (NBTC). We also thank Professor Eric Shusta at University of Wisconsin Chemical Engineering (Madison, WI) for the BMEC primary culture methodologies, Professor John Schimenti and Robert Munroe at Cornell University College of Veterinary Medicine (Ithaca, NY), Professor William Shain at the Center of Neural Communication Technology, Wadsworth Center (Albany, NY), Carol Bayles at Cornell University Life Sciences Core Laboratories Center (CLC), and Professor James Booth at Cornell University Statistical Consulting Unit (CSCU). We also thank Glenn Swan at Cornell University Chemical Engineering machine shop.

REFERENCES

1. Abbott, N.J., 2002. Astrocyte-endothelial interactions and blood-brain barrier permeability. *J. Anat*. 200: 629-638.
2. Rubin, L.L., Staddon, J.M., 1999. The cell biology of the blood brain barrier. *Annu. Rev. Neurosci.* 22: 11-28.
3. Cecchelli, R, Berezowski, V, Lundquist, S, *et al.*,2007. Modeling of the blood-brain barrier in drug discovery and development. *Nature Rev. Drug Discovery* 6: 650-661.
4. Calabria, AR, Weidenfeller, C, Jones, AR, *et al.,* 2006. Puromycin-purified rat brain microvascular endothelial cell cultures exhibit improved barrier properties in response to glucocorticoid induction. *J. Neurochem*. 97: 922-933.
5. Dehouck, MP, Meresse, S, *et al.,* 1990. An easier, reproducible, and mass-production method to study the blood-brain barrier *in vitro*. *J. Neurochem.* 54: 1798-1801.
6. Deli, MA, Abraham, CS, Niwa, M, Falus, A., 2003. *N,N*-diethyl-2-[4-(phenylmethyl)phenoxy]ethanamine increases the permeability of primary mouse cerebral endothelial cell monolayers. *Inflamm. Res.* 52: S39-S 40.
7. Demeuse, P, Kerkhofs, A, *et al.,* 2002. Compartmentalized co-culture of rat brain endothelial cells and astrocytes: a syngenic model to study the blood-brain barrier. *J. Neurosci. Meth*. 121: 21-31.
8. Gaillard, PJ, *et al.,* 2000. Astrocytes increase the functional expression of p-glycoprotein in an *in vitro* model of the blood-brain barrier. *Pharmaceutical Research* 17: 1198-1205.

9. Gaillard, PJ, Voorwinden, LH, *et al.,* 2001. Establishment and functional characterization of an *in vitro* model of the blood-brain barrier, comprising a co-culture of brain capillary endothelial cells and astrocytes. *Euro. J. Pharm. Sci.* 12: 215-222.

10. Perriere, N, Demeuse, PH, *et al.,* 2005. Puromycin-based purification of rat brain capillary endothelial cell cultures. Effect on the expression of blood-brain barrier specific properties. *Journal of Neurochemistry* 93: 279-289.

11. Weidenfeller, C, Schrot, S, *et al.,* 2005. Murine brain capillary endothelial cells exhibit improved barrier properties under the influence of hydrocortisone. *Brain Research* 1053: 162-174.

12. Weidenfeller, C, Svendsen, CN, Shusta, E., 2007. Differentiating embryonic neural progenitor cells induce blood-brain barrier properties. *Journal of Neurochemistry* 101: 555-565.

13. Nag, S., 2003. The blood-brain barrier: biology and research protocols. New Jersey: Humana Press.

14. Hurwitz, AA, Berman, JW, Rashbaum, WK, Lyman, WD., 1993. Human fetal astrocytes induce the expression of blood-brain barrier specific proteins by autologous endothelial cells. *Brain Research* 625: 238-243.

15. Perriere, N, Yousif, S, *et al.,* 2007. A functional *in vitro* model of rat blood-brain barrier for molecular analysis of efflux transporters. *Brain Research* 1150: 1-13.

16. Hayashi, Y, Nomura, M, *et al.,* 1997. Induction of various blood-brain barrier properties in non-neural endothelial cells by close apposition to co-cultured astrocytes. *Glia* 19: 13-26.

17. Isobe, I, Watanabe, T, *et al.,* 1996. Astrocytic contributions to blood-brain barrier (BBB) formation by endothelial cells: a possible use of aortic endothelial cell for *in vitro* BBB model. *Neurochem. Int*. 28: 523-533.

18. Rubin, LL, Hall, DE, *et al.,* 1991. A cell culture model of the blood-brain barrier. *J. Cell Biol.* 115: 1725-1735.

19. Janzer, RC, Raff, MC., 1987. Astrocytes induce blood-brain barrier properties in endothelial cells. *Nature* 325: 253-257.

20. Kacem, K, Lacombe, P, *et al.,* 1998. Structural organization of the perivascular astrocyte end-feet and their relationship with the endothelial glucose transporter. *Glia* 23: 1-10.

21. Davis-Cox, MI, Turner, JN, *et al.,* 1994. Phorbol ester-stimulated stellation in primary cultures of astrocytes from different brain regions. *Microsc. Res. Tech.* 29: 319-327.

22. Everitt, BS., 2002. The Cambridge dictionary of statistics. London, UK: Cambridge University press.

23. Gordon, EL, Danielsson, PE, *et al.,* 1991. A comparison of primary cultures of rat cerebral microvascular endothelial cells to rat aortic endothelial cells. *In vitro Cell Dev. Biol.* 27A: 312-326.

24. Harris, Ma S, Lepak, LA, *et al.,* 2005. An endothelial and astrocyte co-culture model of the blood-brain barrier utilizing an ultra-thin, nanofabricated silicon nitride membrane. *Lab on a chip* 5: 74-85.

25. Hirase, T, Staddon, JM, *et al.,* 1997. Occludin as a possible determinant of tight junction permeability in endothelial cells. *Journal of Cell Science* 110: 1603-1613.

CHAPTER 4

SYNTHESIS AND CHARACTERIZATION OF HIGH-THROUGHPUT NANOFABRICATED POLY(HYDROXY STYRENE) MEMBRANES FOR *IN VITRO* MODELS OF BARRIER TISSUE

4.1 Preface

This chapter is adapted from: Shayan, G., Felix, N., Chatzichristidi, M., Shuler, M. L., Ober, C. K., Lee, K. H., 2010. Synthesis and characterization of high-throughput nanofabricated poly(hydroxy styrene) membranes for *in vitro* models of barrier tissue. *Biomaterials*, in preparation. It reports on the synthesis, nanofabrication, and characterization of high throughput 3 μm thick membranes based on poly(hydroxy styrene). These membranes can be used as an alternative to current commercially available permeable supports for transport studies across *in vitro* models of barrier tissue.

4.2 Abstract

Commercially available permeable supports with microporous membranes have led to significant improvements in the culture of polarized cells because they permit them to feed basolaterally and thus carry out metabolism in a more *in vivo* like setting. The porous nature of these membranes enable permeability measurements of drugs or biomolecules across the cellular barrier. However, current porous membranes have a high flow resistance due to great thickness (20-40 μm), low porosity, and a wide pore size distribution with tortuous diffusion paths which make them low-throughput for permeability studies. Here we describe an alternate platform that is more flexible, allows for

more control over physical parameters of the membranes, and is high-throughput. This study reports on the synthesis and nanofabrication of a 3 μm thick, transparent membrane based on poly(hydroxy styrene). The membranes are nanofabricated using electron beam lithography and deep ion plasma etching to achieve an organized array of straight pores from 50 nm to 800 nm in diameter, with at least 23 times less flow resistance. It also shows for the first time the potential utility of poly(hydroxy styrene) as a cell culture substrate with lack of cytotoxicity, and with suitability for nanofabrication processes due to temperature stability.

4.3 Introduction

The development of culture vessels and cell attachment substrates has been driven by the need to produce an environment that resembles the *in vivo* state as closely as possible to enable the growth of specialized cell types. In the case of polarized cells, such as epithelial cells and endothelial cells involved in barrier tissues, commercially available permeable supports with microporous membranes have become the standard tool for cell culture. This technology has led to significant improvements in the culture of polarized cells because it permits basolateral feeding of cells which facilitates metabolism in a more *in vivo* like setting [1,2]. As an example, it is well established that epithelial cells such as MDCK and Caco-2 cells appear squamous and display poor cell polarity when grown on solid plastic. However, when these cells are grown on permeable supports their morphology dramatically alters to become cuboidal and columnar respectively and both display good cell polarity [3]. Moreover, cellular functions including transport, adsorption, and secretion can also be

studied because the permeable supports provide convenient and independent access to apical and basolateral plasma membrane domains [3,4].

Microporous membranes in commercially available permeable supports are either made of polyester (partially transparent) or polycarbonate (translucent). They are 20-40 μm thick depending on the manufacturer, and their pore diameter is either 0.4 μm, 1.0 μm, or 3.0 μm with their nominal pore density being 4×10^6 (polyester) and 1×10^8 (polycarbonate) pores/cm^2. Even though polycarbonate membranes possess higher porosity, they are not commonly used in cell culture applications due to the difficulty in performing microscopy on them. The process of fabrication of these membranes results in a random distribution in the size and placement of pores, and more importantly the resulting diffusion path is tortuous causing entrapment of biomolecules [5-12]. Thus, a key drawback of current commercial permeable supports is their high flow resistance due to a wide pore size distribution with tortuous paths, the low total porosity, and the relatively thick membrane which makes them low-throughput for permeability studies [8-12].

Here we describe an alternate platform that is more flexible, versatile in its physical characteristics, and most importantly high-throughput. A 3 μm thick, transparent polymeric membrane based on poly(hydroxy styrene) (PHOST) was synthesized. The membranes were then nanofabricated using a combination of electron beam lithography with deep ion plasma etching to achieve an organized array of straight pores with a narrow size distribution (50 nm to 800 nm in diameter). The porosity of the membrane is 8×10^6 pores/cm^2, which is two times more than commercial membranes. These membranes have at least 23 times less flow resistance compared to their commercial counterparts, making them ideal for high-throughput permeability studies.

Moreover, we report on preliminary cell culture studies, showing the successful attachment and growth of several cell lines commonly used in *in vitro* models of the blood-brain barrier and the intestinal barrier, with focus on the viability, rates of metabolism, and differentiation of the cells on the nanofabricated membranes.

4.4 Materials and Methods

4.4.1 Chemicals and Supplies

Solvents and reagents for the polymer synthesis were obtained from Sigma (St. Louis, MO, USA) and used without further purification unless otherwise stated. Twelve well Transwell® permeable support (polyester; pore size, 0.4 μm; pore density, $4x10^6$ pores/cm^2) was purchased from Corning (Lowell, MA, USA). Poly-D-lysine and collagen type I were purchased from Fisher Scientific (Pittsburg, PA, USA). Human fibronectin was purchased from Millipore (Billerica, MA, USA). EGM® MV and trypsin-EDTA were purchased from Lonza (Basel, Switzerland). Alamar Blue, fetal bovine serum (FBS), and Dulbecco's Modified Eagle Medium (DMEM, with L-glutamin, sodium pyruvate, and low glucose), polyclonal rabbit anti-glial fibrillary acidic protein (GFAP) antibody (18-0063), rabbit anti-occludin antibody (71-1500), Alexa Fluor® 488 goat anti-rabbit IgG antibody (A11008), and 4',6-diamidino-2-phenylindole (DAPI) dihydrochloride nuclear stain were also purchased from Invitrogen (Carlsbad, CA, USA). Dulbecco's phosphate buffered saline (DPBS, without $CaCl_2$ and $MgCl_2$), HEPES sodium salt, Triton X-100, goat serum, fluorescein sodium salt, and gentamicin were purchased from Sigma (St. Louis, MO, USA). Paraformaldehyde (16%) was purchased from Electron Microscopy Sciences (Ft. Washington, PA, USA). Acetylated low density lipoprotein labeled with

1,1'-dioctadecyl-3,3,3',3'-tetramethylindo-carbocyanine percholorate (DiI-Ac-LDL) was purchased from Biomedical Technologies (Stoughton, MA, USA).

4.4.2 Polymer Synthesis

The reactions used for the preparation of PHOST is based on a modified reaction scheme (Figure 4.1) [13-14]. Poly(tert-butoxy styrene) was synthesized by free radical polymerization. Briefly, 7.5 mL of 4-*tert*-butoxy styrene (99%) was polymerized in 5 mL of anhydrous toluene at 65ºC with 10 mg of re-crystallized *α,α'*-Azoisobutyronitrile (AIBN) as the initiator. All glassware was flame dried prior to use and the reaction mixture was purged with dry argon for 10 minutes. Polymerization was carried out for 19 hours and then terminated in 800 mL of 4ºC methanol. Poly(*tert*-butoxy styrene) was converted to PHOST by a hydrolysis reaction. First, it was dissolved in 20 mL of 1,4-dioxane, and then 50 mL of 4M hydrochloric acid in dioxane solution (5-fold) was added. The mixture was reacted at 80ºC under reflux for 24 hours and then precipitated in 800 mL 4ºC water. After neutralization with NaOH solution to a pH value of 7 – 7.5, the resulting polymer was filtered and lyophilized for 48 hours.

4.4.3 Polymer Characterization

Gel permeation chromatography (GPC) measurements were performed using THF as elution solvent at a flow rate of 1 mL/min in a Waters size exclusion chromatograph (SEC). ^{1}H-NMR spectroscopy was performed on 300 MHz Mercury 300 NMR instrument using $CDCl_3$ and DMSO-d_6 as solvents. FTIR measurements were carried out on a Mattson 2020 Galaxy series instrument.

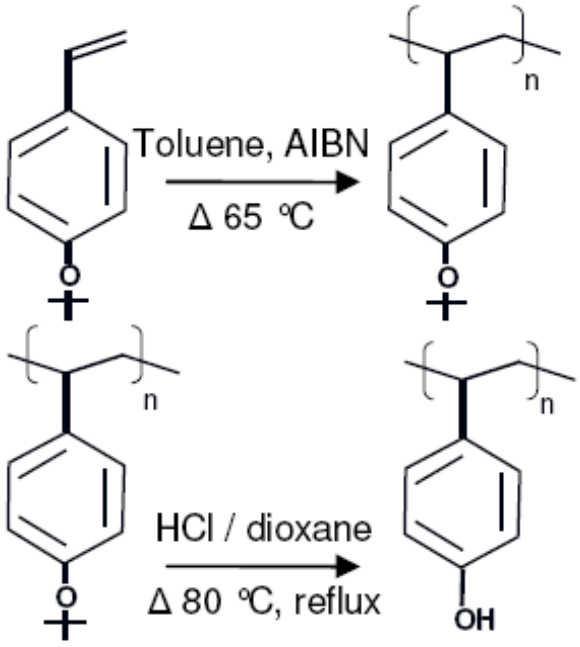

Figure 4.1 | Synthesis of PHOST.

Thermal analysis was carried out on a TA instrument DSC (DSCQ1000) and a TA instrument TGA (TGAQ500).

4.4.4 Nanofabrication Process

Figure 4.2 illustrates the fabrication process that was applied to obtain spatially controlled nanopores. Briefly, a silicon substrate was cleaned with oxygen plasma (standard recipe) in an Oxford Plasmalab 80+ RIE system for 2 minutes. A solution of poly(acrylic acid) (PAA, 20 wt% in water) was spin-coated at 2000 rpm for 45 seconds on the substrate followed by baking at 130ºC for 5 seconds. The layer thickness was 200 nm by profilometry. Following the deposition of the PAA layer, a solution of PHOST (15 wt% in propylene glycol methyl ether acetate) was spin-coated at 1100 rpm for 30 seconds followed by baking at 130°C for 1 minute. The layer thickness was 3 μm by profilometry (at least four scratches were made on the film at different locations using a razorblade and the depth of each scratch was measured at three different locations). Low stress thermally grown SiO_2 was deposited using the IPE 1000 plasma enhanced chemical vapor deposition system at 115°C for 5 minutes. The layer thickness was 200 – 300 nm. ZEP-520A (positive electron beam resist) was spin-coated at 4000 rpm for 1 minute and baked at 115°C for 2 minutes. Leica VB6-HR electron beam lithography system (100 kV) was used to write a hexagonal pattern of octagons with the current at 1 nA and the exposure dose at 1500 μC/cm^2. The pore diameters were either 50 nm, 200 nm, 400 nm, 600 nm, or 800 nm with 5 μm center to center spacing. The pattern area was a square with an area of 0.25 cm^2. The exposed samples were developed at 4°C in ZED-N50 for 1 minute, followed by methyl isobutyl ketone (MIBK) for 30 seconds, and finally isopropyl alcohol

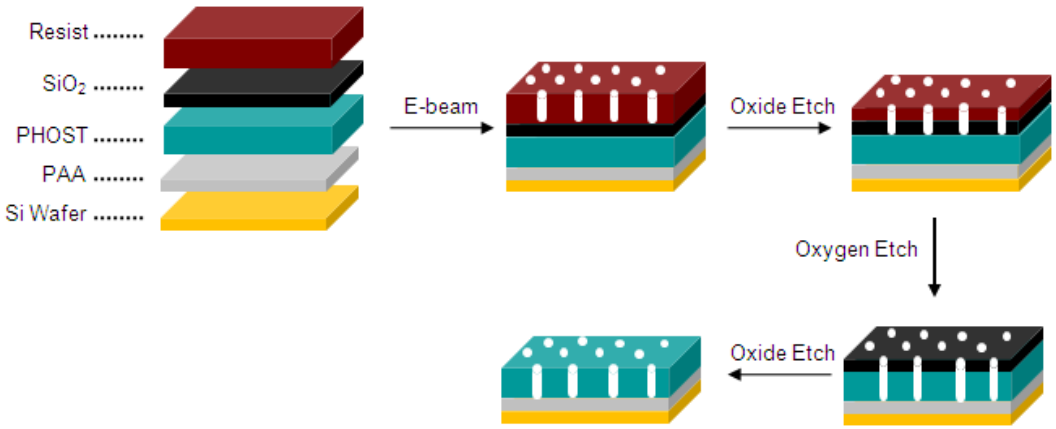

Figure 4.2 | Nanofabrication scheme for obtaining spatially controlled nanopores. PHOST was spincoated on a Silicon wafer, followed by the deposition of low stress SiO_2 layer, and electron beam resist. After electron beam exposure, samples were developed at 4°C. A three step etch process was used to etch through the SiO_2 layer followed by the PHOST. The final oxide etch removes the SiO_2 layer. Porous membranes are detached from the Si wafer by placing them in water and thus dissolving the PAA layer.

(IPA) for 1 minute. The SiO_2 mask was etched with a CHF_3/O_2 recipe in an Oxford Plasmalab 80+ RIE system for 6 minutes, and the PHOST was etched with an oxygen plasma clean recipe in an Oxford Plasmalab 100 RIE system for 2 minutes. Finally, the SiO_2 mask was removed with the CHF_3/O_2 recipe for 5 minutes. Pore dimensions were characterized using Zeiss Ultra scanning electron microscope at 3 kV.

4.4.5 Cell Culture Maintenance

Astrocytes isolated from 3 days old Wistar rat pups were provided by Dr. W. Shain (Wadsworth Center, Albany, NY) following established techniques [15]. Cells were maintained in DMEM (low glucose, with L-glutamine and sodium pyruvate) supplemented with 5% FBS and gentamicin at the supplier's recommended concentration. Cells were grown on 75 cm^2 tissue culture flasks at passage 0 and were fed every 3 days by completely replacing the medium.

Cryo-preserved, single donor, bovine aortic endothelial cells (BAEC) were purchased from Lonza (Basel, Switzerland) at passage 1. Cells were thawed, maintained, and sub-cultured according to the supplier's recommendations. In summary, cells were maintained in endothelial basal medium supplemented with bovine brain extract, heparin, human epidermal growth factor, hydrocortisone, gentamicin-amphotericin, and 10% fetal bovine serum (EGM® MV). Cells were grown on 25 cm^2 tissue culture flasks and used at passage 6 for experiments.

Human colon carcinoma cells (Caco-2) were maintained in DMEM with 4.5 g/L glucose, 25 mM HEPES buffer, 4 mM L-glutamine, and 10% FBS. Cells were used at passage 34. All cultures were maintained in a 37°C humidified cell culture incubator with 5% CO_2.

4.4.6 Cell Culture on Nanofabricated Membranes

The PHOST membrane was detached from the silicon substrate after the fabrication process by placing it in water. This step dissolved the PAA layer and ensured detachment of the membrane from the substrate. An in-house support device was designed and made from polycarbonate (Figure 4.3). The membrane was chemically attached to the device using methylene chloride. After membrane attachment, the device was placed in a 12-well culture dish and incubated in an antibiotic solution (100 U/mL penicillin, 100 µg/mL streptomycin, and 0.25 µg/mL amphotericin) for 4 hours in culture incubator for sterilization. The membrane was washed with DPBS prior to cell culture.

For astrocyte attachment, both the membrane and a control commercially available permeable support were treated with 5 µg/cm^2 of poly-D-lysine in DMEM without serum for 4 hours in the culture incubator. Before use, poly-D-lysine was aspirated and the surface was rinsed once with DPBS. Astrocytes (passage 1) were seeded at 50,000 cells/cm^2 on both surfaces. For BAEC, the membrane and the control surface were treated with 10 µg/cm^2 of human plasma fibronectin in DMEM without serum for 20 minutes in the culture incubator. Before use, fibronectin was aspirated and the surface was rinsed once with DPBS. BAEC (passage 6) were seeded at 20,000 cells/cm^2 on both surfaces. For Caco-2 attachment, the membrane and the control surface were treated with 8 µg/cm^2 of collagen type I in water for 20 minutes in the culture incubator. Before use, collagen was aspirated and the surface was rinsed once with DPBS. Caco-2 (passage 34) were seeded at 100,000 cells/cm^2 on both surfaces.

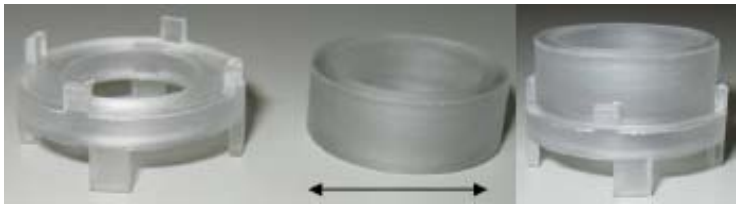

Figure 4.3 | Cell culture support device. After detachment of fabricated membranes from the Silicon wafer, they are chemically attached to the top cylindrical segment of the device using methylene chloride. The top segment will then sit firmly inside the bottom segment with the membrane dividing the chambers. The device fits inside a 12-well culture dish. The inner diameter (arrow) is 1.12 cm.

Cells were observed with an Olympus inverted phase contrast microscope and pictures were captured with a Retiga 1300 CCD camera 1 day and 4 days after culture establishment.

4.4.7 Immunocytochemistry

DiI-Ac-LDL was diluted to 10 µg/mL in EGM® MV and added to BAEC. The cells were then incubated in a 37°C humidified cell culture incubator with 5% CO_2 for 4 hours. The cells were rinsed three times with DPBS and then fixed in 4% (w/v) paraformaldehyde at room temperature for 20 minutes.

Astrocyte and Caco-2 cultures were rinsed twice with DPBS followed by fixation in 4% paraformaldehyde for 20 minutes (all steps performed at room temperature unless stated otherwise). Following three 5 minute rinses in DPBS, astrocytes were permeabilized with 0.1% Triton X-100 in DPBS for 15 minutes, and Caco-2 cells were permeabilized with 0.05% Triton X-100 for 5 minutes on ice. (Caco-2 cells were also pre-permeabilized with 0.2% Triton X-100 for 2 minutes on ice for occludin staining). After three 5 minute rinses in DPBS following permeabilization, astrocytes and Caco-2 cells were blocked in 10% goat serum in DPBS for 15 minutes. All subsequent steps were performed on a shaker. The following concentrations in 10% goat serum were used for primary antibodies: rabbit anti-GFAP 4 µg/mL, and rabbit anti-occludin 15 µg/mL. Primary antibodies were added to the appropriate compartment for 1 hour followed by three 10 minutes rinses in 1% goat serum (occludin incubation was done at 4°C). Cells were incubated for 1 hour in 1:500 dilution of Alexa Fluor® 488 goat anti-rabbit IgG antibody followed by three 10 minutes rinses in 1% goat serum. DAPI was added in 300 nM for 3 minutes prior to mounting the membrane on a glass slide with a cover slip in

Vectashield mounting medium. Samples were observed in a Leica SP2 scanning confocal microscope (Leica Microsystems Inc., Bannockburn, IL, USA).

Control samples were treated exactly as stated above, except that the primary antibodies were replaced with a rabbit IgG fraction negative control. A secondary antibody-only control was also included.

4.4.8 Cell Metabolism and Viability Assays

Alamar Blue (AB) assay, a fluorometric indicator of cell metabolic activity, was used to determine cell metabolic rate [16-17]. Prior to the experiment and according to the manufacturer's protocol, the seeding density and incubation period consistent with linear reduction of AB was determined by seeding cells at various densities and monitoring AB reduction over 72 hours. This initial study indicated that for the seeding densities reported for all three cell lines in the former section, the maximum incubation time in which the cells turn AB from the oxidized form (blue) to the fully reduced form (red) is 24 hours, with the signal from the first 6 hours being linear. Thus, twenty four hours post seeding, all cultures were fed with a 10% (v/v) solution of AB in culture medium and allowed to incubate for 6 hours in the incubator. The fluorescence was measured at room temperature every hour in a fluorescent plate reader (Molecular Devices SpectraMax Gemini EM) using an excitation and emission wavelength of 540 nm and 590 nm, respectively. The fluorescence of an empty culture dish and the culture medium were also measured as controls. At day 4, all cultures were washed with DPBS and cells were trypsinized from the surface. Cell viability was determined with a hemocytometer using 50% Trypan Blue.

Three independent experiments were performed with *n=4* in each experiment. The statistical analysis was carried out using JMP® 7.0 (SAS Institute Inc., Cary, NC, USA). Statistical significance was determined using one-way analysis of variance (ANOVA) with the global risk fixed at $p < 0.05$. All results are mean ± standard deviation (SD).

4.4.9 Flux Measurements

The top and bottom compartments of the commercial and nanofabricated membranes were pre-equilibrated with transport buffer (10 mM HEPES). A solution of sodium fluorescein (376 Da, water soluble) in transport buffer was then added to the upper compartments to yield a final concentration of 1 μM. Aliquots (100 μL) were removed from the bottom compartment for later analysis in a plate reader and the volume replaced with transport buffer every 15 minutes over 60 minutes. The rate of influx of sodium fluorescein into the bottom compartment divided by the total porous area equals the flux [18].

4.5 Results and Discussion

Although several attempts have been made to create high flux membranes [8-12], they are usually targeted towards separation and microfiltration processes by creating silicon nitride or silicon oxide nano-films or nano-sieves with limited pore sizes (<100 nm) and random pore arrangement. Due to the proposed application as well as the extreme fragility of the above membranes, these studies come short in showing the absence of cytotoxicity and appropriateness for cell culture and tissue engineering. In this study, selection of the appropriate polymer involved consideration of two factors. First, the material should lack cytotoxicity and require minimum post-fabrication modifications for

cell attachment mainly due to the inherent fragility of a 3 μm thick membrane and preference over minimal manipulations. Second, the polymeric membrane should have enough thermal resistance to withstand high temperatures needed at various nanofabrication steps. This study proposes the potential utility of PHOST as a cell culture substrate with suitability for nanofabrication processes for the first time. PHOST was chosen over poly(styrene) because the presence of the negatively charged hydroxyl group makes it a better candidate for cell attachment. More importantly, since the hydroxyl group was incorporated into the polymer during the synthesis, the need for post-fabrication treatment was eliminated.

4.5.1 Synthesis and Characterization of PHOST

PHOST was prepared in a novel reaction scheme by free radical polymerization and subsequent hydrolytic de-protection (Figure 4.1). The molecular weight before de-protection was 186,000 g/mol. GPC results indicated that the molecular weight distribution (PDI) is 1.7. The high molecular weight of PHOST is necessary to ensure proper mechanical stability at 3 μm thickness. While Higashimura *et al.* (1989) proposed a living cationic polymerization scheme for PHOST synthesis, our free radical polymerization scheme is superior because it is faster, does not require in-lab preparation of reactants, is capable of creating high molecular weight PHOST, and involves safer chemicals.

The chemical composition of both polymers was determined by ^{1}H-NMR spectroscopy (Figure 4.4). A chemical shift of 1.2 ppm corresponds to the *tert*-butyl group of poly(*tert*-butoxy styrene) in $CDCl_3$. The spectrum of PHOST in DMSO-d_6 shows a peak at 8.9 ppm, which corresponds to the

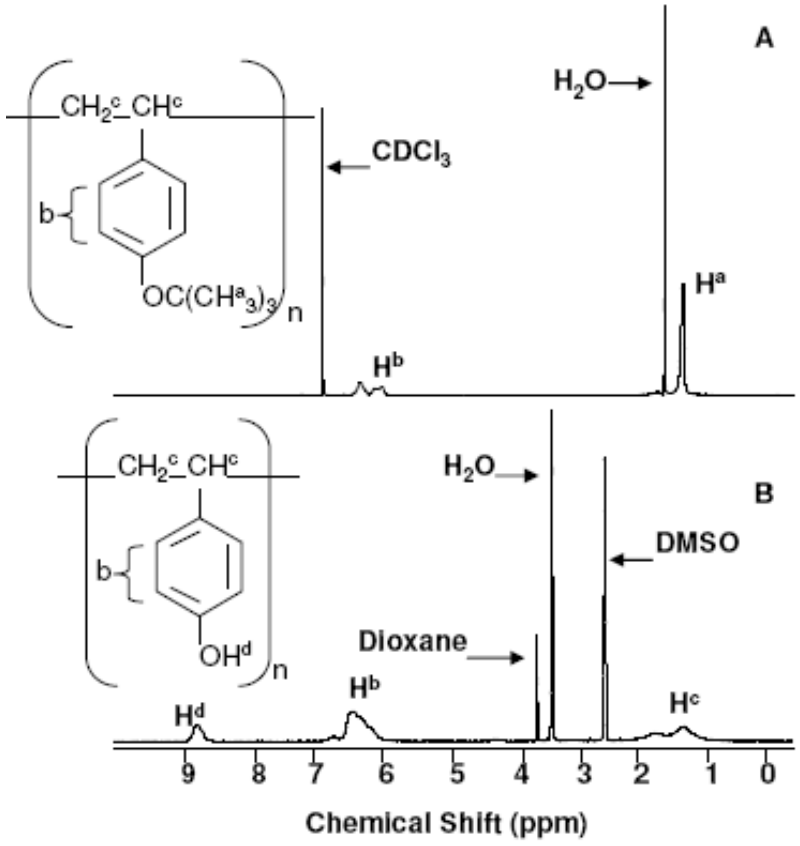

Figure 4.4 | ^{1}H-NMR spectrum of poly(*tert*-butoxy styrene) in $CDCl_3$ (A) and PHOST in DMSO-d_6 (B).

hydroxyl group after the de-protection reaction. The polymer backbone protons appear in the chemical shift region of 1-2 ppm with the signal due to the *tert*-butyl group being disappeared. The FTIR spectrum of PHOST shows a peak at 3380 cm^{-1}, which corresponds to the presence of the hydroxyl group after de-protection (Figure 4.5). The disappearance of the peak at 1132 cm^{-1} indicates complete removal of the *tert*-butyl ether group during hydrolysis.

Differential Scanning Calorimetry (DSC) was carried out on both polymers (Figure 4.6). The T_g of both poly(*tert*-butoxy styrene) and PHOST is approximately 180°C. Thermogravimetric analysis (Figure 4.7) indicated no significant weight loss in PHOST bellow 361°C. The significant weight loss at 220°C in poly(*tert*-butoxy styrene) is due to decomposition of the *tert*-butyl group.

4.5.2 Characterization of Nanofabricated Membranes

Here we describe a nanofabrication scheme that is used for the first time to create high resolution porous structures directly on the membranes. Although traditional photolithography approaches have long been used in creating micro-patterned surfaces, electron beam introduces a higher level of precision and resolution. Furthermore, the proposed fabrication scheme provides flexibility over the choice of polymer. Also, the process is not limited to thin (<500 nm) conducting films (as seen in the semiconductor/mask nano-patterning using electron beam) due to the presence of an internal mask (SiO_2). SiO_2 is resistant to oxygen etch, and thus can be selectively used as an internal mask to transfer the e-beam pattern to PHOST or other underlying polymers with thicknesses in the micron or nanometer range. Susceptibility of the SiO_2 layer to oxide etch however makes its removal easy.

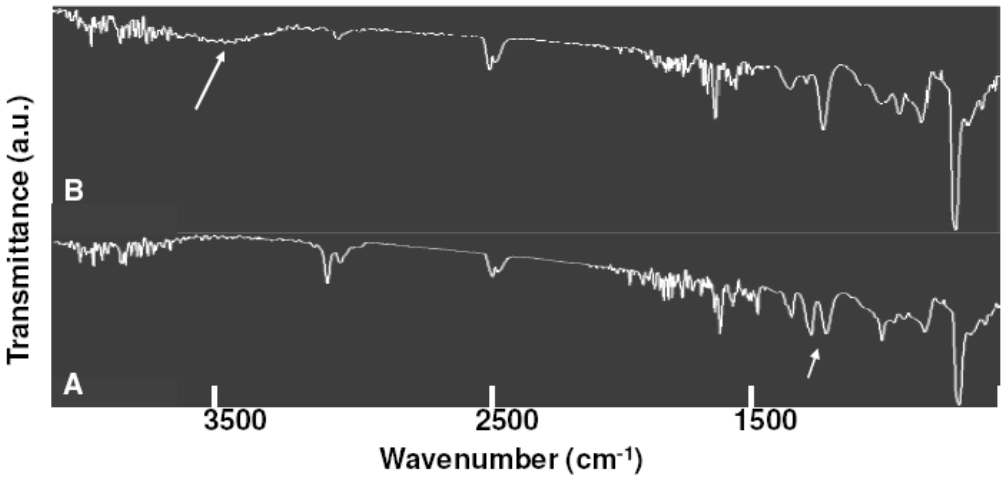

Figure 4.5 | FTIR spectra of poly(*tert*-butoxy styrene) (A) and PHOST (B). Arrows correspond to 1132 cm^{-1} (A) and 3380 cm^{-1} (B).

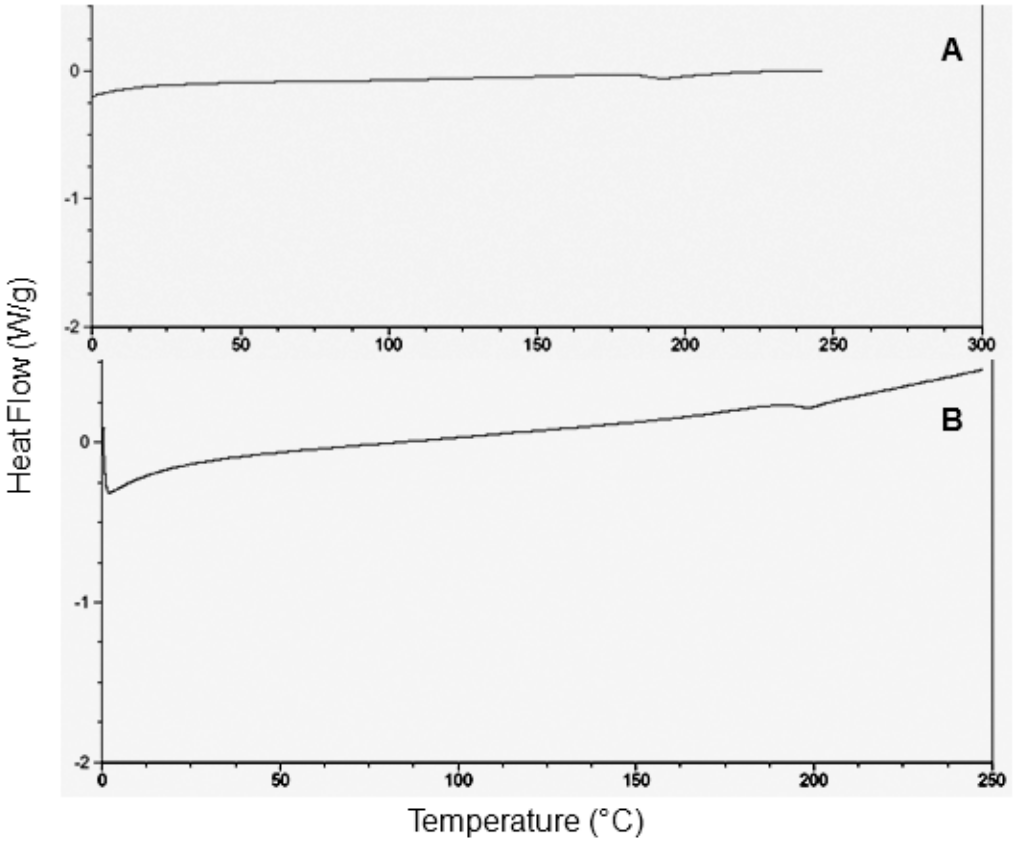

Figure 4.6 | DSC analysis of poly(*tert*-butoxy styrene) (A) and PHOST (B). T_g of both polymers is at 180°C.

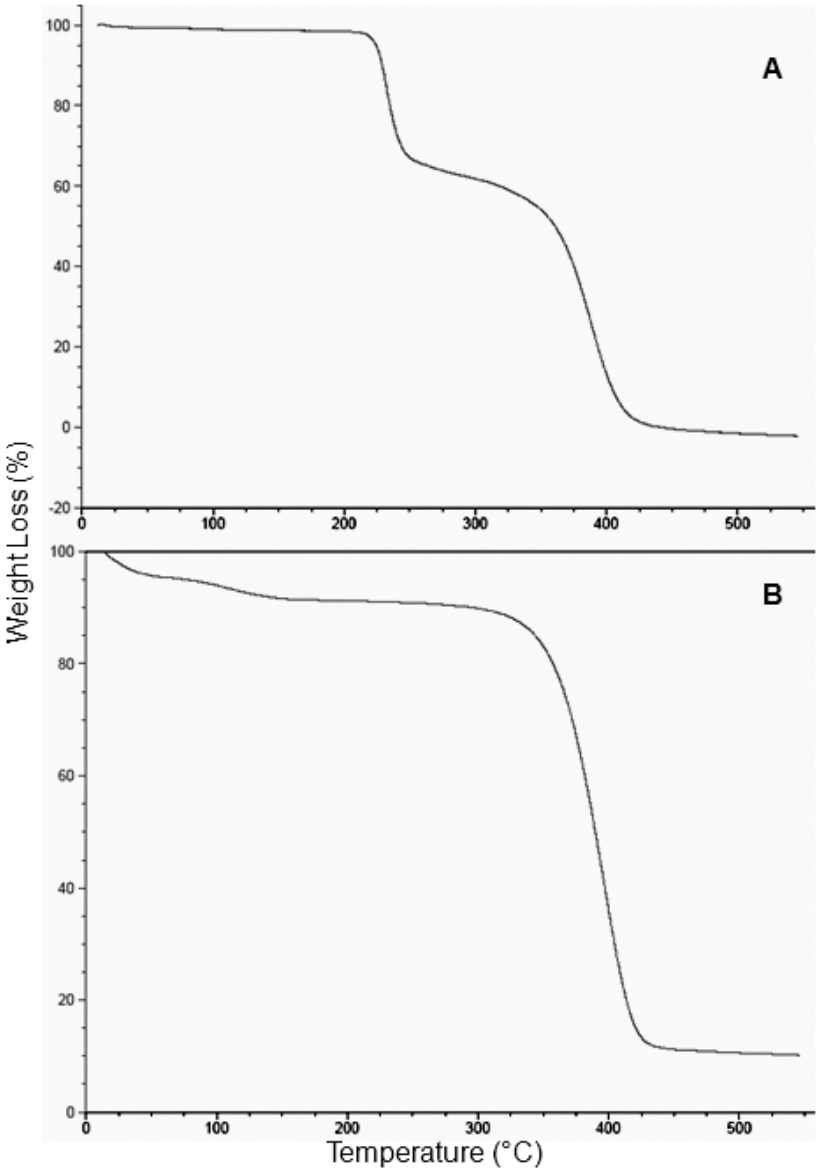

Figure 4.7 | TGA analysis of poly(*tert*-butoxy styrene) (A) and PHOST (B). The significant weight loss at 220°C in (A) is due to decomposition of the *tert*-butyl group.

The PAA layer ensures the complete detachment of fabricated PHOST from the Si wafer once the sample is placed in water. Due to extreme hygroscopic properties of PAA, it makes a uniform film on the Si wafer only after O_2 plasma cleaning of the wafer [19]. The thickness of the PAA layer and PHOST were 200 nm and 3 μm respectively by profilometry. The thickness of PHOST was chosen based on its mechanical stability and ease of handling in cell culture.

ZEP-520A (positive electron beam resist) was specifically chosen over more traditional PMMA due its high resolution and more importantly high etch resistance [20]. The etch-resistance ensured the complete transfer of pattern from ZEP layer all the way down to the SiO_2 layer during the CHF_3/O_2 etch process. Cold development temperature was also used to minimize increase in the pattern dimensions [21-22]. After the O_2 plasma etching of PHOST, pores with sloped sidewalls measuring 150-250 nm larger than the target size on the patterned side (top side) were typically observed. Figure 4.8 shows SEM images of the top-view and cross-section of membranes. The process is capable of producing pores with diameters in the range of 50-800 nm.

After detachment of a fabricated membrane from the Si wafer, it was attached to the top cylindrical segment of the in-house support device (Figure 4.3) using methylene chloride. Even though this may change the thickness and chemistry of the membrane at the attachment site (the cross-sectional thickness of the ring is 0.2 cm), the chemical attachment is fully controllable with respect to creating a leak-proof chamber. Moreover, the inner diameter of the support device (and hence the membrane) is 1.12 cm, with the nanofabricated portion being a square located at the center of the support device (the area of the nanofabricated square is 0.25 cm^2). Thus, the

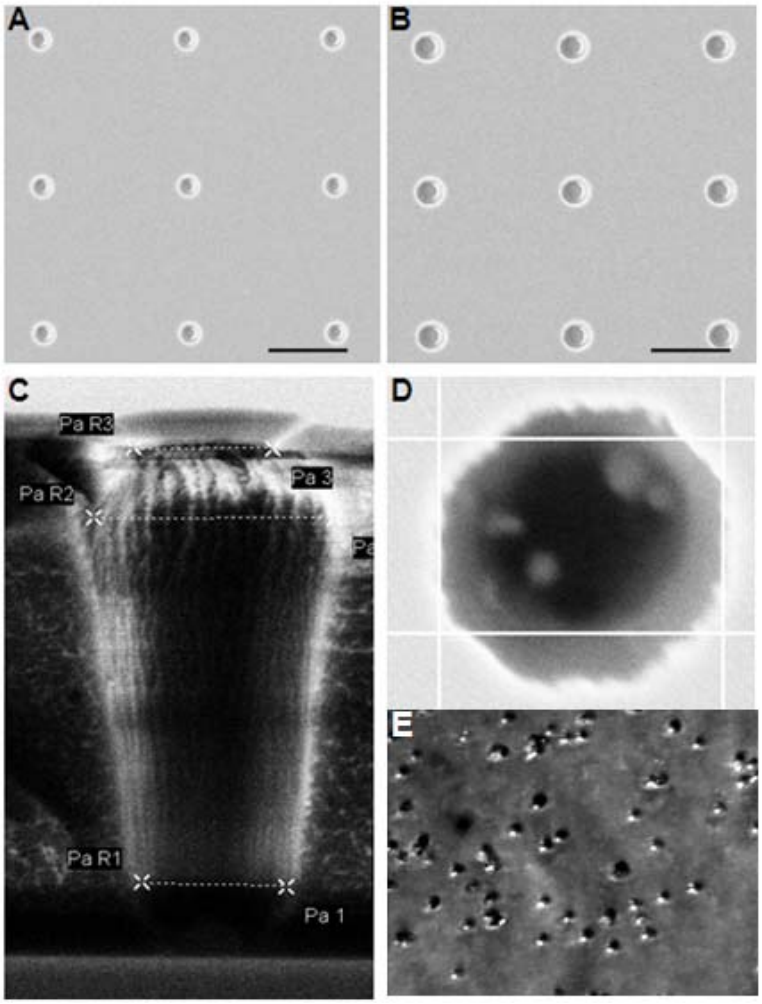

Figure 4.8 | Top and cross-sectional views of the porous membrane. Top views of 400 nm pores (A) and 600 nm pores (B). Scale bar is 2.5 μm. (C-D) shows the cross-section and an angled top view of a 600 nm pore. The larger diameter at the top is 828 nm, and the smaller diameter at the bottom is 566 nm. (E) Top view of a commercial polyester membrane with 400 nm pores. The pores are randomly distributed and they are not uniform in size.

nanofabricated region is 0.31 cm away from the attachment site in every direction.

4.5.3 Cell Viability, Rate of Metabolism, and Differentiation

To test the lack of cytotoxicity and cell culture handling ability of very thin nanofabricated membranes, astrocytes, BAEC, and Caco-2 cells were cultured on PHOST with pores 400 nm in diameter. This pore size was selected because the smallest available pore size in commercial permeable supports is 400 nm. The three cell lines were chosen to show that the membrane is generally applicable to the culture of any cell type, and more importantly because these cells are commonly used in constructing *in vitro* models of barrier tissues, blood-brain barrier (BAEC and astrocytes) and the intestinal barrier (Caco-2).

AB was used to determine cell metabolic rate [16-17]. AB is a water-soluble dye that contains a fluorometric/colorimetric redox indicator that changes from the oxidized to the reduced form in response to the chemical reduction of the growth medium resulting from cellular metabolism. AB is extremely stable and most importantly non-toxic to the cells and thus cultures can be monitored continuously over time. The maximum amount of time it takes for AB to be completely reduced depends on the cell seeding density. Prior to testing the rate of metabolism of cells cultured on the membranes, the desired seeding densities were used to determine the incubation period consistent with linear reduction of AB over 72 hours. In this experiment, the maximum incubation time in which the cells turn AB from the oxidized form to the fully reduced form was 24 hours, with the signal from the first 6 hours being linear.

Figure 4.9 shows the fluorescence over time for astrocytes, BAEC, and Caco-2 cells cultured on the membrane and the control culture dish. According to the slopes, the rate of metabolism of astrocytes was 36% lower on the membrane compared to the control. For BAEC grown on the membrane the rate of metabolism was 19% lower than the control and for the Caco-2 cells the rate was statistically the same on both surfaces. The Trypan Blue test indicated that cell viability is the same on membranes compared to control surfaces for all three cell lines (94%, 96.7%, and 96.9% for astrocytes, BAEC, and Caco-2 cells respectively).

Even though the rate of metabolism of astrocytes and BAEC is lower on PHOST, their viability is the same as those cultured on the control surfaces. The geometry and consequently the thickness of the liquid film above the cells differs in these two constructs (PHOST versus commercial inserts) and the different responses maybe due to differences in surface properties or gas transfer. We believe that Caco-2 cells grow as fast on PHOST compared to control surfaces because they are transformed (i.e. cancer cell line) and thus are robust and properties of the culture substrate may not play a significant role on their metabolism. However, in the case of astrocytes which are primary cells and thus extremely sensitive, the rate of metabolism is lowest. BAEC are also primary cells, but they can be passaged multiple times before they lose their properties and thus they are more robust than astrocytes.

Figure 4.10 shows the phase contrast images of cells 1 day after culture establishment on both surfaces (A-F). This shows the ability of the cells to adhere to porous PHOST with their morphology being indistinguishable from that on the control surface. Phase contrast image of the cells 4 days after culture establishment shows the ability of the cells to grow and proliferate on

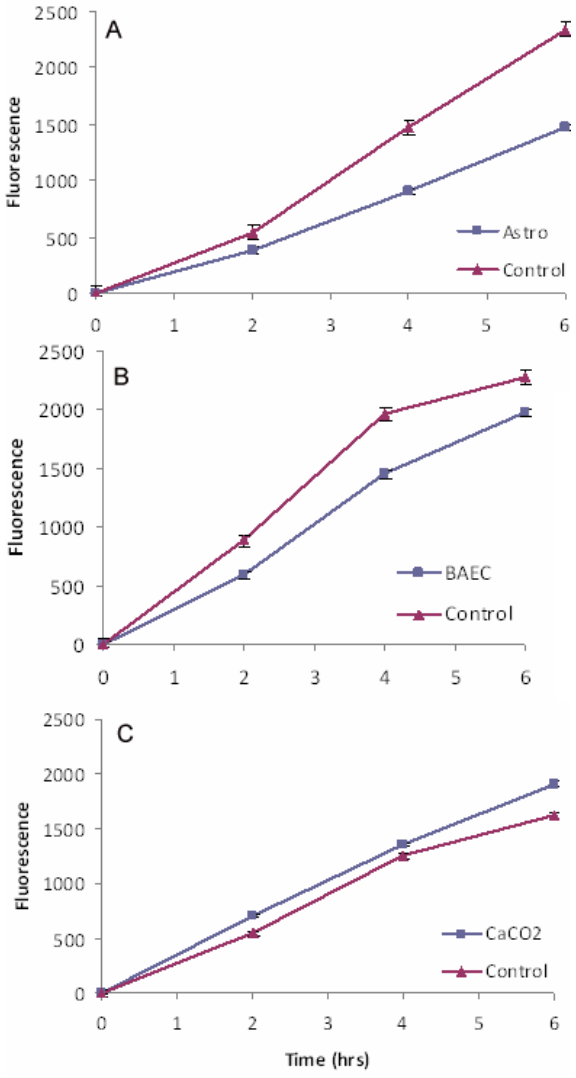

Figure 4.9 | Alamar Blue assay showing cellular rate of metabolism on PHOST with 400 nm pores versus the control surface. (A-C) corresponds to astrocytes, BAEC, and Caco-2 cells respectively. Three independent experiments were performed with *n=4* in each experiment. Statistical analysis of the data was performed by one-way ANOVA ($p < 0.05$). All results are mean ± standard deviation (SD).

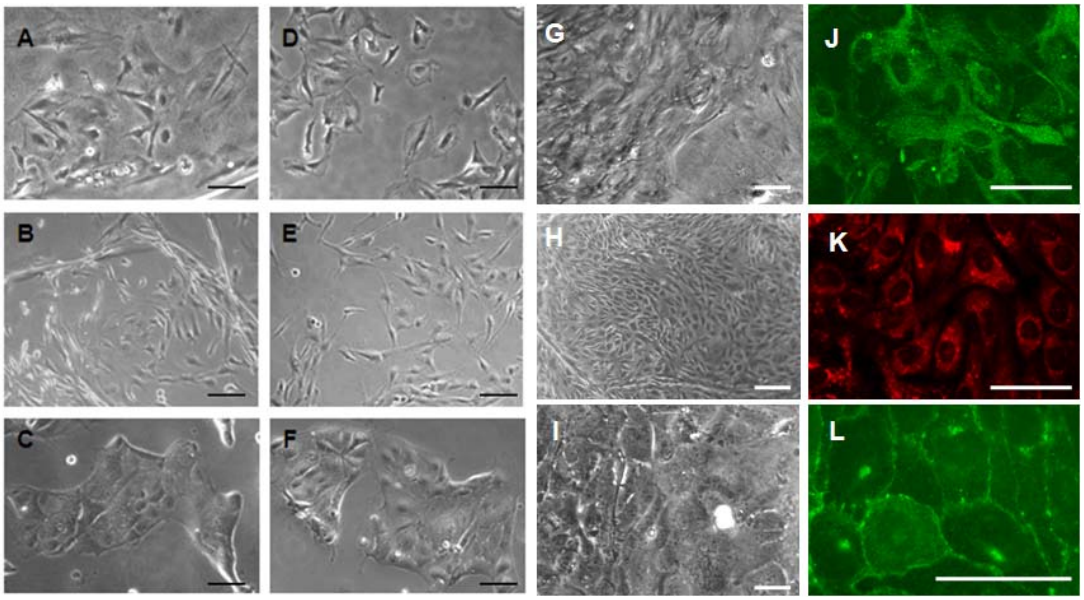

Figure 4.10 | Cell attachment, growth, and differentiation on PHOST. (A-C) shows the attachment of astrocytes, BAEC, and Caco-2 cells on PHOST with 400 nm pores 1 day after culture establishment. The morphology looks indistinguishable from the culture of cells on the commercial permeable supports (D-F). (G-I) shows the proliferation of astrocytes, BAEC, and Caco-2 cells on PHOST with 400 nm pores 4 days after culture establishment. (J-L) shows the expression of GFAP in astrocytes, uptake of Ac-LDL in BAEC, and the expression of occludin in Caco-2 cells all cultured on PHOST with 400 nm pores. Scale bar is 50 μm in all images.

PHOST (Figure 4.10, G-I). Immunocytochemical characterization of BAEC for uptake of Ac-LDL (a marker of endothelial cells), astrocytes for the expression of glial fibrillary acidic protein (GFAP), and Caco-2 cells for the expression of occludin junctional protein shows that the differentiation of these cell types are maintained when cultured on porous PHOST (Figure 4.10, J-L).

4.5.4 Flow Resistance Across Nanofabricated Membranes

As mentioned previously, a key drawback of current commercial permeable supports is their high flow resistance due to a wide pore size distribution with tortuous paths, the low total porosity, and the relatively thick membrane which makes them low-throughput for permeability studies [8-12]. Sodium fluorescein was used to assess the flux across the nanofabricated PHOST and commercially available permeable supports. The rate of transport of sodium fluorescein divided by the porous area is equal to the flux [18]. We evaluated the flux over two nanofabricated PHOST membranes both with 400 nm pore sizes: one with the same total porosity as a commercial counterpart, and the second one with twice the porosity. Figure 4.11 shows the corresponding rates of transport across the membranes. These results indicated that the flux over PHOST is 23 times higher compared to commercial counterparts due to the reduced thickness and the straight pore profiles. When the porosity is doubled, flux is 53 times higher compared to commercial membranes. To our knowledge, this is the first study that establishes a direct comparison between the porosity of commercial membranes versus nanofabricated PHOST and reports a minimum of 23 times higher flux.

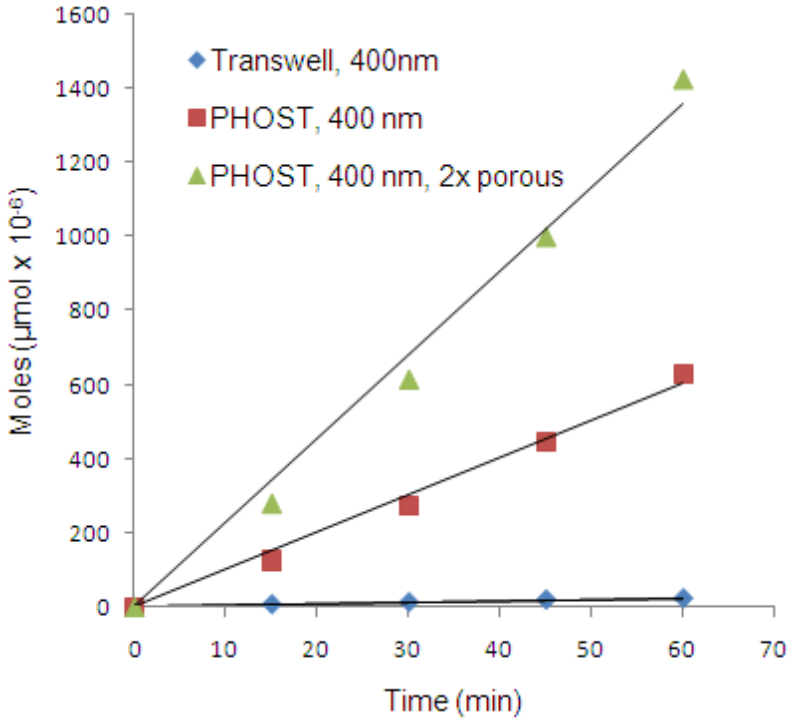

Figure 4.11 | Rate of transport across PHOST with 400 nm pores, its commercial counterpart, and PHOST with twice the porosity of the commercial membrane.

4.6 Conclusion

In summary, 3 μm thick, transparent, porous polymeric membranes based on poly(hydroxy styrene) with defined pore sizes and pore density is nanofabricated. The membrane is attached to a support device to facilitate its use for cell culture and/or permeability studies. Moreover, the membranes have low flow resistance which contributes to their application for high-throughput permeability and/or separation assays. Cell culture studies show the successful attachment, proliferation and differentiation of several cell lines that are commonly used in constructing *in vitro* models of the blood-brain barrier, and intestinal barrier. We believe this is the first study that proposes the suitability of nonporous PHOST as a high-throughput polymeric membrane with lack of cytotoxicity which also has appropriate characteristics for use in nanofabrication processes.

4.7 Acknowledgements

This work was funded in part by the New York State Office for Science, Technology, and Academic Research (NYSTAR) and the National Science Foundation through the Nanobiotechnology Center (NBTC). We specially thank Cornell NanoScale Science and Technology Facility (CNF) for their continuous support on material fabrication as well as Cornell Center for Materials Research for polymer characterization. We thank Professor William Shain at the Center of Neural Communication Technology, Wadsworth Center (Albany, NY) for providing us with Astrocytes. We thank Professor David Putnam at Biomedical Engineering, Cornell University (Ithaca, NY) and Dr. Sara Yazdi for their guidance on ^{1}H-NMR and PHOST synthesis. We also thank Jaewook Seok for his support on chemistry.

REFERENCES

1. Villars, F, Conrad, V, *et al.*, 1996. Ability of various inserts to promote endothelium cell culture for the establishment of co-culture models. *Cell Biol Toxicol*. 12, 207-214.
2. Maric, D, Kaiserlian, D, *et al.*, 1996. Intestinal epithelial cell line induction of T cell differentiation from bone marrow precursors. *Cell Immunol*. 172, 172-179.
3. Shaw, AJ. Epithelial cell culture: A practical approach. Oxford University Press Inc. New York: 2002. p. 12.
4. Sporn, LA, Marder, VJ, *et al.*,1989. Differing polarity of the constitutive and regulated secretary pathways for von-Willebrand factor in endothelial cells. *Journal of Cell Biology* 108, 1283-1290.
5. Harris, S, Shuler, ML, 2003. Growth of endothelial cells on microfabricated silicon nitride membranes for an in vitro model of the blood-brain barrier. *Biotechnology and Bioprocess Engineering* 8, 246-251.
6. Harris, Ma S, Lepak, LA, *et al.*, 2005. An endothelial and astrocyte co-culture model of the blood-brain barrier utilizing an ultra-thin, nanofabricated silicon nitride membrane. *Lab on a chip* 5, 74-85.
7. Demeuse, P, Kerkhofs, A, *et al.*, 2002. Compartmentalized co-culture of rat brain endothelial cells and astrocytes: a syngenic model to study the blood-brain barrier. *J. Neurosci. Meth*. 121, 21-31.
8. Striemer, C, Gaborski, T, McGrath, J, Fauchet, P, 2007. Charge- and size-based separation of macromolecules using ultrathin silicon membranes. *Nature* 445, 749-753.

9. Tong, H, Jansen, H, *et al.*, 2004. Silicon nitride nanosieve membrane. *Nano Letters* 4, 283-287.

10. Van den berg, A, Wessling, M, 2007. Silicon for the perfect membrane. *Nature* 445, 726.

11. Rijn, C, Nijdam, W, Elwenspoek, M, 1995. High flow rate microsieve. *ASME* 57, 995-1000.

12. Kuiper, S, Rijn, C, Nijdam, W, Elwenspoek, M, 1998. Development and applications of very high flux microfiltration membranes. *Journal of Membrane Science* 150, 1-8.

13. Higashimura, T, *et al.*, 1989. Living cationic polymerization of 4-tert-butoxystyrene and synthesis of poly(4-vinylphenol) with narrow molecular weight distribution. *Die Makromolekulare Chemie* 15S, 127-136.

14. Li, M, Douki, K, Goto, K, *et al.*, 2004. Spatially controlled fabrication of nanoporous block copolymers. *Chem. Mater*. 16, 3800-3808.

15. Davis-Cox, M, Turner, JN, *et al.*, 1994. Phorbol ester-stimulated stellation in primary cultures of astrocytes from different brain regions. *Microsc. Res. Tech.* 29, 319-327.

16. O'Brian, J, Wilson, I, *et al.*, 2000. Investigation of the Alamar Blue (resazurin) fluorescent dye for the assessment of mammalian cell cytotoxicity. *Eur. J. Biochem.* 267, 5421-5426.

17. Nasiry, S, Geusens, N, *et al.*, 2007. The use of Alamar Blue assay for quantitative analysis of viability, migration and invasion of choriocarcinoma cells. *Human Reproduction* 1-6.

18. Deli, MA, Abraham, CS, Niwa, M, Falus, A, 2003. N,N-diethyl-2-[4(phenylmethyl)phenoxy]ethanamine increases the permeability of primary mouse cerebral endothelial cell monolayers. *Inflamm. Res*. 52, S39-S40.

19. Winkleman, A, Perez-Castillejos, R, *et al.*, 2007. Patterning micron-sized features in a cross-linked poly(acrylic acid) film by a wet etching process. *Soft Matter* 3, 108-116.

20. Pescini, L, Tilke, A, *et al.*, 1999. Suspending highly doped silicon-on-insulator wires for applications in nanomechanics. *Nanotechnology* 10, 418-420.

21. Wang, H, Laws, GM, *et al.*, 2007. Low temperature ZEP-520A development process for enhanced critical dimension realization in reactive ion etch etched polysilicon. *J. Vac. Sci. Technol*. 25, 102-105.

22. Rooks, MJ, Kratschmer, E, *et al.*, 2002. Low stress development of poly(methylmethacrylate) for high aspect ratio structures. *J. Vac. Sci. Technol.* 20, 2937-2941.

CHAPTER 5

MURINE *IN VITRO* MODEL OF THE BLOOD-BRAIN BARRIER FOR EVALUATING DRUG TRANSPORT

5.1 Preface

This chapter is adapted from: Shayan, G., Choi, Y.S., Shusta, E., Shuler, M. L., Lee, K. H., 2010. Murine *in vitro* model of the blood-brain barrier for evaluating drug transport. *European Journal of Pharmaceutical Science*, in preparation. It describes the functional characterization of an *in vitro* model of the blood-brain barrier composed of murine brain microvascular endothelial cells co-cultured with primary rat astrocytes in the presence of various biochemical inducing agents. These co-cultures are established on commercially available inserts made of polyester with 400 nm pores. This chapter also presents preliminary characterization data from the same co-culture model on commercially available inserts made of polycarbonate, and an in-house nanofabricated poly(hydroxy styrene) membrane.

5.2 Abstract

Current *in vitro* models of the blood-brain barrier (BBB) are composed of brain microvascular endothelial cells (BMEC) that are isolated from rat, bovine, or porcine. However, these models may not be suitable for studies of BBB in brain cancer, neurodegenerative disorders, and inflammatory events involving the CNS because these diseases are generally studied in mouse models and thus murine *in vitro* BBB models serve as better surrogates to correlate with these studies. Here we describe the functional characterization of a

reproducible *in vitro* model composed of murine BMEC co-cultured with primary rat astrocytes in the presence of various biochemical inducing agents on commercially available polyester inserts with 400 nm pores. The co-cultures presented high TEER and low sodium fluorescein permeability. Expression of specific BBB tight junction proteins (occludin, claudin-5, ZO-1) and the functionality of transporters (Pgp, GLUT1) were detected by immunocytochemistry and western analysis. These results indicated a 2.5 fold increase in the expression levels of these proteins in the presence of astrocytes versus BMEC alone. In addition, a high correlation coefficient (0.98) was obtained between the permeability coefficients of a series of hydrophobic and hydrophilic drugs and their corresponding *in vivo* murine BBB transfer coefficients. These results together establish the utility of this murine model for future pathological, physiological, and pharmacological characterizations of the BBB.

5.3 Introduction

The blood-brain barrier (BBB) is comprised of a specialized class of endothelial cells (EC) that line the cerebral vasculature and is an important barrier for protecting the brain from fluctuations in plasma composition [1-2]. By restricting non-specific flux of blood-borne molecules, the BBB plays an important role in maintaining parenchymal homeostasis, and strictly regulates transport of ions, small molecules, proteins, and cells into and out of the brain [3]. The specialized capillary endothelium in the brain is endowed by high electrical resistance tight junctions joining adjacent EC that force most molecular traffic to take a transcellular route across the BBB rather than moving paracellularly through the tight junctions. These EC lack fenestrae and

possess very few endocytotic vesicles, thereby limiting the amount of transcellular flux [3].

In vitro models of the BBB have been developed to better understand the underlying cell biology, to predict drug permeability prior to animal studies, and to overcome the inherent difficulty in performing BBB molecular level studies *in vivo* [4]. These *in vitro* models [5-18] serve as successful surrogates to *in vivo* experiments and provide a critical framework for BBB studies. Recent updates in the construction of *in vitro* models include improved techniques to isolate brain microvascular endothelial cells (BMEC) [8,14,18] induction of BMEC with astrocytes, pericytes, or biochemical agents [5,9,11-14,17].

Structurally, the cell type closest to brain capillary EC is the astrocyte and their processes form endfeet that collectively surround cerebral microvessels [7,9,10,16,19,20]. As a result, several models have focused on recreating the brain microenvironment by incorporating astrocyte co-cultures, or astrocyte conditioned-medium to further induce BMEC. Traditionally, many models involve a contact or often a non-contact co-culture between EC and astrocytes on commercially available microporous filters. Furthermore, rat or bovine BMEC co-cultured with rat astrocytes were shown to have higher transendothelial electrical resistance (TEER) and lower permeability compared to BMEC cultures alone [7,9-11,14,18].

Despite these advances, the majority of current *in vitro* models are based on BMEC that are isolated from rat or bovine. Use of such models may not be suitable for studies of BBB in brain cancer, neurodegenerative disorders, and inflammatory events involving the CNS because these diseases are generally studied in mouse models and thus *in vitro* BBB models using

murine BMEC may be a better basis for comparison [21-22]. The purpose of this study was a detailed characterization of a mouse BMEC model co-cultured with rat astrocytes in contact and without contact on commercially available polyester inserts with 400 nm pores for the first time. Rat astrocytes were chosen in preference to mouse astrocytes due to ease of culture and higher yields. The model was characterized by looking at transendothelial electrical resistance (TEER), sodium fluorescein permeability, qualitative and quantitative expression of tight junction proteins, influx, and efflux transporters. Furthermore, *in vitro* permeability of a group of hydrophilic and hydrophobic drugs were evaluated and correlated with *in vivo* permeability data from mouse and a correlation coefficient of 98% was found.

This study also reports on the preliminary characterization results of the same co-culture model on commercially available polycarbonate inserts (400 nm pores), as well as an in-house nanofabricated poly(hydroxy styrene) (PHOST) membrane (400 nm and 800 nm pores) to evaluate the effects of membranes' physical parameters (material, thickness, and pore size) on the integrity of the BBB model.

5.4 Materials and Methods

5.4.1 Chemicals and Supplies

Poly-D-lysine and L-glutamine were purchased from Fisher Scientific (Pittsburg, PA, USA). Human fibronectin was purchased from Millipore (Billerica, MA, USA). Twenty four well Transwell® permeable support (polyester and polycarbonate; thickness, 10 μm; pore size, 0.4 μm; pore density, $4x10^6$ pores/cm^2 and $1x10^8$,respectively) were purchased from Corning (Lowell, MA, USA). Fetal bovine serum (FBS), Dulbecco's Modified

Eagle Medium (DMEM, with l-glutamin, sodium pyruvate, and low glucose), Ham's F-12 nutrient mixture, TrypLE, and Penicillin-Streptomycin-Amphotercin (PSA) were purchased from Invitrogen (Carlsbad, CA, USA). Dulbecco's phosphate buffered saline (DPBS, without $CaCl_2$ and $MgCl_2$), gentamicin, HEPES sodium salt, fluorescein sodium salt, Heparin, bovine serum albumin, puromycin, hydrocortisone, insulin-transferrin-sodium selenite supplement, retinoic acid, caffeine, prazosin, trazodone, propranolol, hydroxyzine, atenolol, cimetidine, DMSO, Krebs-Ringer buffer, collagen type IV, Triton X-100, and goat serum were purchased from Sigma (St. Louis, MO, USA). 8-CPT-cAMP and RO20-1724 were purchased from Biomol (Plymouth Meeting, PA). Percoll was purchased from Amersham Biosciences (Piscataway, NJ, USA). Type II collagenase and DNase I were purchased from Worthington Biochemical Corp. (Lakewood, NJ, USA). Collagenase-dispase and basic fibroblast growth factor were purchased from Roche Molecular Biochemicals (Indianapolis, IN, USA). Paraformaldehyde (16%) was purchased from Electron Microscopy Sciences (Ft. Washington, PA, USA). Acetylated low density lipoprotein labeled with 1,1'-dioctadecyl-3,3,3',3'-tetramethylindo-carbocyanine percholorate (DiI-Ac-LDL) and bovine platelet-poor plasma-derived serum were purchased from Biomedical Technologies (Stoughton, MA, USA). Polyclonal rabbit anti-glial fibrillary acidic protein (GFAP) antibody (18-0063), rabbit anti-occludin antibody (71-1500), rabbit anti-claudin5 antibody (34-1600), rabbit anti-ZO1 antibody (61-7300), Alexa Fluor® 488 goat anti-rabbit IgG antibody (A11001), and 4',6-diamidino-2-phenylindole (DAPI) dihydrochloride nuclear stain were also purchased from Invitrogen (Carlsbad, CA, USA). Mouse anti-MDR1 (SC-55510) and rabbit anti-Glut1 (SC-7903) were purchased from Santa Cruz Biotechnology (Santa Cruz, CA, USA).

Vectashield mounting medium was purchased from Vector Laboratories (Burlingame, CA, USA). EVOM voltohmmeter (STX2) was purchased from World Precision Instruments (Sarasota, FL, USA). Solvents and reagents for the polymer synthesis were obtained from Sigma (St. Louis, MO, USA) and used without further purification unless otherwise stated.

5.4.2 Polymer Synthesis

The reactions used for the preparation of PHOST is based on a modified reaction scheme [23-24]. Poly(tert-butoxy styrene) was synthesized by free radical polymerization. Briefly, 7.5 mL of 4-*tert*-butoxy styrene (99%) was polymerized in 5 mL of anhydrous toluene at 65ºC with 10 mg of recrystallized *α,α'*-Azoisobutyronitrile (AIBN) as the initiator. All glassware was flame dried prior to use and the reaction mixture was purged with dry argon for 10 minutes. Polymerization was carried out for 19 hours and then terminated in 800 mL of 4ºC methanol. Poly(*tert*-butoxy styrene) was converted to PHOST by a hydrolysis reaction. First, it was dissolved in 20 mL of 1,4-dioxane, and then 50 mL of 4M hydrochloric acid in dioxane solution (5-fold) was added. The mixture was reacted at 80ºC under reflux for 24 hours and then precipitated in 800 mL 4ºC water. After neutralization with NaOH solution to a pH value of 7 – 7.5, the resulting polymer was filtered and lyophilized for 48 hours.

5.4.3 Nanofabrication Process

Briefly, a silicon substrate was cleaned with oxygen plasma (standard recipe) in an Oxford Plasmalab 80+ RIE system for 2 minutes. A solution of poly(acrylic acid) (PAA, 20 wt% in water) was spin-coated at 2000 rpm for 45

seconds on the substrate followed by baking at 130ºC for 5 seconds. The layer thickness was 200 nm by profilometry. Following the deposition of the PAA layer, a solution of PHOST (15 wt% in propylene glycol methyl ether acetate) was spin-coated at 1100 rpm for 30 seconds followed by baking at 130°C for 1 minute. The layer thickness was 3 μm by profilometry (at least four scratches were made on the film at different locations using a razorblade and the depth of each scratch was measured at three different locations). Low stress thermally grown SiO_2 was deposited using the IPE 1000 plasma enhanced chemical vapor deposition system at 115°C for 5 minutes. The layer thickness was 200 – 300 nm. ZEP-520A (positive electron beam resist) was spin-coated at 4000 rpm for 1 minute and baked at 115°C for 2 minutes. Leica VB6-HR electron beam lithography system (100 kV) was used to write a hexagonal pattern of octagons with the current at 1 nA and the exposure dose at 1500 μC/cm^2. The pore diameters were either 400 nm, or 800 nm with 5 μm or 10 μm center to center spacing, respectively (corresponding to $4x10^6$ pores/cm^2 and $1x10^6$ pores/cm^2, respectively). The pattern area was a square with an area of 0.29 cm^2. The exposed samples were developed at 4°C in ZED-N50 for 1 minute, followed by methyl isobutyl ketone (MIBK) for 30 seconds, and finally isopropyl alcohol (IPA) for 1 minute. The SiO_2 mask was etched with a CHF_3/O_2 recipe in an Oxford Plasmalab 80+ RIE system for 6 minutes, and the PHOST was etched with an oxygen plasma clean recipe in an Oxford Plasmalab 100 RIE system for 2 minutes. Finally, the SiO_2 mask was removed with the CHF_3/O_2 recipe for 5 minutes. Pore dimensions were characterized using Zeiss Ultra scanning electron microscope at 3 kV.

The PHOST membrane was detached from the silicon substrate after the fabrication process by placing it in water. This step dissolved the PAA

layer and ensured detachment of the membrane from the substrate. An in-house support device was designed and made from polycarbonate (Figure 5.1). The membrane was chemically attached to the device using methylene chloride. After membrane attachment, the device was placed in a 12-well culture dish and incubated in an antibiotic solution (100 U/mL penicillin, 100 µg/mL streptomycin, and 0.25 µg/mL amphotericin) for 4 hours in culture incubator for sterilization. The membrane was washed with DPBS prior to cell culture.

5.4.4 Isolation of Rat Astrocytes

Astrocytes isolated from 3 days old Wistar rat pups were provided by Dr. W. Shain (Wadsworth Center, Albany, NY) following established techniques [25]. Cells were maintained in DMEM (low glucose, with L-glutamine and sodium pyruvate) supplemented with 5% FBS and gentamicin at the supplier's recommended concentration. Cells were grown on 75 cm^2 tissue culture flasks at passage 0 and were fed every 3 days by completely replacing the medium. Cultures were maintained in a 37°C humidified cell culture incubator with 5% CO_2.

5.4.5 Isolation of Murine Brain Microvascular Endothelial Cells (BMEC)

Isolation of murine BMEC was based on a modified protocol [5,17]. All animals were treated according to protocols evaluated and approved by IACUC at the University of Delaware. In summary, 10 adult wild type male mice (C57Bl/6) were euthanized under CO_2. Forebrains were collected and stored in DMEM on ice. The remainder of the isolation took place under aseptic conditions. The

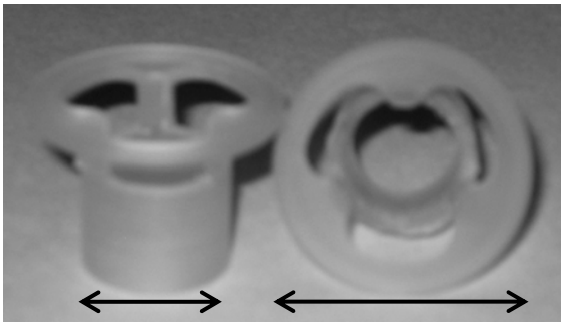

Figure 5.1 | Cell culture support device. After detachment of fabricated membranes from the Silicon wafer, they are chemically attached to the cylindrical segment of the device using methylene chloride. The device fits inside a 12-well culture dish. The arrows represent 1.5 cm and 2.5 cm, respectively.

brains were cut sagittally into two haves and rolled on Whatman 3MM chromatography paper to remove the meninges. The cortices were dissected away and much of the white matter was removed. The cortices were smashed with forceps and completely triturated and digested with 0.69 mg/mL type II collagenase and 37.6 U/mL DNase I in DMEM for 1 hour in 37°C shaker (250 rpm). The enzyme solution was then diluted in DMEM and centrifuged at 1000 *g* for 8 minutes at room temperature. To remove myelin the pellet was resuspended in 20% (w/v) bovine serum albumin in DMEM and centrifuged at 1000 *g* for 20 minutes. The pellet was resuspended and further digested with 0.69 mg/mL collagenase-dispase and 28.3 U/mL DNase I in DMEM for 1 hour in 37°C shaker (200 rpm). The micro-vessels were separated on a 33% continuous Percoll gradient, collected and plated in a 35mm petri-dish coated with collagen type IV and fibronectin. Cultures were maintained in DMEM supplemented with 4 µg/mL puromycin, 20% bovine platelet-poor plasma-derived serum, 1 ng/mL human basic fibroblast growth factor, 1 µg/mL heparin, 2 mM L-glutamine, and an antibiotic solution (100 U/mL penicillin, 100 µg/mL streptomycin, and 0.25 µg/mL amphotericin). Culture medium was completely replaced every day, and puromycin was removed from the medium on day 3. Cells were subcultured on day 3.5 using 1 mL TrypLE and seeded on commercial transwells or nanofabricated PHOST coated with collagen type IV and fibronectin at 300,000 cells/cm^2. Cultures were maintained in Ham's F-12:DMEM (1:1) supplemented with 2 mM L-glutamine, 550 nM hydrocortisone, 312.4 µM cAMP, 17.5 µM phosphodiesterase inhibitor, 1 µM retinoic acid, 5 µg/mL insulin, 5 µg/mL transferrin, 5 ng/mL sodium selenite, and an antibiotic solution (100 U/mL penicillin, 100 µg/mL streptomycin, and

0.25 µg/mL amphotericin). Cultures were maintained in a 37°C humidified cell culture incubator with 5% CO_2.

5.4.6 Co-Culture Setup

Co-cultures were set up on four different membranes: commercial polyester membrane with 400 nm pores, $4x10^6$ pores/cm^2, commercial polycarbonate membrane with 400 nm pores and $1x10^8$ pores/cm^2, 3 µm thick PHOST with 400 nm pores and $4x10^6$ pores/cm^2, and PHOST with 800 nm pores and $1x10^6$ pores/cm^2. The pore densities on PHOST were chosen so that their total porosity (regardless of the pore size) will be the same as commercial polyester membranes.

Two different co-cultures were set up. In the contact co-cultures, astrocytes and BMEC were seeded on the opposite sides of the membranes, while in the non-contact co-cultures astrocytes were seeded on the multi-well dish and BMEC on the membrane. For better astrocyte attachment the backside of the membrane, or the bottom of the multi-well dish, were treated with 5 µg/cm^2 of poly-D-lysine in DMEM without serum for one hour in culture incubator. Before use, poly-D-lysine was aspirated and the surface was rinsed once with DPBS. Astrocytes (passage 1) were seeded at 80,000 cells/cm^2 either on the bottom of the dish (non-contact co-culture) or on the backside of the membrane (contact co-culture). After 20 minutes, all transwells were flipped over inside a 24-well culture dish containing DMEM supplemented with 5% FBS in the bottom compartment and were fed every day for three days before the addition of BMEC. On day three, the astrocyte medium was changed to BMEC medium (Ham's F-12:DMEM (1:1) supplemented with 2 mM L-glutamine, 550 nM hydrocortisone, 312.4 µM cAMP, 17.5 µM

phosphodiesterase inhibitor, 1 μM retinoic acid, 5 μg/mL insulin, 5 μg/mL transferrin, 5 ng/mL sodium selenite, and an antibiotic solution) and BMEC were added to the transwells as described in the previous section.

Controls included empty transwell with the top-side of the membrane coated with collagen type IV and fibronectin and bottom-side coated with poly-D-lysine, murine BMEC and astrocyte only transwells. Culture medium in both compartments was replaced completely every 3 days. All measurements were performed 6 days after BMEC seeding.

5.4.7 Transendothelial Electrical Resistance Measurements

Transendothelial electrical resistance (TEER) was measured using an EVOM voltohmmeter (STX2) 6 days after establishment of co-culture. Final resistance ($\Omega \times cm^2$) was calculated after subtracting the resistance of an empty filter. Three TEER measurements were made per transwell and the arithmetic mean calculated. Unless specified, TEER measurements of three transwells for each culture condition were used to compute the mean and standard deviations reported.

5.4.8 Sodium Fluorescein Permeability Measurements

Prior to permeability studies, culture media from the top and bottom compartments was replaced with pre-equilibrated transport buffer (10 mM HEPES, 0.1% w/v bovine serum albumin, 4.5% w/v glucose). A solution of sodium fluorescein (376 Da) in transport buffer was then added to the upper compartment of the transwell to yield a final concentration of 1 μM. Aliquots (100 μL) were removed from the bottom compartment and the volume replaced with pre-equilibrated transport buffer every 15 minutes over 60

minutes. Based on the rate of influx of sodium fluorescein into the bottom compartment, permeability coefficients were calculated [8].

5.4.9 Uptake of DiI-Ac-LDL

DiI-Ac-LDL was diluted to 10 µg/mL in BMEC medium and added to the upper compartment containing BMEC prior to other immunofluorescent studies. The cells were then incubated in a 37°C humidified cell culture incubator with 5% CO_2 for 4 hours. The cells were rinsed three times with DPBS and then fixed in 4% (w/v) paraformaldehyde at room temperature for 20 minutes.

5.4.10 Immunocytochemistry

All cultures were rinsed twice with DPBS followed by fixation in 4% paraformaldehyde for 20 minutes (all steps performed at room temperature unless stated otherwise). Following three 5 minute rinses in DPBS, astrocytes were permeabilized with 0.1% Triton X-100 in DPBS for 15 minutes, and BMEC were permeabilized with 0.05% Triton X-100 for 5 minutes on ice (BMEC were also pre-permeabilized with 0.2% Triton X-100 for 2 minutes on ice if staining for occludin). After three 5 minute rinses in DPBS following permeabilization, astrocytes and EC were blocked in 10% goat serum in DPBS for 15 and 7 minutes, respectively. All subsequent steps were performed on a shaker. The following concentrations in 10% goat serum were used for primary antibodies: rabbit anti-GFAP 4 µg/mL, rabbit anti-occludin 15 µg/mL, rabbit anti-ZO1 and rabbit anti-claudin5 5 µg/mL. Primary antibodies were added to the appropriate compartment for 1 hour followed by three 10 minutes rinses in 1% goat serum. Cells were incubated for 1 hour in 1:500 dilution of Alexa Fluor® 488 goat anti-rabbit IgG antibody followed by three 10

minutes rinses in 1% goat serum. DAPI was added in 300 nM for 3 minutes prior to mounting the membrane on a glass slide with a cover slip in Vectashield mounting medium. Samples were observed in a Leica SP2 scanning confocal microscope (Leica Microsystems Inc., Bannockburn, IL, USA). Control samples were treated exactly as stated above, except that the primary antibodies were replaced with a rabbit IgG fraction negative control. A secondary antibody-only control was also included.

To assess whether astrocytes clog the 400 nm pores on polyester membranes, samples were fixed in 4% paraformaldahyde at 4°C for approximately 2 weeks. The membranes were labeled red using FM4-64 hydrophobic dye and the cells were labeled green using Syto13 nucleotide dye. The images were taken on a Zeiss AxioObserver Z1 inverted microscope configured as an LSM 5DUO confocal, using a 100x α Plan Apochromat (NA=1.45). The FM4-64 was excited at 560 nm laser (20.9% power) and emitted light was collected using a long pass filter (575). Syto13 was excited with a 488 nm laser (1.9% power) and emitted light was collected using a band pass filter at (505 – 550 nm). Reflected light off the surface of the membranes was visualized with a 633nm laser. Channels were collected in fast line switching mode, and 175 slices were acquired at 0.12 um intervals.

5.4.11 Western Blotting

Six days after establishing the co-cultures, Laemmli sample buffer was used to collect cell lysates. 20 µL of protein lysate was resolved by SDS-PAGE (12% w/v) using Tris-HCl and immunoblotted. All subsequent steps were done at room temperature. Membranes were blocked in 3% non-fat dry milk for one hour and then probed with rabbit anti-occludin (1 µg/mL), rabbit anti-claudin5

(1 µg/mL), rabbit anti-GLUT1 (4 µg/mL), or mouse anti-MDR1 (Pgp) (4 µg/mL). Following washing steps, the membranes were incubated with alkaline phosphatase conjugated goat anti-mouse IgG or mouse anti-rabbit IgG (1:30,000 dilution). Bound antibodies were detected using enhanced chemi-fluorescence (ECF) substrate following the manufacturer's instructions and imaged using a FLA-3000 Fujifilm scanner.

5.4.12 In Vitro Drug Permeability Study

To measure the flux of hydrophobic and hydrophilic drugs selected for the study (Table 5.1) across the co-cultures, inserts were transferred to clean 24-well plates containing 0.6 mL Ringer-Hepes buffer in the lower compartment. All test drugs were dissolved in DMSO to yield a 1 mM solution. The upper compartment was then filled with 0.1 mL of 1 µM drug solution in Ringer-Hepes buffer. The inserts were transferred at 20, 40, and 60 minutes to a new well containing fresh buffer. The concentration of the drugs in the upper and lower compartments were measured by liquid chromatography-mass spectrometry (LC-MS) (described below) and based on the rate of influx of each drug into the bottom compartment, permeability coefficients were calculated and correlated with *in vivo* permeability of the drugs in mice [13].

5.4.13 LC-MS Analysis

To remove insoluble materials and large molecules, samples and standards were filtered through 3 kDa molecular weight cut-off filter (Millipore Micron YM-3) at 10,000 rpm for 25 minutes. 50 µL of each filtrate was separated by an

Table 5.1 | List of drugs selected for transport studies. P_e Values are calculated using a tissue distribution model in mice reported in Nakagawa *et. al* [13]. Permeability values are (10^{-6} cm/s).

Name	MW	CNS	Transport	P_e
Atenolol	226	-	Passive Hydrophilic	2.49
Caffeine	212	+	Passive lipophilic	496.67
Cimetidine	252	-	Efflux: Pgp, BCRP	2.99
Hydroxyzine	448	+	Passive lipophilic	1174.04
Prazosin	420	-	Efflux: Pgp, BCRP	22.91
Propranolol	296	+	Passive lipophilic	1987.16
Trazodone	408	+	Passive lipophilic	333.61

Agilent 1100 series LC system with two mobile phases: a 0.1% formic acid in water, and a 0.1% formic acid in acetonitrile at a flow rate of 400 μL/min. In this system, a two-way divert valve (10 ports, Valco Instruments Co. Inc., Houston, TX), an adjustable splitter (Analytical Scientific Instruments, El Sobrante, CA), a micro-tee connector (Upchurch Scientific, Oak Harbor, WA), and restrictor capillaries (25um ID, Upchurch Scientific) were used for the online desalting of samples and standards. First, with the valve position at "load/wash", samples and standards were introduced on a guard column (C18, 4 x 3.00 mm, Phenomenex, Torrance, CA) by the autosampler and their salts were washed away by 100% formic acid in water for 6 minutes. Then, the valve position was changed to "injection" for the delivery of analytes retained at the guard column to an analytical column (Luna 3μ, C18, 100 x 2.00 mm, Phenomenex) by a gradient mobile phase programming (0% to 80% formic acid in acetonitrile for 30 minutes). At the "load/wash" valve position, the actual flow rate at the guard column was about 250 μL/min and at the "injection" position, the actual flow rate at the analytical column was about 200 μL/min. Analytes eluted from the analytical column were directly introduced into an Applied Biosystems QTRAP mass spectrometer through its Turbospray source (curtain gas of 20.0 psi, high collision gas, ion spray voltage of 5200 V, temperature of 450 °C, ion source gas1 of 20 psi, and ion source gas2 of 40 psi) and analyzed by using full mass scan (mass range between 100 and 1400 *m/z*, scan rate of 4000 amu/s, and dynamic fill time) in the positive ion mode.

5.4.14 Statistical Analysis

The statistical analysis was carried out using JMP® 7.0 (SAS Institute Inc., Cary, NC, USA). Statistical evaluation of the resistance and permeability data

was performed using a least square linear regression model. All results are mean ± standard deviation (SD).

The influence of astrocytes on the resistance and permeability of BMEC in contact and non-contact co-cultures was evaluated using one-way analysis of variance (ANOVA) with linear contrast. The global risk was fixed at $p < 0.05$ for all tests.

5.5 Results

5.5.1 Immunocytochemical Characterization of Murine BMEC and Astrcoytes

BMEC cultured alone or in the presence of astrocytes grew in non-overlapping continuous monolayers and displayed a tightly apposed characteristic spindle shaped morphology (Figure 5.2 A). BMEC cultures in co-culture with astrocytes in contact and without contact retained their phenotype as judged by the uptake of DiI-Ac-LDL (Figure 5.2 B). Astrocytes cultured on the bottom side of the transwell as well as in the multi-well dish, attached and proliferated well and retained their phenotype as judged by GFAP antibody staining (Figure 5.2 C).

5.5.2 Paracellular Permeability of the Co-Cultures

In both co-cultures and controls, paracellular permeability of the endothelial layer was monitored by measuring the TEER and the rate of influx of sodium fluorescein from the top compartment of the transwell to the bottom. Representative influx rates over the transwell membrane area correspond to the permeability coefficient for each configuration.

In the TEER study, regardless of the type of membrane used, the statistical analysis of the data revealed a significant increase in resistance of

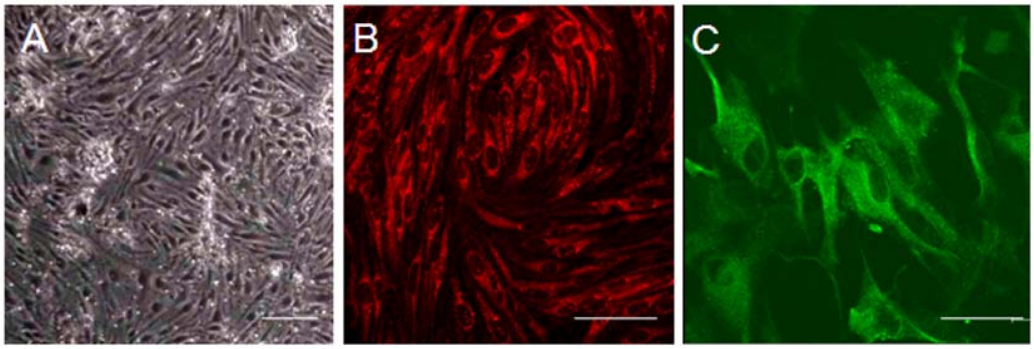

Figure 5.2 | Immunocytochemical characterization of BMEC and Astrocytes. (A) Phase contrast image of BMEC in transwell. **(B)** Immunofluorescent confocal image of BMEC probed for uptake of DiI-Ac-LDL. **(C)** Immunofluorescent confocal image of astrocytes probed for glial fibrillary acidic protein (GFAP). Scale bars represent 50 μm.

BMEC in the non-contact co-cultures (Figure 5.3). The resistance of BMEC alone controls and the contact co-cultures were statistically similar.

The paracellular permeability of BMEC as measured by the influx rate of water soluble small marker sodium fluorescein also revealed similar results to TEER (Table 5.2). The permeability was statistically lowest in non-contact co-cultures compared to BMEC alone, or the sum of BMEC and astrocytes in contact co-cultures.

Permeability and TEER results on PHOST membranes with different pore sizes were statistically similar. However, the overall resistance of BMEC on PHOST and polycarbonate was lower than on commercial polyester membranes with similar pore size and total porosity.

5.5.3 Expression of Transporters and Tight Junction Proteins

BMEC cultured alone and in contact, or non-contact, co-cultures on polyester membranes were examined by immunocytochemistry for the expression and morphological distribution of intercellular tight junction proteins claudin-5, occludin, and ZO-1 (Figure 5.4). While all three proteins are clearly expressed in the different culture conditions, the morphological distribution is smooth in the BMEC alone cultures and turns to a more “zig zag” like configuration in co-cultures. This zig zag configuration is more clear in the morphology of claudin-5 and occludin in the non-contact co-cultures.

To further assess possible changes in the expression level of claudin-5 and occludin in the different culture conditions, western analysis was performed (Figure 5.5). The results indicated that claudin-5 and occludin expression increases 2.5 fold in the non-contact co-cultures. Western analysis was also performed to confirm the expression of P-glycoprotein (Pgp) and

Figure 5.3 | TEER of BMEC and astrocytes on polyester, polycarbonate, and PHOST with 400 nm or 800 nm pores. The TEER of BMEC and contact co-cultures (BMEC/Astro) are statistically similar, while the TEER of the non-contact co-cultures (BMEC-Astro) are statistically higher. BMEC have lower resistance on polycarbonate and PHOST. Results are the means ± SD of 2-3 transwells. Statistical analysis of the data was performed by one-way ANOVA ($p < 0.05$) along with linear contrast analysis for contact co-cultures. Star represents statistical significance. Star represents statistical significance.

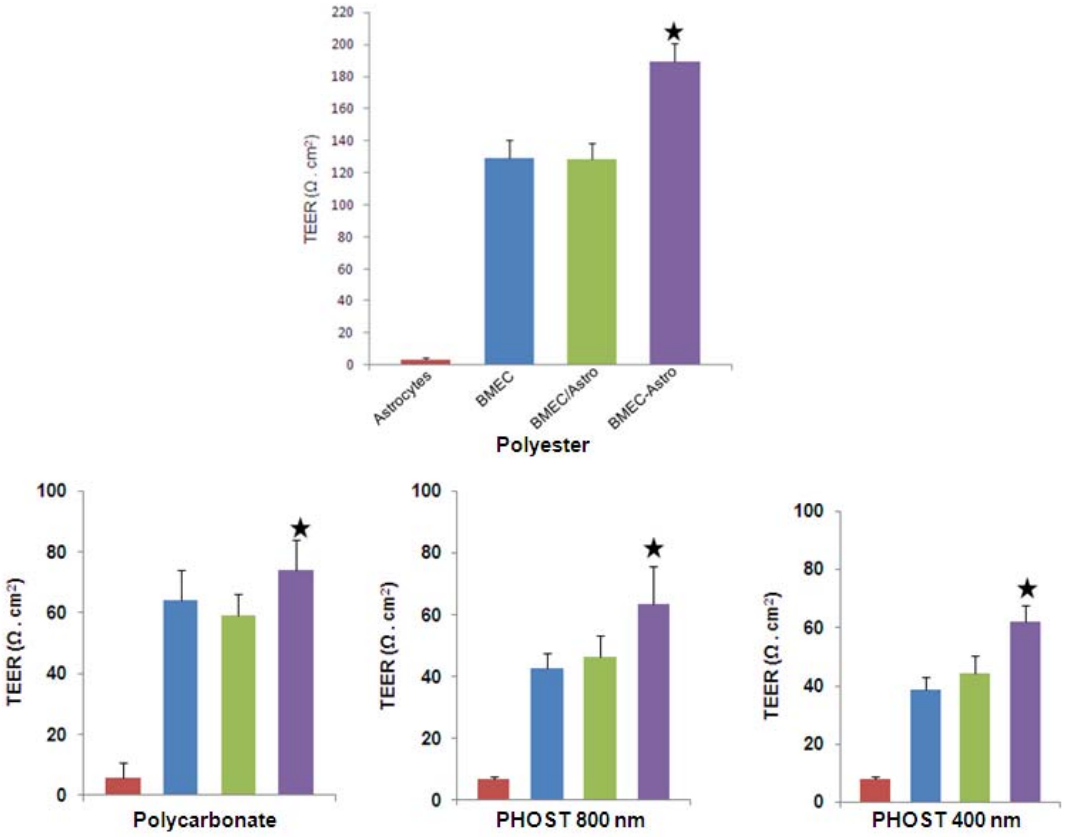
TEER (Ω . cm²)
Astrocytes
BMEC
BMEC/Astro
BMEC-Astro
Polyester
Polycarbonate
PHOST 800 nm
PHOST 400 nm

Table 5.2 | Sodium fluorescein permeability on polyester, polycarbonate, and PHOST with 400 nm or 800 nm pores. Permeability values are (10^{-6} cm/s). Star represents statistical significance.

Culture Type	Polyester	Polycarbonate	PHOST 400 nm	PHOST 800
Astrocyte	25 ± 0.2*	31 ± 0.7*	27 ± 0.4*	23 ± 0.5*
BMEC	6.5 ± 0.8	7.4 ± 0.1	19.4 ± 0.2	17 ± 0.2
Contact	6.1 ± 0.5	7.8 ± 0.4	18.7 ± 0.3	15.8 ± 0.1
Non-contact	3.5 ± 0.1*	6.0 ± 0.1*	13.9 ± 0.3*	11.4 ± 0.5*

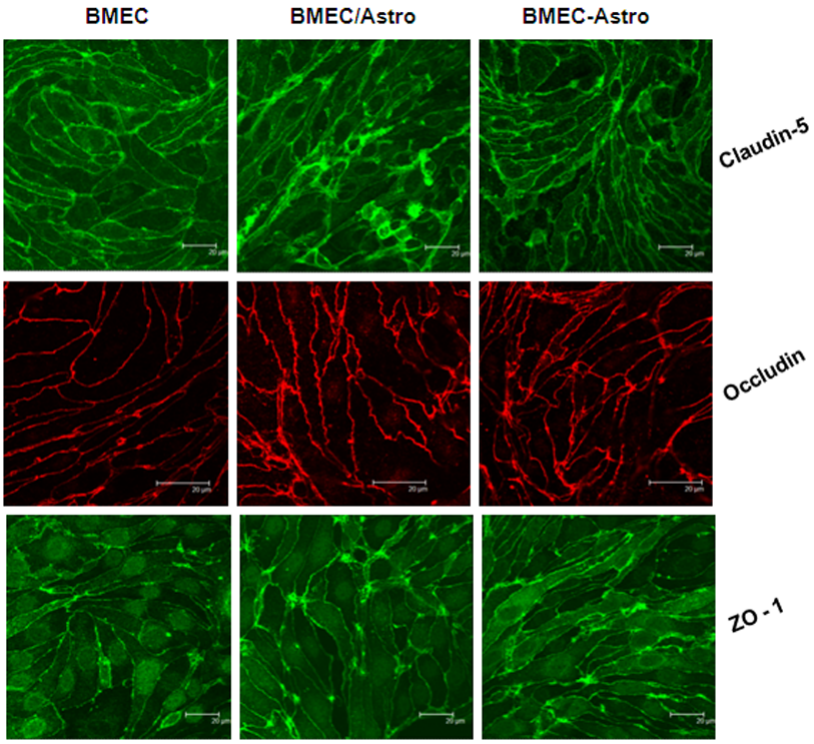

Figure 5.4 | Immunocytochemistry of tight junctions on polyester. Confocal images of BMEC, contact (BMEC/Astro), and non-contact (BMEC-Astro) co-cultures stained for the expression of claudin-5, occludin and ZO-1. The “zig-zag” morphology is more evident in the non-contact co-cultures. Scale bars represent 20 μm.

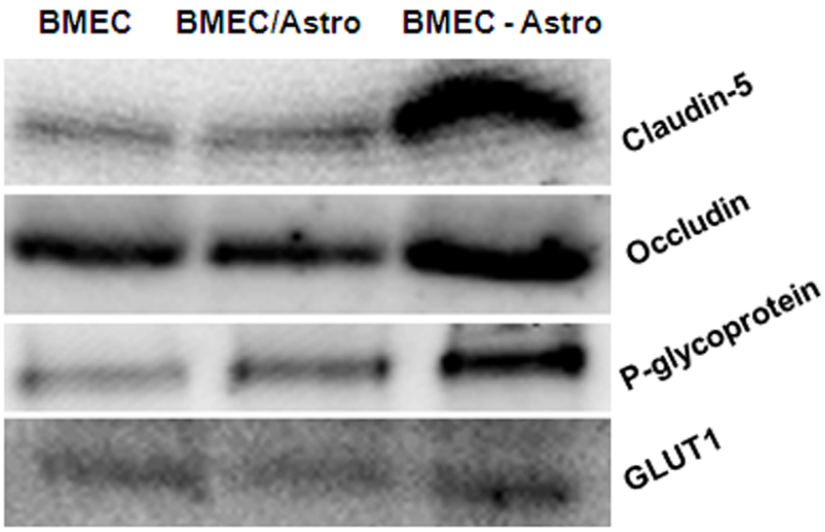

Figure 5.5 | Expression levels of tight junction proteins and transporters on polyester. Western blot results show a 2.5 fold increase in the expression levels of claudin-5, occludin, and P-glycoprotein in the non-contact co-cultures. The results also show the expression of glucose transporter-1.

glucose transporter-1 (GLUT1), and it indicated an increase in the expression of both proteins in the non-contact co-cultures.

5.5.4 Drug Permeability and Correlation with In Vivo Data

The non-contact co-cultures of BMEC and astrocytes on polyester membranes were further characterized by measuring the permeability of compounds with known permeability properties *in vivo* (Table 5.1). These compounds include hydrophobic and hydrophilic drugs. All molecules that enter the BBB by lipid-mediated free diffusion (caffeine, hydroxyzine, propranolol, trazodone) displayed a high permeability when measured on the model (Figure 5.6). In contrast the permeability of small hydrophilic compounds (atenolol, cimetidine, prazosin) was small. When the data obtained from the *in vitro* model was compared with the *in vivo* values, a correlation coefficient of 0.98 was found.

5.6 Discussion

This study has primarily focused on the development of facile and reproducible methods for cultivating mouse BMEC and further co-culturing them with primary rat astrocytes to make an *in vitro* BBB model with more authentic permeability properties. It further included preliminary experiments to assess resistance properties of BMEC on various materials, and whether reduced membrane thickness or increased pore size and porosity facilitates the induction by astrocytes. We believe this is the first study that reports on a complete characterization of an *in vitro* BBB model based on a co-culture of mouse BMEC and rat astrocytes by study of TEER, sodium fluorescein permeability, qualitative and quantitative expression of tight junction proteins, Pgp, and GLUT-1. Further, we correlated permeability of multiple hydrophobic

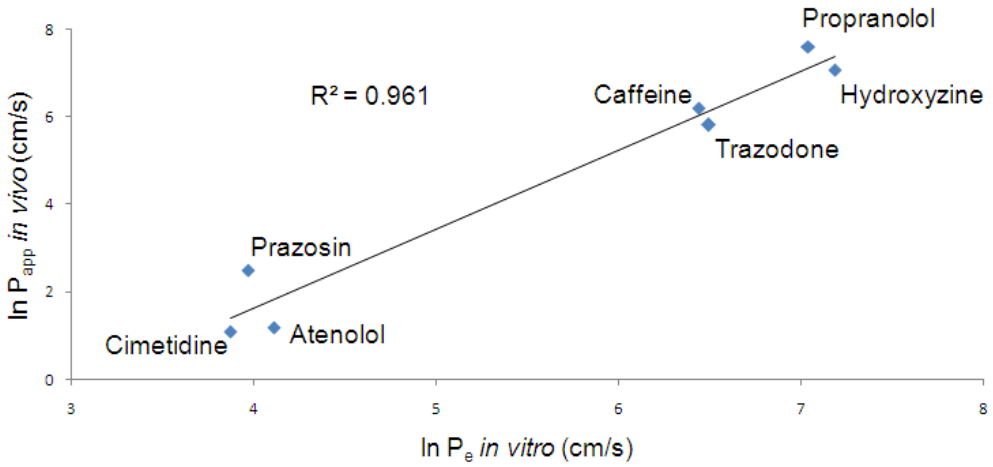

Figure 5.6 | Drug permeability correlation studies. Correlation between permeability coefficients of drugs tested in the *in vitro* model (non-contact co-cultures) and the apparent permeability coefficients measured in mice (Table 5.1). The R^2 value represents the fitness of the straight line, while the actual correlation coefficient is 0.98. Results were replicated in three independent experiments.

and hydrophilic drugs in the *in vitro* model with *in vivo* data from mouse to establish utility of the model for drug development testing by obtaining a 98% correlation coefficient on polyester commercial membranes. Previously characterized *in vitro* models based on BMEC isolated from rat or bovine in co-culture with astrocytes, or in triple co-culture with astrocytes and pericytes have reported drug permeability correlation coefficients ranging from 89% to 94% [4,6,13,15].

Deli *et al.* [8] pioneered the establishment of cultures of primary mouse cerebral EC with reported sodium fluorescein permeability of 1.812 ± 0.191 × 10^{-3} cm/s. Although the reported techniques for isolating mouse BMEC in the current study is motivated by the techniques introduced by Deli *et al.* [8], the use of puromycin to obtain pure cultures of BMEC highlights an important addition to those techniques [5,14,17]. Puromycin is an antibiotic produced by *Streptomyces alboniger* that inhibits peptidyl transfer in ribosomes. However, BMEC can withstand relatively high concentrations of this molecule because of the expression of Pgp, which effluxes puromycin out of the cells. Further, what distinguishes our method from previous reports using mouse BMEC [8,17,26] is the combinatorial addition of biochemical agents (retinoic acid, hydrocortisone, cAMP, phosphodiesterase inhibitor, and insulin-transferrin-sodium selenite) that have been separately shown to induce EC barrier tightening *in vitro* [3,5,10,13,17,27]. Together, the combination of these techniques resulted in a model with improved permeability properties compared to previous studies.

Although the TEER results reported here stand in the lower range compared to some previous models based on porcine, bovine, or rat, the sodium fluorescein permeability of the non-contact co-cultures on polyester

membranes ($3.5 \pm 0.1 \times 10^{-6}$ cm/s) are lower than previous reports [8,10] including triple co-cultures between BMEC, astrocytes, and pericytes [12-13]. Furthermore, the drug permeability results indicate that this model discriminates well between passively and actively transported drugs, and we believe this is the first time that a high syngenic correlation coefficient of 0.98 is achieved. This observation is important because the pharmaceutical industry seeks reliable *in vitro* models for predicting permeability of CNS drugs before moving to *in vivo* testing. Moreover, this model provides the opportunity to correlate *in vivo* and *in vitro* data obtained from the same species (i.e. mouse), while previous reports did such comparisons between different species [6,13,26].

Although this study revealed no significant difference between the properties of BMEC alone and in contact co-culture on neither type of membranes, care must be used before making general conclusions about whether physical contact is necessary in these models. Properties of the transwell membrane, such as thickness, pore size, and pore density play an important role in determining whether sufficient physical contact, and therefore induction, occurs [9,28]. The pore diameter of the commercial membranes in this study (polyester or polycarbonate) was 400 nm, and the observation regarding the lack of BMEC induction in contact co-cultures indicate that this pore size is not large enough to promote complete extension of astrocyte foot processes to the BMEC side, and it appears that this incomplete extension blocks the passage of soluble factors (Figure 5.7). This observation is consistent with a previous report by Demeuse *et al.* [9] that indicated astrocyte foot processes did not cross membranes through pores of 450 nm, and therefore did not induce brain EC. Similar observation was made when 3 μm

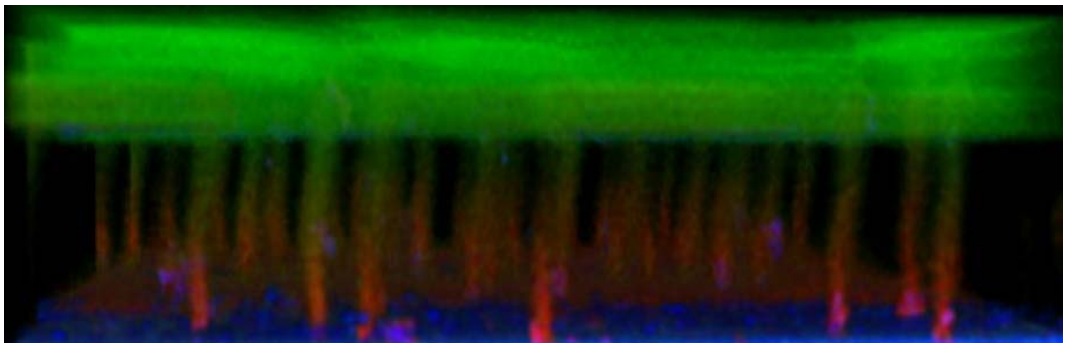

Figure 5.7 | Astrocyte foot processes clog 400 nm pores of polyester membranes. Astrocytes are stained with a cytoplasmic green dye, and as shown the foot processes penetrate halfway inside the pores. A red dye is added to the other side of the membrane with no cells. The blue shows the reflection of the membrane. The width of the image shows the width of the membrane.

thick PHOST with 400 nm and 800 nm pores were used. Even though PHOST is considerably thinner than commercial membranes, it is possible that 3 μm is still too thick to promote physical contact, or 800 nm pores are still too small for this thickness. However, the results on different membranes clearly indicate that the chemistry of the material and possibly porosity play a major role on the physiology of the cultures. It is not clear why the resistance of cells are lower on polycarbonate and PHOST versus a commercial polyester membrane with the same pore size and total porosity. Further characterization is needed to make appropriate conclusions.

The immunocytochemical characterization in this study leads to an interesting observation. The morphology of immunostaining of tight junction proteins clearly changes in the non-contact co-cultures compared to BMEC alone. This morphological change may correlate with increases at the gene expression level, increases at the protein level, or structural changes in the proteins such as phosphorylation. Perriere *et al.* [15] indicated that BMEC co-cultured with astrocytes have higher occludin, claudin-5, and ZO-1 mRNA levels compared to BMEC alone. The Western analysis in this study indicated for the first time that this increase in mRNA levels correspond to an increase in protein expression levels. However, future characterizations at the protein level are needed to investigate possible changes in post-translational modifications of these proteins in the presence of astrocytes.

In vitro BBB models are important research tools to study the structure and function of various BBB components under normal and pathological conditions. Here, we discuss a model based on murine BMEC with improved barrier properties and a high drug permeability correlation coefficient with *in vivo* data. Moreover, this model could serve as a new tool for *in vitro* studies of

BBB in brain cancer, neurodegenerative disorders, and inflammatory events and correlation with mouse models of these diseases.

5.7 Acknowledgements

This work was funded in part by the New York State Office for Science, Technology, and Academic Research and the National Science Foundation through the Nanobiotechnology Center. We thank Professor John Schimenti and Robert Munroe at Cornell University college of veterinary medicine (Ithaca, NY), Professor Ulhas Naik and Meghna Naik at University of Delaware Department of Biological Sciences, Professor William Shain at the Center of Neural Communication Technology, Wadsworth Center (Albany, NY). Special thanks go to Cornell NanoScale Science and Technology Facility, Carol Bayles at Cornell University Life Sciences Core Laboratories Center (CLC), and Professor Kirk Czymmek and Jeffrey Caplan at Delaware Biotechnology Institute Bioimaging.

REFERENCES

1. Abbott,N. J., 2002. Astrocyte-endothelial interactions and blood-brain barrier permeability. *J. Anat*. 200, 629-638.
2. Abbott, N.J., *et al.*, 2006. Astrocyte-endothelial interactions at the blood-brain barrier. *Nat. Rev. Neurosci*. 7, 41-53.
3. Rubin, L. L., Staddon, J. M., 1999. The cell biology of the blood brain barrier. *Annu. Rev. Neurosci.* 22, 11-28.
4. Cecchelli, R., Berezowski, V., Lundquist, S., *et al.*, 2007. Modeling of the blood-brain barrier in drug discovery and development. *Nature Rev. Drug Discovery* 6, 650-661.
5. Calabria, A. R., Weidenfeller, C., Jones, A. R., *et al.*, 2006. Puromycin-purified rat brain microvascular endothelial cell cultures exhibit improved barrier properties in response to glucocorticoid induction. *J. Neurochem*. 97, 922-933.
6. Cecchelli, R., *et al.*, 1999. In vitro model for evaluating drug transport across the blood-brain barrier. *Advanced Drug Delivery* 36, 165-178.
7. Dehouck, M. P., Meresse, S., *et al.*, 1990. An easier, reproducible, and mass-production method to study the blood-brain barrier in vitro. *J. Neurochem.* 54, 1798-1801.
8. Deli, M. A., Abraham, C. S., Niwa, M., Falus, A., 2003. *N,N*-diethyl-2-[4 (phenylmethyl)phenoxy]ethanamine increases the permeability of primary mouse cerebral endothelial cell monolayers. *Inflamm. Res.* 52, S39-S 40.
9. Demeuse, P., Kerkhofs, A., *et al.*, 2002. Compartmentalized coculture of rat brain endothelial cells and astrocytes: a syngenic model to study the blood-brain barrier. *J. Neurosci. Meth*. 121, 21-31.

10. Gaillard, P. J., Voorwinden, L. H., *et al.*, 2001. Establishment and functional characterization of an in vitro model of the blood-brain barrier, comprising a co-culture of brain capillary endothelial cells and astrocytes. *Euro. J. Pharm. Sci*. 12, 215-222.

11. Gaillard, P.J., *et al.*, 2000. Astrocytes increase the functional expression of p-glycoprotein in an in vitro model of the blood-brain barrier. *Pharmaceutical Research* 17, 1198-1205.

12. Nakagawa, S., *et al.*, 2007. Pericytes from brain microvessels strengthen the barrier integrity in primary cultures of rat brain endothelial cells. *Cell Mol. Neurobiol.* 27, 687-694.

13. Nakagawa, S., *et al.*, 2009. A new blood-brain barrier model using primary rat brain endothelial cells, pericytes and astrocytes. *Neurochem. Int*. 54, 253-263.

14. Perriere, N., Demeuse, PH., *et al.*, 2005. Puromycin-based purification of rat brain capillary endothelial cell cultures. Effct on the expression of blood-brain barrier specific properties. *Journal of Neurochemistry* 93, 279-289.

15. Perriere, N., *et al.*, 2007. A functional in vitro model of rat blood-brain barrier for molecular analysis of efflux transporters. *Brain Research* 1150, 1-13.

16. Rubin, L. L., Hall, D. E., *et al.*, 1991. A cell culture model of the blood-brain barrier. *J. Cell Biol.* 115, 1725-1735.

17. Weidenfeller, C., Schrot, S., *et al.*, 2005. Murine brain capillary endothelial cells exhibit improved barrier properties under the influence of hydrocortisone. *Brain Research* 1053, 162-174.

18. Weidenfeller, C., Svendsen, C. N., Shusta, E., 2007. Differentiating embryonic neural progenitor cells induce blood-brain barrier properties. *Journal of Neurochemistry* 101, 555-565.

19. Janzer, R. C., Raff, M. C., 1987. Astrocytes induce blood-brain barrier properties in endothelial cells. *Nature* 325, 253-257.

20. Kacem, K., Lacombe, P., *et al.*, 1998. Structural organization of the perivascular astrocyte endfeet and their relationship with the endothelial glucose transporter. *Glia* 23, 1-10.

21. Nag, S., 2003. The blood-brain barrier: biology and research protocols. Humana Press, New Jersey.

22. Zlokovic, B.V., 2008. The blood-brain barrier in health and chronic neurodegenerative disorders*. Neuron* 57, 178-201.

23. Higashimura, T, *et al.*, 1989. Living cationic polymerization of 4-tert-butoxystyrene and synthesis of poly(4-vinylphenol) with narrow molecular weight distribution. *Die Makromolekulare Chemie* 15S, 127-136.

24. Li, M, Douki, K, Goto, K, *et al.*, 2004. Spatially controlled fabrication of nanoporous block copolymers. *Chem. Mater*. 16, 3800-3808.

25. Davis-Cox, M. I., Turner, J. N., *et al.*, 1994. Phorbol ester-stimulated stellation in primary cultures of astrocytes from different brain regions. *Microsc. Res. Tech.* 29, 319-327.

26. Cosine, C., *et al.*, 2005. Mouse syngenic in vitro blood-brain barrier model: a new tool to examine inflammatory events in cerebral endothelium. *Laboratory Investigation* 85, 734-746.

27. Hoheisel, D., Nitz, T., *et al.*, 1998. Hydrocortisone reinforces the blood-brain barrier properties in a serum free cell culture system. *Biochem. Biophys. Res. Commun.* 247, 312-315.

28. Harris Ma, S., Lepak, L. A, *et al.*, 2005. An endothelial and astrocyte co-culture model of the blood-brain barrier utilizing an ultra-thin, nanofabricated silicon nitride membrane. *Lab on a chip 5*, 74-85.

CHAPTER 6

INTRAVENOUS IMMUNOGLOBULIN IMMUNOTHERAPY IN AUTOIMMUNE AND NEUROLOGIC DISEASES

6.1 Introduction

Intravenous immunoglobulin (IVIg) is produced from human plasma derived from thousands of healthy donors using a modified Cohn-Oncley cold ethanol fractionation process, as well as cation and anion exchange chromatography. IVIg contains the entire range of natural antibodies present in normal plasma and has been used in the treatment of primary and secondary antibody deficiencies for over 50 years [1]. IVIg was first demonstrated to be effective in treating an autoimmune disorder, idiopathic thrombosytopenic purpura, in 1981 [2,3,4]. Since then, IVIg has been established to be effective in the treatment of the Guillain-Barre syndrome, chronic inflammatory demyelinating polyneuropathy, myasthenia gravis, corticosteroid-resistant dermatomyositis, Kawasaki's syndrome, and in the prevention of graft-versus-host disease in recipients of allogenic bone marrow transplants [5]. Benefits of IVIg have also been reported in many other autoimmune and systemic inflammatory conditions [6].

The success of IVIg immunotherapy in the treatment of autoimmune diseases has promoted its use for the treatment of neurologic disorders, including Alzheimer's disease [5-9]. In contrast to many autoimmune disorders where the affected cells are virtually bathed in high concentrations of infused IgG, the access of IVIg to the central nervous system (CNS) is severely restricted by the blood-brain barrier (BBB) [10]. However, several studies have

indicated that cerebrospinal fluid (CSF) IgG concentration increases two-fold following a high-dose infusion of IVIg, corresponding to a five-fold IgG increase in the serum [5]. What remains unclear is whether IVIg molecules interact directly with the proteins in the CSF. This review looks at the components of IVIg along with its known mechanisms of action in the treatment of autoimmune diseases. It further reviews preliminary proteomics approaches to identify possible interactions between IVIg and CSF.

6.2 Components of IVIg

Commercial preparations of IVIg contain intact IgG molecules with a distribution of IgG subclasses corresponding to that in normal human serum. Most preparations contain traces of IgA and IgM. IVIg also contains trace amounts of soluble CD4, CD8, and HLA (human leukocyte antigen) molecules and certain cytokines [11-12]. The half-life of infused IVIg in an immune-competent person is three weeks.

Because IVIg consists of polyclonal IgG, both polyreactive natural antibodies as well as antibodies with specificities for allotypic antigens are present in it. These sources of IgGs have been suggested to contribute to IVIg's efficacy through neutralization of various inflammatory components, including pathogenic antibodies [13-14]. However, most experiments have shown that the active component of IVIg lies within the Fc domain-containing fractions rather than the $F(ab)_2$ fractions, implicating Fc receptor engagement rather than neutralization mechanisms.

Natural antibodies are more polyreactive than immune antibodies because they can often bind to different antigens [15]. Natural antibodies can also recognize and be recognized by other autoantibodies in the same person.

The high level of natural antibodies in IVIg, makes a considerable fraction of it capable of interacting with idiotypes to form dimers or multimers. The content of such dimers increases with the number of donors in the pool [16]. The formation of idiotype-idiotype dimers may account for some of the clinical effects of IVIg.

6.3 Mechanisms of Action of IVIg

6.3.1 Fc Receptor Mediated Effects

Fc receptors (FcR) bind the Fc region of the immunoglobulins. Fcγ receptors (FcγR) bind the Fc region of only the γ subclass. The main mechanism of action of IVIg in autoantibody-mediated cytopenias is FcγR blockade on macrophages [17-18], which leads to the deactivation of phagocytes and lymphocytes. In inflammatory neurological disorders IVIg has an anti-demyelination effect, resulting from FcR blockade. IVIg is believed to prevent the phagocytosis of antigen bearing target cells.

IVIg has been found to affect antibody kinetics through the neonatal Fc receptor (FcRn) blockade. FcRn is a protective transport receptor that prevents the catabolism of IgG molecules. Generally, IgG molecules that enter the cell bind maximally to FcRn, which protects them from lysosomal degradation [19]. When IVIg blocks FcRn receptors, IgG catabolism is increased and the concentration of pathogenic autoantibodies are decreased.

6.3.2 Anti-Idiotypic Effects

IVIg has been found to contain anti-idiotypic antibodies against autoantibodies (i.e. idiotypes). Examples of such autoantibodies include anti-DNA, anti-phospholipids, and anti-acetylcholine receptor. Anti-idiotypic antibodies in IVIg

bind and neutralize the autoantibodies and moreover have the ability to modulate the immune system by suppressing antibody production [5]. However, IVIg does not contain anti-idiotypic antibodies against rare auto-antibodies.

6.3.3 Effects on Complement Proteins

The complement system is a complex cascade, which ultimately results in an inflammatory response. One of the potent anti-inflammatory effects of IVIg lies within the ability of the Fc region of the IgGs to interact with complement proteins in the plasma [1]. The anti-inflammatory effects of IVIg have been demonstrated is several autoimmune diseases, including dermatomyositis and Kawasaki syndrome. In an *in vitro* study, sera of dermatomyositis patients were treated with IVIg and as a consequence a significant decrease in C3 uptake was observed [20]. This observation is consistent with the idea that IVIg withholds complement-mediated tissue damage by preventing the deposition of complement proteins on target surfaces.

6.3.4 Effects on the Cytokine Network

One of the most significant disease-modifying mechanisms of IVIg is the regulation of the immune system by altering cytokine levels. IVIg has been found to reduce the inflammatory response via natural antibodies against specific cytokines, cytokine antagonists, and cytokine receptors [21]. Natural antibodies against proinflammatory cytokines, interleukin (IL)-1, tumor necrosis factor (TNF)-α, and IL-6 are examples of such antibodies. IVIg contains cytokines, which may represent the cytokines existing in normal human plasma [21]. Therefore, IVIg's cytokine rebalancing ability is of great

importance in conditions associated with cytokine deregulation, such as autoimmune diseases, cancer, and inflammation. IVIg also exerts its anti-inflammatory effects by regulating the production, release, and function of proinflammatory cytokines. IVIg was found to downregulate the production of proinflammatory cytokines *in vitro* in mitogen-stimulated peripheral blood mono-nuclear cell (PBMC) cultures. These proinflammatory cytokines include IL-2, IL-3, IL-4, and IL-5.

6.4 Protein Targets of IVIg in the Cerebrospinal Fluid

Experimental evidence of the possible interactions between IVIg and CSF, as well as the underlying mechanisms of interaction is non-existent. The subsequent section in this chapter provides examples of possible proteomics approaches that may be utilized to identify some of these interactions, highlighting the experimental results as well as how they fit within the context of known disease-modifying effects of IVIg.

6.4.1 Immunoprecipitation with Magnetic Beads

Immunoprecipitation (IP) is a technique by which a target protein or antigen is precipitated from a solution using an antibody specific for that target. IP with magnetic beads (i.e. Dynabeads®) can be utilized to identify possible proteins in CSF that interact with IVIg, as shown in Figure 6.1. Briefly, IVIg is immobilized on Dynabeads® and then CSF is flowed through it. After elution, samples are resolved by SDS-PAGE.

The main source of complication in this analysis is the presence of antibodies in the CSF. The endogenous CSF antibodies may bind free beads (i.e. beads that have not bound IVIg) and thus a CSF only control is needed to

Figure 6.1 | Immunoprecipitation of CSF with Dynabeads® coupled with IVIg. IVIg was immobilized on two different Dynabeads: Protein G (top) and Protein A (bottom). Both Dynabeads have strong affinity for IgG, but Protein A has a better affinity for IgA and IgM compared to Protein G. First three lanes from left on both gels correspond to the protein ladder and raw samples of IVIg and CSF. Lanes 1-3 correspond to beads+IVIg+CSF, beads+CSF (control), and beads+IVIg (control) respectively. Lanes 1S-3S correspond to the flow-through of samples 1-3 respectively to monitor the efficiency of binding. A protein band that appears in lane 1, but not in lanes 2 and 3 would be of interest.

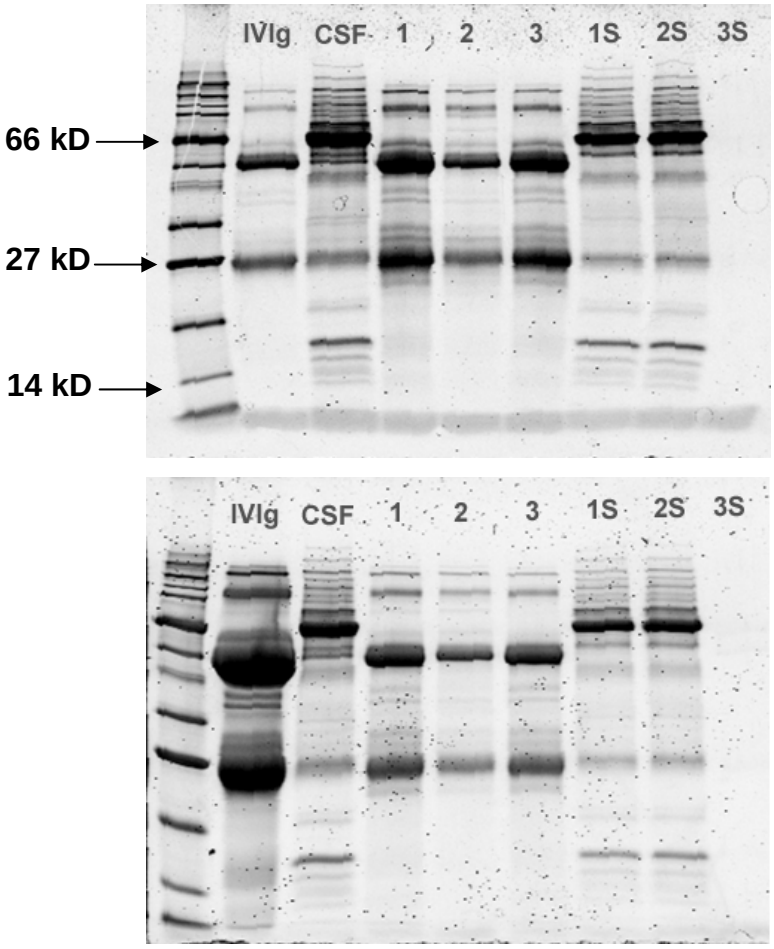
IVIg
CSF
1
2
3
1S
2S
3S
66 kD
27 kD
14 kD
IVIg
CSF
1
2
3
1S
2S
3S

analyze the results properly. Also, because the elution will contain molecules present in the IVIg, an IVIg only control is needed to subtract these molecules from the final co-immunoprecipitant. Figure 6.1 exemplifies these controls. As shown in the figure, protein bands corresponding to elution of IVIg plus CSF look similar to IVIg alone, and CSF alone controls, which makes it difficult to identify possible interacting partners or complexes. Using two-dimensional gel electrophoresis (2DE) to resolve the IP elution may serve as a more sensitive technique to analyze such complex mixtures.

6.4.2 One-Dimensional Gel Electrophoresis and Western Blot

As an alternative approach to IP, CSF can be resolved by one-dimensional SDS-PAGE and immunoblotted against IVIg. Membranes are probed with IVIg as a primary antibody followed by alkaline phosphatase labeled anti-human IgG, IgM, or IgA as a secondary antibody. Bound antibodies are then detected using an enhanced chemi-flourescence substrate. Figure 6.2 shows an example of such blots probed with anti-human IgG (panel A), IgM (panel B), and IgA (panel C).

Based on the results from the secondary antibody only control blots, it appears that CSF proteins themselves interact directly with the secondary antibodies. Therefore, it is difficult to deduce whether the protein bands on blots probed with IVIg are a results of interaction between IVIg and the secondary antibody, or CSF and the secondary antibody. Only two bands, one around 14 kD in panel A, and the other one around 66 kD in panel B may be indicative of possible interactive partners between IVIg and CSF because none appear on the secondary antibody only control blot. These bands can be further cut out of the gel and analyzed using mass spectrometry, however,

Figure 6.2 | Reactivity of IVIg with CSF using one-dimensional western blot. CSF was resolved by 1D SDS-PAGE and immunoblotted. Membranes were probed with three different dilutions of IVIg (1:1k, 1:2k, 1:3k) as the primary antibody followed by anti-human IgG (A), IgM (B), and IgA (C) as the secondary antibody. For each panel, the secondary antibody control blot is located on the right hand side. In panels A and B, only one band (arrow) appears on the IVIg plus secondary antibody, but not on the secondary antibody control blot. These bands may correspond to proteins in the CSF that bind IgGs or IgMs in IVIg.

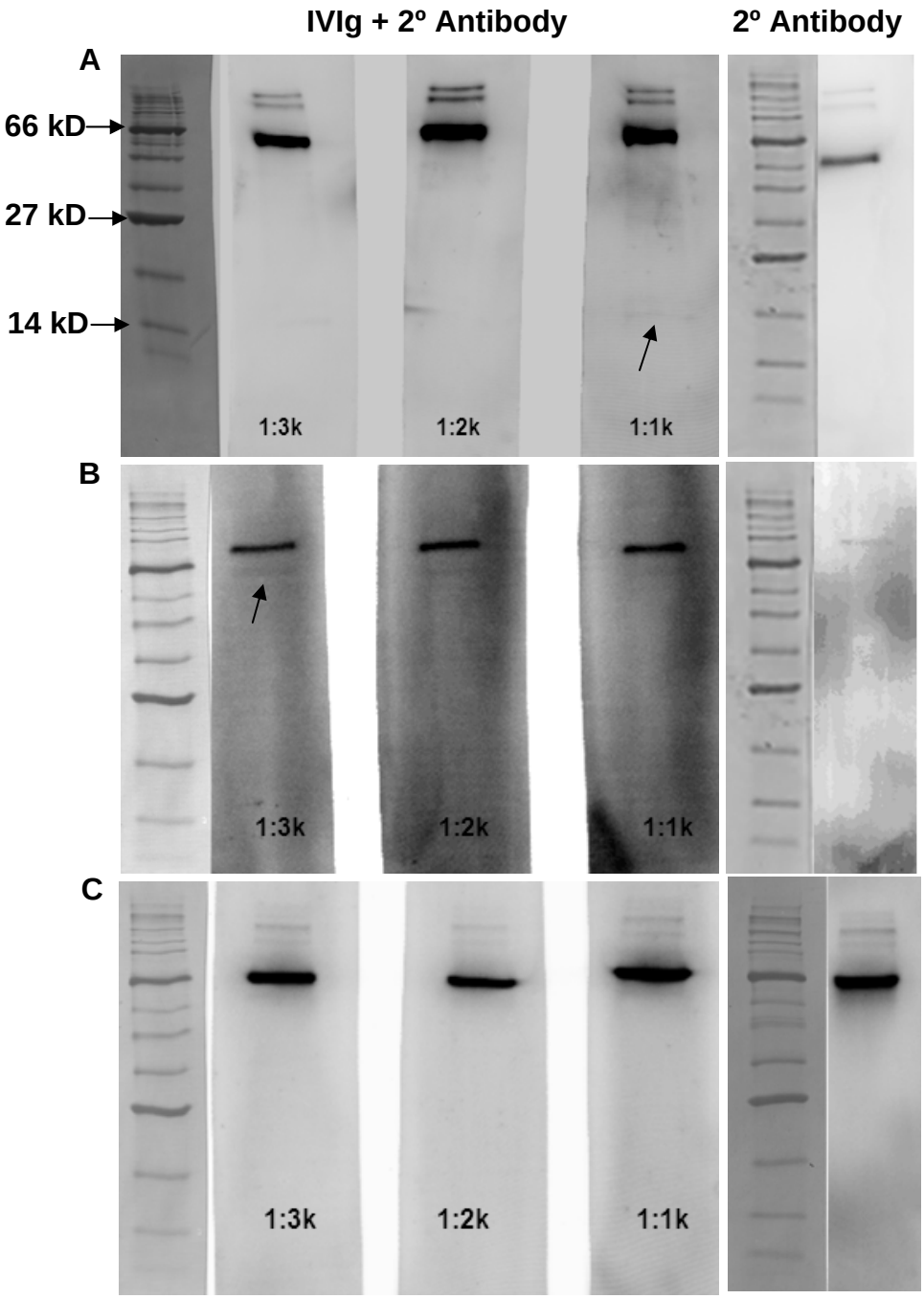
IVIg + 2º Antibody
2º Antibody
A
66 kD
27 kD
14 kD
1:3k
1:2k
1:1k
B
1:3k
1:2k
1:1k
C
1:3k
1:2k
1:1k

because 1D gels are not capable of resolving a high protein content sample, 2DE may again serve as a better technology for this analysis.

6.*4.3 Two-Dimensional Gel Electrophoresis and Western Blot*

2DE permits high resolution separation of individual proteins from complex mixtures in two orthogonal dimensions. The sequential use of both separations significantly expands the resolving power of 2DE over 1D gels, with a potential to resolve as many as 2000-5000 proteins within one sample. Comprehensive 2DE protein maps have been published for several samples related to neurological disorders, including human CSF, Plasma, and brain [22-23].

Similar to the techniques introduced in the previous section, CSF can be resolved by 2DE and immunoblotted. Membranes are then probed with IVIg followed by anti-human IgG, IgM, or IgA. Bound secondary antibodies are then detected using an enhanced chemi-flourescence substrate and imaged. The blots are then stained using a total protein stain to enable spot identification. Figure 6.3 shows an example of such blots. Panel A in this image shows a clear example of anti-human IgGs binding to the endogenous immunoglobluins (or possibly other proteins) in the CSF, in the secondary control blot. However, these interactions seem to be blocked when IVIg is used as the primary antibody. In other words, bound IVIg prevents the binding of the secondary antibody. Similar effects are not observed when IgM or IgA is used as the secondary antibody. While these results are preliminary, they can provide hints on the possible interactions between the CSF and IVIg. The following section provides an overview of how these results fit within the context of the immunology network theory, and of possible disease-modifying effects of IVIg in neurologic disorders.

Figure 6.3 | Reactivity of IVIg with CSF using two-dimensional western blot. CSF was resolved by 2-D gel electrophoresis and immunoblotted. Membranes were probed with 1:1k dilution of IVIg as the primary antibody followed by anti-human IgG (A), IgM (B), and IgA (C) as the secondary antibody. Panel (A) also shows the image of a stained 2-D CSF gel on the far right for spot identification. Panel (A) shows that anti-human IgG is unable to bind endogenous immunoglobulins in the CSF in the presence of IVIg. Similar effect is not observed in the other panels.

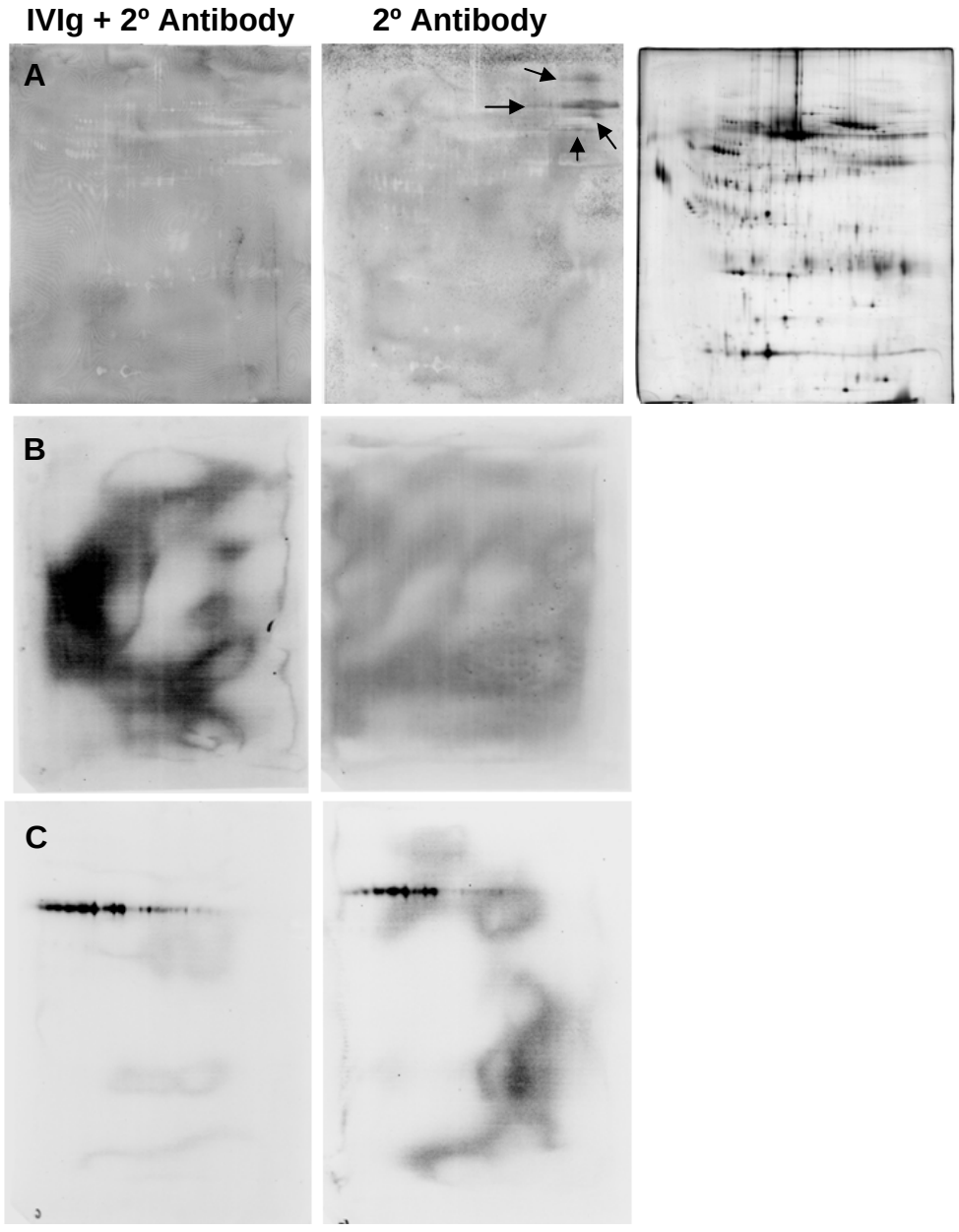
IVIg + 2º Antibody
2º Antibody
A
B
C

6.5 Idiotypic Network Theory in Autoimmunity

In 1974, Jerne [24] proposed that the immune response might be regulated via the unique antigenic determinants of Ig variable regions (i.e. idiotypes). This hypothesis predicts that the idiotypic determinants of each antibody molecule would be complemented by those of another, creating an idiotypic network through which Ig expression might be controlled. A wide array of experiments, including immunization with anti-idiotype antibodies as a vaccine against cancer [25], have strengthened Jerne's hypothesis.

The dogma of idiotypic network theory is that an antigen generates antibodies whose serologically unique structure (i.e. idiotype) results in the production of anti-idiotypic antibodies. The original antibody is designated Ab_1, and the anti-idiotypic antibody Ab_2. The Ab_2 antibodies recognize the antigen-binding site of Ab_1, and therefore share a structural similarity with the original antigen. The cascade then repeats with the generation of anti-anti-idiotypic antibodies (Ab_3) that recognizes Ab_2 and so on (Figure 6.4) [24,26-29]. The end result is the production of a chain of autoantibodies that recognize each other and may modulate the immune system by stimulating or suppressing it. However, it is not exactly clear how far this cascade continues and what triggers the body to prefer one pathway over another. This network theory has been harnessed for preventive immunization as well as for therapeutic purposes and it was proposed that the idiotypic network may be involved in the pathogenesis of autoimmune diseases [28].

In human autoimmune diseases, remission or recovery may be associated with the presence of anti-idiotypic antibodies directed against the patient's autoantibodies in the plasma. Anti-idiotypic antibodies against autoantibodies have been found in patients with Systemic Lupus

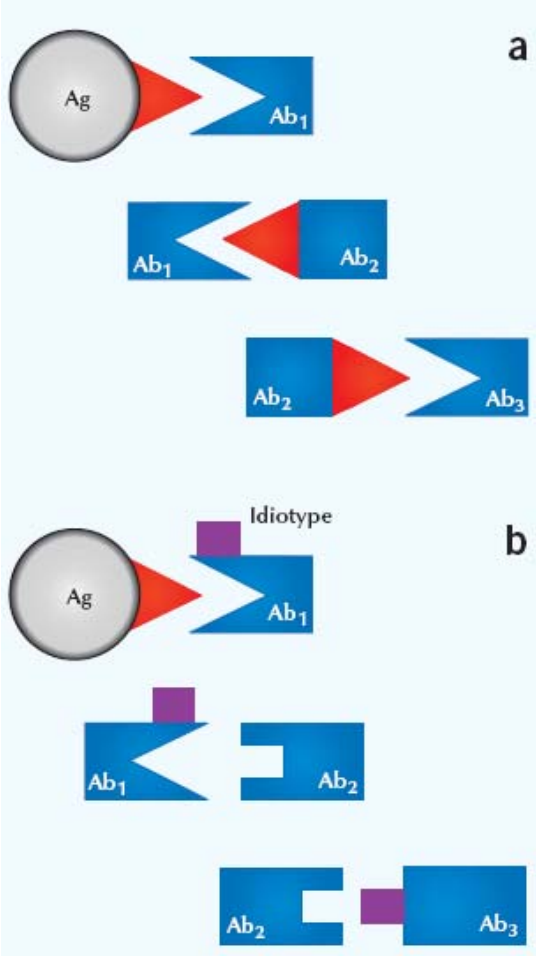

Figure 6.4 | Network of antibodies. (a) According to Jerne's theory [24], immunization with an antigen may lead to the generation of not only Ab_1, but also the anti-idiotypic antibodies. **(b)** A unique structure (idiotype) in the framework of Ab_1 can trigger the idiotypic network. This figure is reprinted by permission from Macmillan Publishers Ltd: [Nature Medicine] (26), © (2004).

Erythematosus (SLE) [30-31], myasthenia gravis [32], autoimmune thyroiditis [33], and polyneuropathy associated with gammopathy [34]. Intravenous infusion of IgG prepared from large pools of normal donors has resulted in clinical improvements and decrease in autoantibody titer in several organ-specific autoimmune diseases [35-37]. In this context, it is believed that IVIg interferes with the binding of autoantibodies to their respective antigens.

As mentioned previously, treatment of neurologic disorders with IVIg has indicated that CSF IgG concentration increases two-fold corresponding to a five-fold increase in the serum [5]. This increase is reversed when IVIg treatment is stopped. Experimental evidence of whether this increased concentration of antibody (i.e. anti-idiotypes) interferes with binding of autoantibodies, or antibodies that initiate inflammatory, or complement cascades in the CSF is non-existant, but experimental techniques outlined in the previous section may be useful in addressing this issue. For example, the 2D western analyses outlined above, provide evidence that IVIg can bind endogenous CSF antibodies or proteins in such a way that these molecules are no longer available to bind anti-human IgGs. While it is still unclear how this blockage contributes to the disease-modifying effects of IVIg in neurologic disorders, the phenomenon itself fits well within the context of the anti-idiotype network theory and known anti-idiotypic effects of IVIg.

According to a previously established 2DE CSF map [38], the majority of the proteins that appear in the region highlighted by arrows in Figure 6.3 are immunoglobulins. A preliminary hypothesis based on the 2D westerns is that the binding of IVIg to endogenous CSF immunolgobulins and possibly their neutralization alleviates pathologic symptoms. The disease-modifying effects may be a primary result of this neutralization, or there may be other cascades

that are affected by this neutralization (i.e. complement and inflammatory cascades) that further result in disease modification. However, other proteins such as plasminogen, gelsolin, and complement component 3 (C3) also appear in the same region. Both plasminogen and C3 have been previously implicated as a diagnostic biomarker of AD [39]. Moreover, the concentration of C3 decreases in Alzheimer's patients after six months of IVIg immunotherapy [Chapter 8]. Thus, depending on what panel of proteins or antibodies in the CSF are involved in interacting with IVIg, a more detailed disease-modifying mechanism can be established.

6.6 Conclusion

The success of intravenous immunoglobulin therapy in the treatment of autoimmune diseases has promoted its use for the treatment of neurological disorders, including Alzheimer's disease. Although the access of IVIg to the central nervous system is restricted by the blood-brain barrier, experimental evidence suggests entry of IgG into the cerebrospinal fluid. However, what remains unclear is how the immunoglobulins interact with other proteins in the CSF (if any) and whether this interaction is responsible for disease-modifying effects. This chapter provided a review on components of IVIg, its known mechanisms of action with respect to autoimmune diseases, as well as possible proteomics approaches that may be utilized to identify the protein targets of IVIg in CSF. In particular, 2DE coupled with western analysis seems to be a promising approach to understand these mechanisms.

6.7 Supplemental Methods

6.7.1 Immunoprecipitation with Dynabeads®

Immunoprecipitation kit-Dynabeads® Protein A and G were purchased from Invitrogen (Carlsbad, CA, USA) and samples were prepared following the manufacturer's protocol. Briefly, 6 mg of dynabeads was incubated with 10% Gammagard liquid (corresponding to 40 µg of protein in IVIg) (Baxter Healthcare Corporation, Westlake Village, CA, USA) on a vortex for 10 minutes at room temperature. After collection of the flow-through and a single washing step, 233 µg of protein in CSF was added to the IVIg-bound dynabeads on vortex for 60 minutes at room temperature. After collecting the flow-through, CSF bound to IVIg was washed three times and eluted from the beads and mixed with Laemmli sample buffer. 15 µL of protein sample was resolved by SDS-PAGE (12% w/v) using Tris-HCl. The separated proteins were stained with SYPRO Ruby Protein Gel Stain (Molecular Probes), and de-stained for 24 hours in a solution of 10% methanol and 7% acetic acid. The gel was scanned on a FLA-3000 Fluorescent Image Analyzer (Fujifilm Company).

Control samples consisted of 2 µg of protein in 10% Gammagard, 7 µg of protein in CSF, 40 µg of protein in 10% Gammagard bound to dynabeads, and 233 µg of protein in CSF bound to dynabeads.

6.7.2 One-Dimensional Western Blot

Laemmli sample buffer was mixed with 7 µg of CSF and 15 µL of samples was resolved by SDS-PAGE (12% w/v) using Tris-HCl and immunoblotted. All subsequent steps were done at room temperature. Membranes were blocked in 3% non-fat dry milk for one hour and then probed with 10% as is or dialyzed Gammagard at 100 µg/mL, 50 µg/mL, or 33.3 µg/mL for one hour. Following

washing steps, the membranes were incubated with alkaline phosphatase conjugated goat anti-human IgG (A3150, Sigma), or IgM (A3275, Sigma), or IgA (A3400, Sigma) at 1:30,000 dilution. Bound antibodies were detected using an ECF substrate following the manufacturer's instructions and imaged using a FLA-3000 Fujifilm scanner. Dialyzed IVIg was prepared using a 3.5k Slide-A-Lyzer (Thermo Fisher) in a solution of acetic acid at pH4 [40-41].

6.7.3 Two-Dimensional Western Blot

Briefly, 300 µL of CSF (containing approximately 120 µg of protein) were precipitated using ice-cold ethanol. The resulting protein pellet was dissolved in a solution of 9 M urea (Bio-Rad), 2% 2-mercaptoethanol (J.T. Baker), 2% IGEPAL (Sigma), and 0.25% carrier ampholytes (Bio-Rad). The sample was then loaded directly into a 18 cm, 3-10 nonlinear immobilized pH gradient (IPG) isoelectric focusing gel (GE Healthcare). A Protean IEF unit (Bio-Rad) was used to perform isoelectric focusing at 20 ºC for a total of 100 kVh. The IPG gels were equilibrated in solutions containing dithiothreitol (Bio-Rad) and subsequently iodoacetamide (Fluka) for reduction and alkylation of the focused proteins. Polyacrylamide gel electrophoresis was performed using 12-15% T gradient slab gels.

The gels were then immunoblotted and all subsequent steps were done at room temperature. Membranes were blocked in 3% non-fat dry milk for one hour and then probed with 10% as is or dialyzed Gammagard at 100 µg/mL for one hour. Following washing steps, the membranes were incubated with alkaline phosphatase conjugated goat anti-human IgG (A3150, Sigma), or IgM (A3275, Sigma), or IgA (A3400, Sigma) at 1:30,000 dilution. Bound antibodies

were detected using an ECF substrate following the manufacturer's instructions and imaged using a FLA-3000 Fujifilm scanner.

6.8 Acknowledgements

This work was funded by the National Institute of Health (NIH) and the Institute for the Study of Aging (ISOA). We thank Leila Choe and Jeffrey Foltz for important contributions. We also thank Dr. Brian Little at the Christiana Care Health System.

REFERENCES

1. Sapir, T., Shoenfeld, Y., 2005. Facing the enigma of immunomodulatory effects of intravenous immunoglobulin. *Clinical Reviews in Allergy & Immunology* 29, 185-199.
2. Kazatchkine, M.D., Kaveri, S.V., 2001. Immunomodulation of autoimmune and inflammatory diseases with intravenous immunoglobulin. *New Engl J Med*. 345, 747-755.
3. Gold, R., Stangel, M., Dalakas, M.C., 2007. Drug insight: the use of intravenous immunoglobulin in neurology-therapeutic considerations and practical issues. *Nat Clin Pract Neurol*. 3, 36.
4. Imbach, P., Barandun, S., dApuzzo, V., *et al.*, 1981. High-dose intravenous gammaglobulin for idiopathic thrombocytopenic purpura in childhood. *Lancet* 1, 1228-1231.
5. Dalakas, M.C., 1997. Intravenous immunoglobulin therapy for neurologic diseases. *Annals of Internal Medicine* 126, 721-730.
6. Kaveri, S.V., Mouthon, L.,Kazatchkine, M.D., 1994. Immunomodulating effects of intravenous immunoglobulin in autoimmune and inflammatory diseases. *Journal of Neurology, Neurosurgery, and Psychiatry* 57S, 6-8.
7. Dodel, R., Hampel, H., Depboylu, C., *et al*, 2002. Human antibodies against amyloid beta peptide: a potential treatment for Alzheimer's disease. *Ann Neurol.* 52, 253-256.
8. Weksler, M.E., Relkin, N., Turkenich, R., *et al.*, 2002. Patients with Alzheimer’s disease have lower levels of serum anti-amyloid peptide antibodies than healthy elderly individuals. *Exp. Gerontol*. 37 943-948.

9. Relkin, N.R., Szabo, P., Adamiak, B., 2008. 18-Month study of intravenous immunoglobulin for treatment of mild Alzheimer's disease. *Neurobiology of Aging*, in press.
10. Wurster, U., Hass, J., 1994. Passage of intravenous immunoglobulin and interaction with the CNS. *Journal of Neurology, Neurosurgery, and Psychiatry* 57(S), 21-25.
11. Lam, L., Whitsett, C.F., *et al.*, 1993. Immunologically active proteins in intravenous immunoglobulin. *Lancet* 342, 678.
12. Blasczyk, R., *et al.*, 1993. Soluble CD4, CD8, and HLA molecules in commercial immunoglobulin preparations. *Lancet* 341, 789-790.
13. Shoenfield, Y., *et al.*, 2002. Efficacy of IVIg affinity-purified anti-double-stranded DNA anti-tdiotypic antibodies in the treatment of an experimental murine model of systemic lupus erythematosus. *Int. Immunol*. 14, 1303.
14. Buchwald, B., Ahangari, R., *et al.*, 2002. Intravenous immunoglobulins neutralize blocking antibodies in Guillain-Barre syndrome. *Annal Neurol*. 51, 673.
15. Avrameas, S., 1991. Natural autoantibodies: from "horror autotoxins" to "gnothi seauton". *Immunol. Today* 12, 154-159.
16. Roux, K.H., Tankersley, D.L., 1990. A view of human idiotypic repertoire. *J. Immunol*. 144, 1387-13995.
17. Clarkson, S.B., Bussel, J.B., *et al.*, 1986. *New England Journal of Medicine* 314, 1236-1239.
18. Debre, M., Bonnet, M.C., 1993. *Lancet* 342, 945-949.
19. Yu, Z., Lennon, V.A., 1999. *New England Journal of Medicine* 340, 227-228.

20. Basta, M., Dalakas, M.D., 1994. *Journal of Clinical Investigation* 94, 1729-1735.

21. Sherer, Y., Wu, R., *et al.*, 2001. *Human Antibodies* 10, 51-53.

22. Choe, L.H., Werner, B.G., Lee, K.H., 2006. Two-dimensional protein electrophoresis: From molecular pathways discovery to biomarker discovery in neurological disorders. *NeuroRx* 3, 327-335.

23. D'Ascenzo, M., Relkin, N.R., Lee, K.H., 2005. Alzheimer's disease cerebrospinal fluid biomarker discovery: A proteomics approach. *Current Opinion in Molecular Therapeutics* 7, 557-564.

24. Jerne, N.K., 1974. Towards a network theory of the immune system. *Ann. Immunol.* 125C, 373-389.

25. Bhattacharya-Chatterjee, M., Chatterjee, S.K., Foon, K.A., 2000. Anti-idiotype vaccine against cancer. *Immunology Letters* 74, 51-58.

26. Shoenfeld, Y., 2004. The idiotype network in autoimmunity: antibodies that bind antibodies that bind antibodies. *Nature Medicine* 10, 17-18.

27. Pendergraft III, W.F., Preston, G., Shah, Ruchir, *et al.*, 2004. Autoimmunity is triggered by cPR-3 (105-201), a protein complementary to human autoantigen proteinase-3. *Nature Medicine* 10, 72-79.

28. Shoenfeld, Y., 1994. Idiotypic induction of autoimmunity: a new aspect of the idiotypic network. *FASEB J.* 8, 1296-1301.

29. Rossi, F., Kazatchkine, M.D., 1989. Anti-idiotypes against autoantibodies in pooled normal human poly-specific Ig. *Journal of Immunology* 143, 4104-4109.

30. Abdou, M.L.H, *et al.* 1981. Network theory in autoimmunity: *in vitro* suppression of serum anti-DNA antibody binding to DNA by anti-idiotypic antibody in systemic lupuserythematosus. *J. Clin. Invest*. 67, 1297.

31. Tanigushi, O., Chia, D.S., *et al.*, 1984. Auto-anti-anti-DNA antibodies from SLE patients and normals. *J. Rheumatol*. 3, 291.

32. Lefvert, A.K., Holm G., *et al.*, 1987. Cellular production of antibodies related to the achetylcholine receptor in myasthenia gravis: correlation with clinical stage. *Scand. J. Immunol*. 25, 265.

33. Sikorska, H.M., 1986. Anti-thyroblobulin anti-idiotypic antibodies in sera of patients with Hashimoto's thyroiditis and Grave's disease. *J. Immunol*. 137, 3786.

34. Page, N., Murray, N., *et al.*, 1985. A monoclonal antibody against a human monoclonal IgM with specificity for myelin-associated glycoprotein. *J. Immunol.* 134, 3094.

35. Gordon, D.S., 1987. Intravenous immunoglobulin therapy: new direction and unanswered questions. *Am. J. Med*. 83 (Suppl. 4A), 52.

36. Rossi, F., Dietrich, G., *et al.*, 1989. Anti-idiotypes against autoantibodies in normal immunoglobulins: evidence for network regulation of human autoimmune responses. *Immunol. Rev*. 110, 315.

37. Kazatchkine, M.D., Rossi, F., *et al.*, 1989. Clinical relevance of anti-idiotypic antibodies during treatment with IVIg. Central Laboratory of the Blood Transfusion Service, Amesterdam, p.125.

38. Finehout, E.J., Franck, Z., Lee, K.H., 2004. Towards two-dimensional electrophoresis mapping of the cerebrospinal fluid proteome from a single individual. *Electrophoresis* 25, 2564-2575.

39. Finehout, EJ, Frank, Z, Choe, L, *et al.*, 2007. Cerebrospinal fluid proteomic biomarkers for Alzheimer's disease. *Ann Neurol* 61, 120-129.

40. Schaub, A., Wymann, S., Heller, M., *et al.*, 2007. Self-reactivity in the dimeric intravenous immunoglobulin fraction. *Ann. NY Acad. Sci.* 1110, 681-693.

41. Miescher, S., Schaub, A., *et al.*, 2005. Comparative analysis of antigen specificities in the monomeric and dimeric fractions of intravenous immunoglobulin. *Ann. NY Acad. Sci*. 1051, 582-590.

CHAPTER 7

PROTEOMIC ANALYSIS OF DIAGNOSTIC BIOMARKERS FOR ALZHEIMER'S DISEASE RELATED TO INTRAVENOUS IMMUNOGLOBULIN THERAPY

7.1 Preface

This chapter is adapted from: Shayan, G., Relkin, N., Lee, K. H. 2010. Proteomic analysis of diagnostic biomarkers for Alzheimer's disease related to intravenous immunoglobulin therapy. *Clinical Chemistry*, in preparation. It reports on the identification of possible effects of IVIg on diagnostic biomarkers of Alzheimer's disease in a group of eight subjects who underwent immunotherapy using a Random Forest classification model.

7.2 Abstract

Intravenous immunoglobulin (IVIg) therapy has shown promising results in treating Alzheimer's disease (AD). In this study, a Random Forest classification model was used to identify possible effects of IVIg on a group of eight subjects who underwent immunotherapy. Cerebrospinal fluid (CSF) samples from eight AD subjects who underwent IVIg therapy were collected before the therapy, after six months of therapy, and after a three months drug washout period. Samples were analyzed using two-dimensional gel electrophoresis and further studied using a Random Forest classification model to identify effects of IVIg on a panel of 23 putative diagnostic AD biomarkers previously identified. Six of the eight subjects showed improvements with respect to the 23 AD diagnostic biomarkers after six

months of therapy compared to the samples taken before the trial. All subjects reverted back to baseline during drug washout. These results are also consistent with the clinical observations. The observed improvements in subjects during six months of IVIg therapy and the reversion back to baseline during drug washout provides preliminary evidence regarding the potential use of IVIg as an AD immunotherapy.

7.3 Introduction

According to recent estimates, as many as 5.3 million Americans are living with Alzheimer's disease (AD) [1]. AD is a progressive, neurodegenerative disorder affecting more than five percent of people over the age of 65 and is the leading cause of dementia in the elderly [2]. AD is characterized by a progressive cognitive decline associated with neurovascular dysfunction, accumulation of neurotoxic amlyloid beta (Aβ) on blood vessels and in the brain parenchyma, intraneuronal lesions, and neurofibrillar tangles [2].

Active immunization against Aβ in preclinical studies using transgenic animal models of AD resulted both in reduction of Aβ in the cerebrospinal fluid (CSF) and plaque burden [3-4]. The change in Aβ plaque burden was also associated with restored cognitive function in some of these transgenic animals [5-6]. Similar results were obtained in animal studies with passive immunization using monoclonal antibodies against Aβ [7].

There is significant interest in the use of passive immunotherapy to treat AD. Intravenous immunoglobulin (IVIg) is a pool of human immunoglobulins obtained from the blood of thousands of healthy donors that has been approved for more than two decades by the United States Food and Drug Administration for treatment of immune deficiency disorders and other

indications, but not AD. However, an initial study of IVIg in patients with neurologic diseases but not AD suggested that IVIg increased blood anti- Aβ antibody levels and fostered Aβ clearance [8].

An open label dose-ranging study in moderate AD subjects involved IVIg therapy for six months, which was discontinued for three months (washout period), and then resumed for another nine months [9]. As a result of this therapy, CSF Aβ decreased significantly after six months of therapy, returned to baseline after IVIg washout and decreased again after IVIg was re-administered. Mini-Mental State Examination (MMSE) scores increased an average of 2.5 points after six months, returned to baseline during washout, and remained stable during subsequent IVIg therapy. An important question is whether other molecular changes could be identified in the longitudinal CSF samples that were collected as part of this study.

Previously, a panel of 23 putative diagnostic AD biomarkers was identified and validated using proteomic analysis [10]. The proteins were separated using two-dimensional gel electrophoresis and the resulting pattern of protein expression was analyzed using the Random Forest (RF) multivariate statistical method. Here, CSF samples collected from AD subjects undergoing IVIg immunotherapy [9] is analyzed to characterize any potential response of the 23 biomarkers. CSF samples taken before the therapy, after six months of therapy, and after a three months IVIg washout were used for this study. The gels were analyzed using a previously described classification model [10] to identify possible effects of IVIg therapy on the panel of 23 AD biomarkers.

7.4 Materials and Methods

7.4.1 Cerebrospinal Fluid Samples

Lumbar CSF samples were obtained from eight subjects enrolled in a phase I clinical trial of IVIg therapy for the treatment of AD at Weill Cornell Medical College [9]. All subjects have been diagnosed with probable AD based on NINCDS-ADRDA criteria [11]. The subjects have been randomly assigned to one of four different dosing regimens: 0.4 g/kg every two weeks, 0.4 g/kg every week, 1 g/kg every two weeks, and 2 g/kg every month, as described previously [9]. Serial lumbar CSF samples taken before IVIg therapy, after six months of therapy, and after three months of IVIg washout were analyzed for this study. This information is summarized in Table 7.1. CSF samples were also collected at an interim time point within the first 6 months of therapy. For the washout period, a CSF sample from subject #5 was not available. The CSF samples and their corresponding 2DE gels appeared free from blood contamination. Samples were stored at -70°C until used.

7.4.2 Two-Dimensional Gel Electrophoresis

The CSF samples were separated using 2DE. The details of the 2DE protocol have been previously published [12]. Briefly, 300 µL of CSF (containing approximately 120 µg of protein) were precipitated using ice-cold ethanol. The resulting protein pellet was dissolved in a solution of 9 M urea (Bio-Rad), 2% 2-mercaptoethanol (J.T. Baker), 2% IGEPAL (Sigma), and 0.25% carrier ampholytes (Bio-Rad). The sample was then loaded directly into a 18 cm, 3-10 nonlinear immobilized pH gradient (IPG) isoelectric focusing gel (GE Healthcare). A Protean IEF unit (Bio-Rad) was used to perform isoelectric

Table 7.1 | Dosing and sample collection information for the eight AD subjects.

Subject	IVIg dose (g/kg)	# weeks between doses	Time of lumbar puncture (weeks since IVIg started)	
			6 months after therapy	Washout period
1	1.0	2	23.85	36.85
2	0.4	1	25.14	35.71
3	0.4	2	22.85	34.42
4	2.0	4	27	40.71
5	1.0	2	26.42	--
6	0.4	1	27.14	41.28
7	0.4	2	27.14	41.28
8	2.0	4	27	41.42

focusing at 20 ºC for a total of 100 kVh. The IPG gels were equilibrated in solutions containing dithiothreitol (Bio-Rad) and subsequently iodoacetamide (Fluka) for reduction and alkylation of the focused proteins. Polyacrylamide gel electrophoresis was performed using 12-15%T gradient slab gels. The separated proteins were fixed, stained with SYPRO Ruby Protein Gel Stain (Molecular Probes), and de-stained for 24 hours in a solution of 10% methanol and 7% acetic acid. The gels were scanned on a FLA-3000 Fluorescent Image Analyzer (Fujifilm Company).

The resulting gel images were imported into the Melanie software package (Version 4.0, GeneBio). The software was used to auto-detect spots that were subsequently manually edited to remove technical artifacts. Each sample gel was then matched to a master gel image created by combining the spots present in two gels from before the therapy, and two gels from the interim time point within the 6 months of thepray. Matching was initially performed using the software's automated matching tool and then checked and corrected manually.

7.4.3 Statistical Analysis

The gels were analyzed using a previously described classification model built using a set of AD and non-AD gels with the RF method [10]. The non-AD CSF samples included both normal and neurological control subjects. The classification model uses the percent volume data from 23 spots previously determined to be important in separating CSF 2DE gels from AD and non-AD subjects. A forest was built in the R environment and then used to predict the classification (AD class or non-AD class) of the IVIg gels. The percent of trees classifying the gels as AD or non-AD was recorded. For an IVIg gel, the

greater the percent of trees classifying the sample as AD, the more similar the percent volume data of the IVIg sample is to the percent volume data of the AD samples used to build the forest.

7.5 Results

The percent volume data for the 23 proteins previously identified to be useful in differentiating AD and non-AD CSF 2DE gels were extracted from the IVIg gels and recorded. This data was run through a classification forest built using 68 CSF 2DE gels (34 AD, 34 non-AD). Based on these 23 spots, all of the IVIg gels, corresponding to CSF taken before the therapy, after six months, and during washout were classified as AD. A classification of AD indicates that over 50% of the trees in the forest classified the sample in the AD category. These data are plotted in Figure 7.1. Six of the eight subjects (1-6) received a lower AD classification after six months of therapy compared to the samples taken before the trial. All of these subjects (except for subject #5, whose CSF sample was not available during washout) received a higher AD classification during the washout compared to the samples taken during the IVIg therapy.

Relkin *et al.* observed that after six months of IVIg immunotherapy, the group's MMSE scores increased on average by 2.5 points. After IVIg washout, MMSE scores declined towards baseline. In the current RF analysis, the lower AD predictions during IVIg immunotherapy and the reversion during drug washout was consistent with observed MMSE score changes. The correlation coefficient between changes in MMSE and AD classification during IVIg therapy and drug washout were 0.11 and 0.95, respectively. Figure 7.2, shows the AD classification normalized with baseline for all patients to monitor for possible dose dependent effects.

Figure 7.1 | Fraction of votes for each CSF sample using a previously built Random Forest classification model. The patient numbers refer to the dosing schedules listed in Table 7.1.

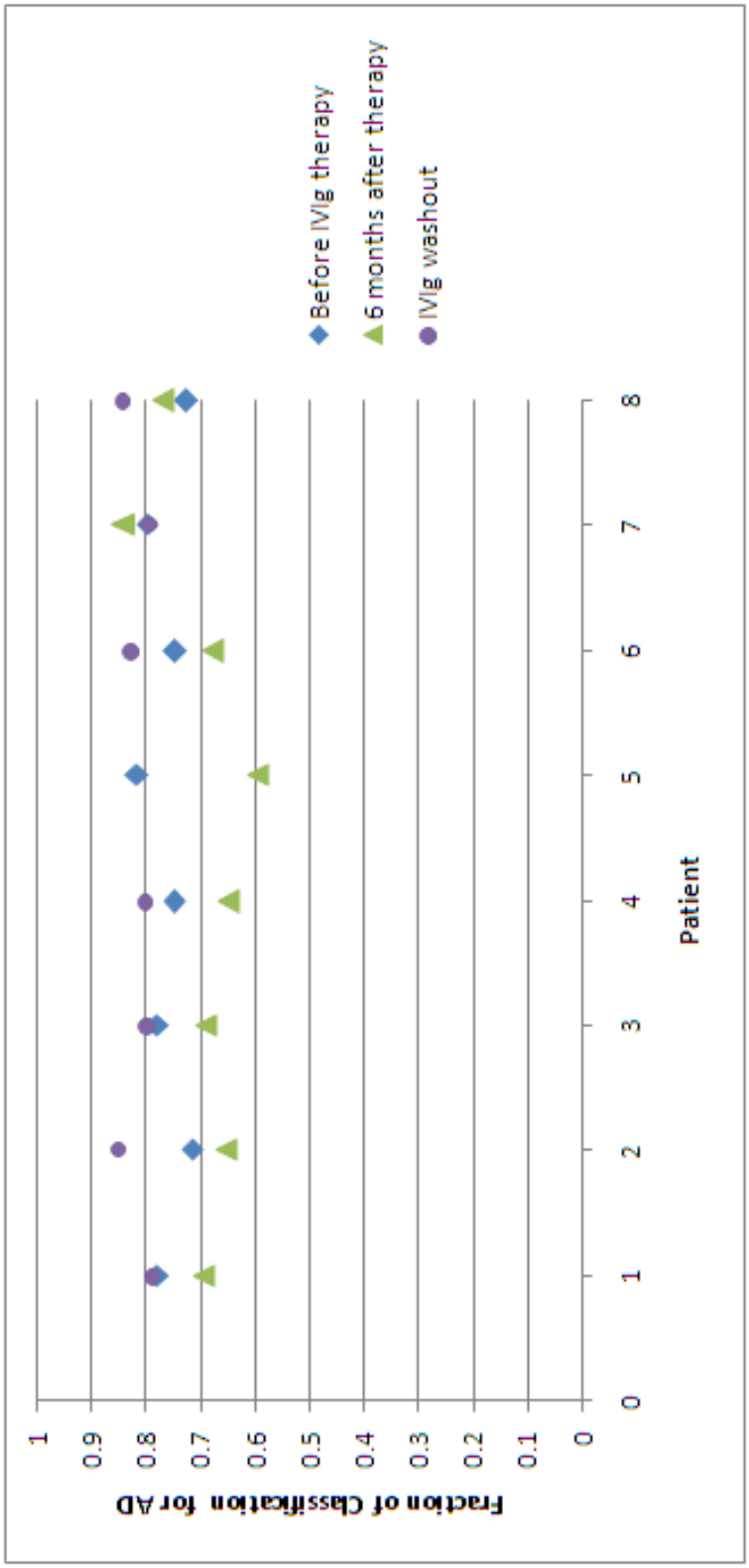
Before IVig therapy
6 months after therapy
IVig washout
Fraction of Classification for AD
Patient
1
0.9
0.8
0.7
0.6
0.5
0.4
0.3
0.2
0.1
0
0
1
2
3
4
5
6
7
8

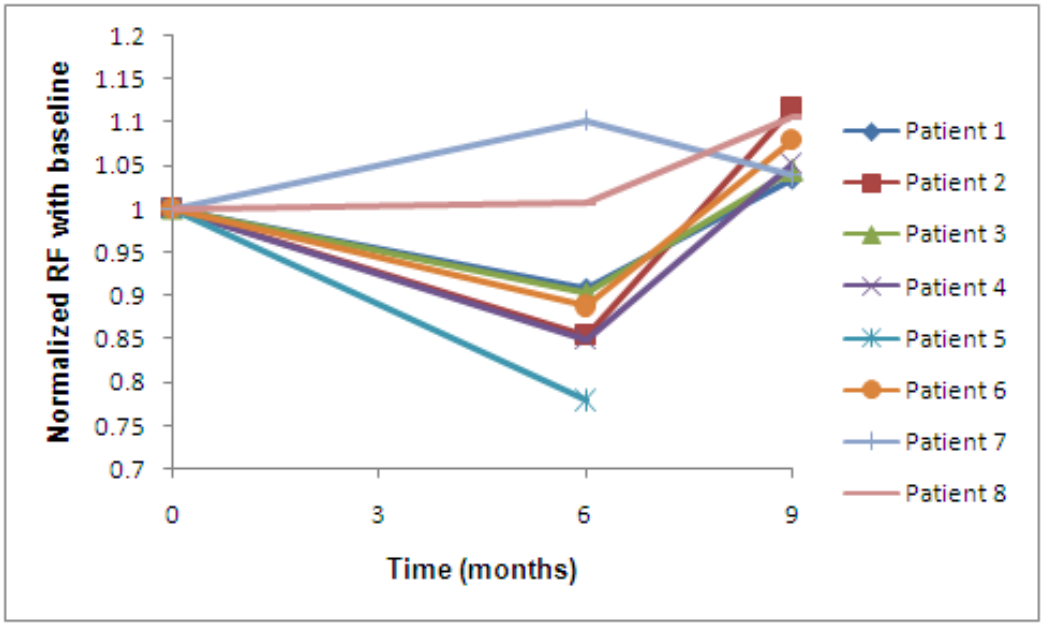

Figure 7.2 | Fraction of AD classification normalized with baseline for each patient. Patients receiving 1g/kg/2wk and 0.4g/kg/1wk showed a lower AD classification during IVIg therapy. Relkin *et al.* also observed optimum changes in MMSE scores in patients who received 1g/kg/2wk of IVIg.

7.6 Discussion

In this study, CSF samples from AD subjects undergoing IVIg therapy were analyzed using two-dimensional gel electrophoresis. The data was studied using the previously developed RF classification model to identify longitudinal effects of IVIg therapy on the panel of 23 AD diagnostic biomarkers. In the RF method, for any sample, the higher the AD prediction for one class (AD or non-AD), the more similar the sample is to that class. According to this analysis, six of the eight AD subjects received a lower AD classification after six months of IVIg therapy, and these predictions reverted to baseline after IVIg washout.

Relkin *et al.* [9] reported that the administration of IVIg to the eight subjects with moderate AD led to transient, reproducible, and dose dependent increases in serum anti-Aβ antibody titers and parallel increases in plasma Aβ40 and Aβ42 levels. It was also observed that after six months of IVIg immunotherapy, CSF Aβ40 and Aβ42 levels decreased and the group's MMSE scores increased on average by 2.5 points, following a decline towards baseline during the drug washout. The consistency between the RF results and the MMSE scores suggests the possibility that the panel of 23 previously proposed diagnostic biomarkers may reflect disease severity or cognition.

Here, subjects 1-6 showed a decline in fraction of AD classifications during IVIg therapy, while subjects 7-8 did not show a similar response. MMSE scores for subject 7 at baseline, after six months of treatment, and after IVIg washout were 25, 28, and 24 respectively corresponding to 80%, 84%, and 79% AD classification (Figure 7.1). MMSE scores for subject 8 at baseline, after 6 months of treatment, and after IVIg washout were 20, 20, and 18 respectively corresponding to 72%, 76%, and 84% AD classification (Figure

7.1). These MMSE scores are also consistent with the RF observations for these subjects.

The fraction of AD classifications after the washout period shows a significant increase from baseline in subjects 2 and 6. The MMSE scores for these two subjects, who also received the same dose of IVIg, improved significantly during therapy, and was unchanged during the washout period [9]. While the majority of the observations related to RF and MMSE scores are consistent, the washout results for these two subjects suggests the possibility that the 23 diagnostic biomarkers may not accurately reflect MMSE scores in all cases. This is also reflected in the poor correlation coefficient between MMSE and AD classification changes during IVIg therapy. One possible reason is that the RF analysis measures changes in the 23 AD biomarkers, and it is possible that disease-modifying effects of IVIg goes beyond the panel of 23 AD biomarkers. If true, then the direction of change of the MMSE score may not correspond to a similar change in the panel of 23 diagnostic biomarkers in all cases.

By performing a proteomic and RF statistical analysis, we showed that six of the eight subjects who underwent IVIg therapy received lower AD classifications with respect to the 23 AD biomarkers after the therapy. These results are in agreement with the reported clinical outcomes, and also provide an example on how proteomic biomarkers may be useful in assessing treatment paradigms for AD. However, additional studies with a larger cohort size are necessary to fully correlate the statistical results with clinical outcomes. We believe that longitudinal AD CSF studies proposed in the context of clinical tools are critically needed and this report is the first such study using proteomic biomarkers.

7.7 Acknowledgements

This work was funded by the National Institute of Health (NIH) and the Institute for the Study of Aging (ISOA). We thank Leila Choe, Erin Finehout, Zsofia Franck, and Heather Roman for important contributions.

REFERENCES

1. 2009. Alzheimer's Disease facts and figures. *Alzheimer's & Dementia* 5, 234-270.
2. Cummings, JL, Cole, G., 2002. Alzheimer disease. *JAMA* 287, 2335-2338.
3. Schenk, D, Barbour, R, Dunn, W, *et al.*, 1999. Immunization with amyloid-beta attenuates Alzheimer-disease like pathology in the PDAPP mouse. *Nature* 400, 173-177.
4. Demattos, RB, Bales, KR, Cummins, DJ, *et al.*, 2001. Peripheral anti-amyloid-beta antibody alters CNS and plasma Aβ clearance and decreases brain Aβ burden in a mouse model of Alzheimer's disease. *PNAS* 98, 8850-8855.
5. Morgan, D, Diamond, DM, Gottschall, PE, *et al.*, 2000. Aβ peptide vaccination prevents memory loss in an animal model of Alzheimer's disease. *Nature* 408, 982-985.
6. Dodart, JC, Bales, KR, Gannon, KS, *et al.*, 2002. Immunization reverses memory deficits without reducing brain Aβ burden in Alzheimer's disease model. *Nature Neuroscience* 5, 452-457.
7. Bard, F, Cannon, C, Barbour, R, *et al.*, 2000. Peripherally administered antibodies against Aβ-peptide enter the central nervous system and reduce pathology in a mouse model of Alzheimer's disease. *Nature Med* 6, 916-919.
8. Dodel, R, Hampel, H, Depboylu, C, Lin, S, *et al.*, 2002. Human antibodies against Aβ-peptide: a potential treatment for Alzheimer's disease. *Ann Neurol* 52, 253-256.

9. Relkin, NR, Szabo, P, Adamiak, B, *et al.*, 2008. 18-Month study of intravenous immunoglobulin for treatment of mild Alzheimer disease. *Neurobiology of Aging*, in press.
10. Finehout, EJ, Frank, Z, Choe, L, *et al.*, 2007. Cerebrospinal fluid proteomic biomarkers for Alzheimer's disease. *Ann Neurol* 61, 120-129.
11. McKhann, G, Drachman, D, *et al.,* 1984. Clinical diagnosis of Alzheimer's disease- report of the NINCDS-ADRDA Work Group under the auspices of Department of Health and Human Services task force on Alzheimer's disease. *Neurology* 34, 939-944.
12. Hatzimanikatis, V, Choe, LH, Lee, KH, 1999. Proteomics: Theoretical and experimental considerations. *Biotechnol Prog* 15, 312-318.

CHAPTER 8

EFFECTS OF INTRAVENOUS IMMUNOGLOBULIN ON CEREBROSPINAL FLUID PROTEOME IN ALZHEIMER'S DISEASE

8.1 Preface

This chapter is adapted from: Shayan, G., Relkin, N., Lee, K. H. 2010. Effects of intravenous immunoglobulin on cerebrospinal fluid proteome in Alzheimer's disease. *Annals of Neurology*, in preparation. It reports on the identification of IVIg induced changes in cerebrospinal fluid samples from a group of subjects with AD who underwent IVIg therapy.

8.2 Abstract

Intravenous immunoglobulin (IVIg) therapy has shown promising results in treating Alzheimer's disease (AD). In this study, serial cerebrospinal fluid (CSF) samples from a group of subjects with AD who underwent IVIg therapy are analyzed to identify IVIg-induced changes. CSF samples from eight AD subjects who underwent IVIg therapy were collected before the therapy, after six months of therapy, and after a three months drug washout period. Samples were analyzed using a gel-based proteomics strategy to identify IVIg-induced changes using two different statistical approaches. The first analysis revealed sixty nine proteins that showed a considerable and consistent change during IVIg treatment. The second analysis identified 25 proteins that changed significantly after six months of therapy, and then the change was sustained or reversed during the washout period including Ig molecules, gelsolin, transferrin, transthyretin and other proteins. The proteins that showed a

significant change during IVIg therapy have been previously implicated in AD. This study provides preliminary evidence regarding the potential group of CSF proteins that may be implicated in the treatment of AD as well as the potential use of IVIg as an AD immunotherapy.

8.3 Introduction

Alzheimer's disease (AD) is the leading cause of dementia in the elderly and affects over 5.3 million people in the United States [1]. The disease is characterized by amnestic type memory impairment and deterioration of language skills, all of which progressively worsen over the course of the disease [2-4]. Histopathologically, AD is characterized by intracellular tangles of tau protein and extracellular plaques that are primarily composed of amyloid beta (Aβ) [5].

Active immunization against Aβ in preclinical studies using transgenic animal models of AD resulted both in reduction of Aβ in the cerebrospinal fluid (CSF) and plaque burden [3-4]. The change in Aβ plaque burden was also associated with restored cognitive function in some of these transgenic animals [5-6]. Similar results were obtained in animal studies with passive immunization using monoclonal antibodies against Aβ [7].

An approach to passive immunization is the use of intravenous immunoglobulin (IVIg) therapy. IVIg is a biological product that contains intact IgG molecules with a distribution of IgG subclasses equivalent to that in normal human serum [8]. After an IVIg infusion of 2 g/kg (a typical dose used to treat other neurological diseases) the serum IgG levels are found to increase fivefold. The serum levels return to baseline after 21 to 28 days. IgG

levels in the CSF are found to increase two fold over the first 48 hours and then return to normal within a week [9].

When subjects with various neurological disorders were given IVIg infusions, there was a significant increase in anti-Aβ antibodies in both the CSF and serum. In the CSF, the total amount of Aβ and the amount of $A\beta_{1-42}$ was shown to significantly decrease after the IVIg infusions. In the serum, however, the total amount of Aβ significantly increased after the IVIg infusions [10]. There are several proposed effects of the anti-Aβ antibodies in AD subjects. The first is that the antibodies bind to the aggregated Aβ and recruit microglia to phagocytose the aggregates [11]. The second proposed effect suggests that the anti-Aβ antibodies provide a peripheral sink for Aβ causing the Aβ to leave the CNS and enter the plasma where it is degraded [4,12]. Lastly, there is evidence that anti-Aβ antibodies prevent Aβ aggregation and may be able to break up already formed aggregates [13-14].

Dodel *et al.* reported results of a pilot study with five AD subjects who were given 0.4 g/kg IVIg every four weeks over the course of six months [15]. They reported that the CSF concentration of total Aβ decreased by 30% and the serum concentration increased by 233%. Based on Mini-Mental State Examination (MMSE) scores before and after six months of IVIg treatment, none of the five subjects showed any cognitive decline, and several showed an improvement [15].

In an open label dose-ranging study, moderate AD subjects were treated with IVIg for six months, followed by a three months washout period, and then resumed treatment for another nine months [16]. As a result of this therapy, CSF Aβ decreased significantly after six months of therapy, returned to baseline after IVIg washout and decreased again after IVIg was re-

administered. MMSE scores increased an average of 2.5 points after six months, returned to baseline during washout, and remained stable during subsequent IVIg therapy. An analysis of the longitudinal changes in CSF protein expression may provide insights into any disease modifying effects of IVIg treatment.

In this report, serial CSF samples collected from AD subjects undergoing IVIg immunotherapy [16] are analyzed using two-dimensional gel electrophoresis (2DE) to characterize the potential effects of IVIg treatment. CSF samples taken before the therapy, after six months of therapy, and after a three months IVIg washout were used for this study. Using two separate statistical analyses, proteins with significant concentration changes during the therapy followed by sustained or reversed changes during the washout were identified. These changes identify possible surrogate endpoints of AD therapy and give information about the IVIg therapeutic mechanism of action in AD subjects. This study is the first to report on the analysis of serial CSF samples from subjects to monitor therapy-induced changes in the CSF proteome.

8.4 Materials and Methods

8.4.1 Cerebrospinal Fluid Samples

With institution review board approval, lumbar CSF samples were obtained from eight subjects enrolled in a phase I clinical trial of IVIg therapy for the treatment of AD at Weill Cornell Medical college [16]. All subjects have been diagnosed with probable AD based on NINCDS-ADRDA criteria [17]. The subjects have been randomly assigned to one of four different dosing regimens: 0.4 g/kg every two weeks, 0.4 g/kg every week, 1 g/kg every two weeks, and 2 g/kg every month. Serial lumbar CSF samples taken before IVIg

therapy (t=0), after six months of therapy (t=6), and after three months of IVIg washout (t=9) were analyzed for this study. This information is summarized in Table 8.1. CSF samples were also collected at an interim time point within the first six months of therapy. For the washout period, a CSF sample from subject #5 was not available. The CSF samples and their corresponding 2DE gels appeared free from blood contamination. Samples were stored at -70°C until used.

8.4.2 Two-Dimensional Gel Electrophoresis

The CSF samples were separated using 2DE. The details of the 2DE protocol have been previously published [18]. Briefly, 300 µL of CSF (containing approximately 120 µg of protein) were precipitated using ice-cold ethanol. The resulting protein pellet was dissolved in a solution of 9 M urea (Bio-Rad), 2% 2-mercaptoethanol (J.T. Baker), 2% IGEPAL (Sigma), and 0.25% carrier ampholytes (Bio-Rad). The sample was then loaded directly into a 18 cm, 3-10 nonlinear immobilized pH gradient (IPG) isoelectric focusing gel (GE Healthcare). A Protean IEF unit (Bio-Rad) was used to perform isoelectric focusing at 20 ºC for a total of 100 kVh. The IPG gels were equilibrated in solutions containing dithiothreitol (Bio-Rad) and subsequently iodoacetamide (Fluka) for reduction and alkylation of the focused proteins. Polyacrylamide gel electrophoresis was performed using 12-15% T gradient slab gels. The separated proteins were fixed, stained with SYPRO Ruby Protein Gel Stain (Molecular Probes), and de-stained for 24 hours in a solution of 10% methanol and 7% acetic acid. The gels were scanned on a FLA-3000 Fluorescent Image Analyzer (Fujifilm Company).

Table 8.1 | Dosing and sample collection information for the eight AD subjects.

Subject	IVIg dose (g/kg)	# weeks between doses	Time of lumbar puncture (weeks since IVIg started)	
			6 months after therapy	Washout period
1	1.0	2	23.85	36.85
2	0.4	1	25.14	35.71
3	0.4	2	22.85	34.42
4	2.0	4	27	40.71
5	1.0	2	26.42	--
6	0.4	1	27.14	41.28
7	0.4	2	27.14	41.28
8	2.0	4	27	41.42

The resulting gel images were imported into the Melanie software package (Version 4.0, GeneBio). The software was used to auto-detect spots that were subsequently manually corrected to remove technical artifacts. Each sample gel was then matched to a master gel image created by combining the spots present in two gels from before the therapy, and two gels from the interim time point within the six months of therapy. Matching was initially performed using the software's automated matching tool and then checked and corrected manually. The percent integrated intensity (percent volume) of each matched spot was then exported.

8.4.3 Statistical Analysis

An initial analysis was performed to identify spots that showed a consistent and considerable change in percent volume between the CSF samples collected before the IVIg therapy and after six months of therapy. A spot percent volume was deemed a consistent change if the same direction of change was observed in at least seven of the eight subjects. The change was considerable if there was greater than a two-fold change in at least five of the subjects.

An alternate statistical analysis was carried out using JMP® 7.0 (SAS Institute Inc., Cary, NC, USA) [19]. In this analysis, the percent volume data of the identified spots on the gels from CSF samples at t=0 and t=6 (from all eight subjects) that showed a normal distribution, were fitted to a linear mixed model using JMP Restricted Maximum Likelihood (REML) estimation method. In the Fit Model function of JMP, percent volume data was chosen as a role variable. Time of CSF sample collection, IVIg dose, the crossed interaction between time and dose were chosen as model effects. Dose was then nested

within patients and was chosen as the random effect. This analysis identified 79 proteins with a significant change in percent volume after six months of IVIg therapy. None of these spots showed a significant change with respect to dose, or the interaction between time and dose. The same statistical analysis was then applied to the % volume of the 79 identified proteins in samples collected after six months of IVIg therapy (t=6) and the washout period (t=9) from all eight subjects (except subject #5). The purpose of this second analysis was to identify proteins out of the pool of 79 spots whose percent volume changed significantly after IVIg therapy with this change being significantly sustained or reversed during drug washout. The global risk was fixed at $p < 0.05$ for all tests.

8.4.4 Protein Identification

Some of the proteins in the 2DE spots that showed a change in percent volume with IVIg therapy were identified with a 2DE CSF map [20]. Other spots were identified using tryptic digestion followed by tandem mass spectrometry (MS). The details of the digestion and MS analysis protocols have been previously published [21]. The MS analysis was done using a matrix-assisted laser desorption/ionization tandem time-of-flight MS (MALDI-TOF/TOF MS, Applied Biosystems). Peptide mass fingerprint data were collected in positive ion reflector mode in the range of 900 to 4000 mass to charge ratio. Several of the highest intensity non-trypsin peaks were then selected for tandem mass spectrometry analysis. The spectra were analyzed using GPS Explorer (Version 2.0, Applied Biosystems), which acts as an interface between the Oracle database containing raw spectra and a local copy of the Mascot search engine (Version 2.0, [22]). The spectral data were

searched against a locally stored copy of the NCBInr human protein database [23] using the Mascot search engine. A mass tolerance of 25 ppm was used for the peptide mass fingerprint data and 0.2 Da for the tandem mass spectrometry data. For a database match to be considered a positive identification, a value of $p < 0.05$ (calculated by GPS Explorer) was required.

8.5 Results

A typical CSF 2DE gel from samples before the IVIg therapy is shown in Figure 8.1. The number of spots on the CSF 2DE gels did not change significantly over the course of the IVIg treatment. There were an average of 1178 +/- 192 spots in the t=0 CSF gels and 1173 +/- 161 spots in the t=6 CSF gels. In the initial analysis, 69 spots demonstrated a consistent and considerable change in percent volume between the t=0 and the t=6 CSF gels. The direction of change for these 69 2DE spots, along with information on the protein(s) identified in the spots, is summarized in Table 8.2. All of the 2DE spots in Table 8.2 (except for spots 6017 and 1378) show a decrease in percent volume after IVIg treatment.

In the alternate statistical analysis using JMP® 7.0, 79 spots demonstrated a significant change in percent volume between the t=0 and the t=6 CSF gels. None of these spots showed a significant change with respect to dose or the interaction between time and dose. In the pool of 79 spots, only 25 spots showed a change that was sustained or reversed in the t=9 CSF gels compared to the changes between t=0 and t=6 CSF gels. Table 8.3 lists the 25 proteins with their corresponding *p* values and the direction of change between t=0, t=6, and t=9 CSF gels.

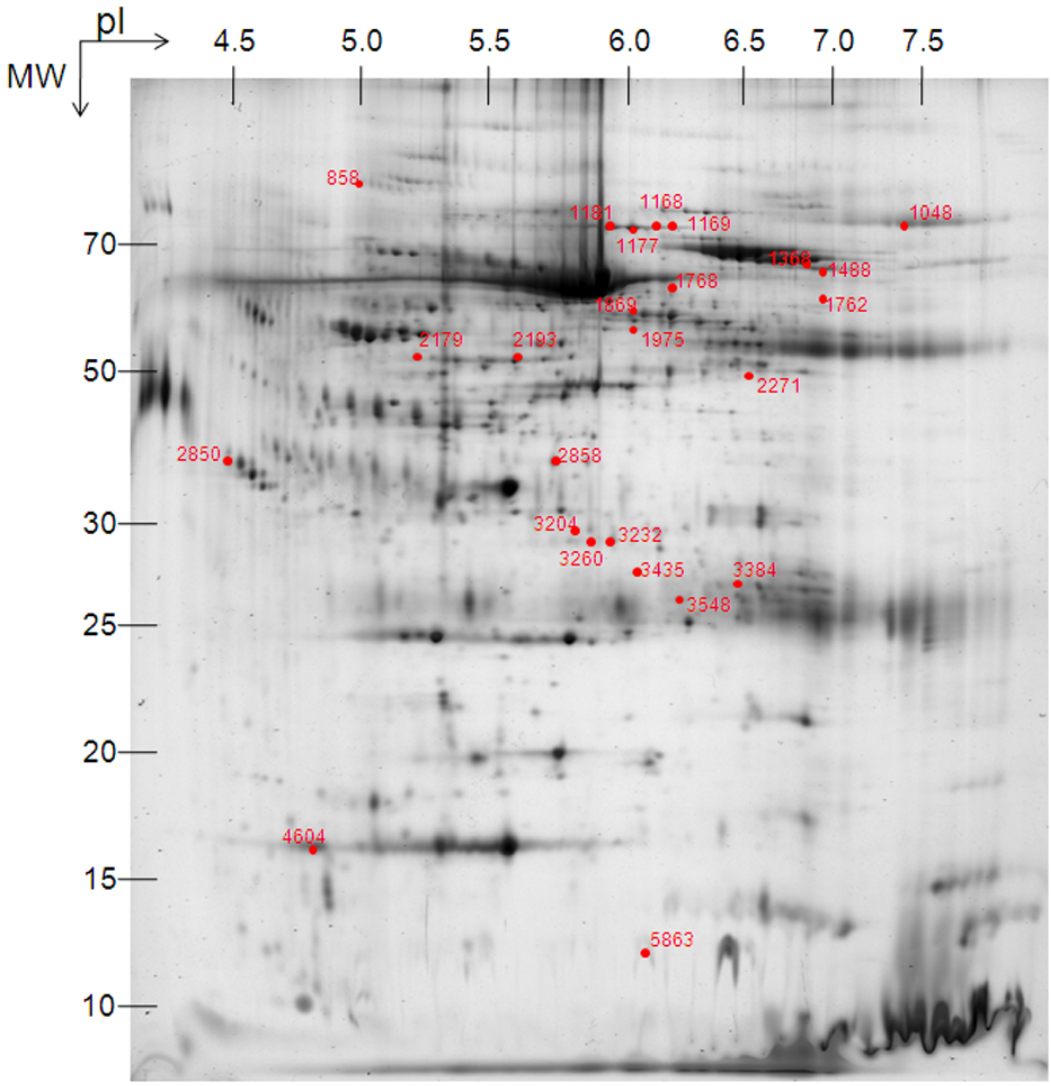

Figure 8.1 | 2DE gel of CSF from subject #7 at baseline. Proteins from Table 8.3 are labeled with their ID number.

Table 8.2 | 2DE spots that show a consistent and considerable change in the percent volume after six months of IVIg therapy.

ID#	Protein ID	NCBI [33] Accession #	Observed/ Calculated MW (kDa)	Δ t=0 to t=6
2850	α-1-antitrypsin	1942629	52/44.3	-
2905	α-1-antitrypsin	1942629	51/44.3	-
2335	α-1-antitrypsin	1942629	48/44.3	-
5867	α-1-antitrypsin	1942629	18/44.3	-
6017	α-1-antitrypsin	1942629	16/44.3	+
1378	α-1-B-glycoprotein	69990	88/51.9	+
1010	Albumin	113576	105/69.4	-
1037	Albumin	113576	105/69.4	-
1593	Albumin	113576	72/69.4	-
1861	Albumin	113576	64/69.4	-
6031	Albumin	113576	53/69.4	-
2172	Albumin	113576	53/69.4	-
2185	Albumin	113576	51/69.4	-
5977	Albumin	113576	45/69.4	-
2863	Albumin	113576	38/69.4	-
3463	Albumin	113576	27/69.4	-
3458	Albumin	113576	27/69.4	-
4354	Albumin	113576	15/69.4	-
4537	Albumin	113576	14/69.4	-
3643	Albumin	113576	24/69.4	-
3481	Albumin	113576	28/69.4	-
2964	Apolipoprotein E	178853	37/36.2	-
3048	Apolipoprotein E	178853	35/36.2	-
5931	Apolipoprotein E	178853	15/36.2	-
2775	Apolipoprotein J	178855	40/48.8	-
2976	Apolipoprotein J	178855	34/48.8	-
1946	α-2-glycoprotein I	4557327	63/38.3	-
1432	BiP Protein	6470150	88/70.9	-
1804	Complement Factor B	291922	65/85.5	-
1133	Contactin 1	28373119	100/112	-
712	Contactin 2	4827022	128/113	-
713	Contactin 2	4827022	128/113	-
3204	Cyclin D-1	483601	32/7.6	-
3065	EPC-1	1144299	33/40.1	-
3260	EPC-1	1144299	31/40.1	-
2179	EPC-1/Albumin	182424	75/69.8	-
1566	Fibrinogen Alpha	4504165	100/85.7	-
1168	Gelsolin	4504165	100/85.7	-
1174	Gelsolin	4504165	100/85.7	-
1169	Gelsolin	4504165	100/85.7	-
1177	Gelsolin	4504165	100/85.7	-
4682	Gelsolin	4504165	80/85.7	-
1440	Gelsolin	4504165	65/85.7	-

Table 8.2 (Continued)

4682	Gelsolin	4504165	80/85.7	-
1440	Gelsolin	4504165	65/85.7	-
1839	Gelsolin	229908	36/25.2	-
2989	Malate Dehydrogenase	14585855	24/25.7	-
903	Plasminogen	135807	95/70.0	-
1272	Prothrombin	553788	80/53.8	-
1368	Transferrin	553788	80/53.8	-
1393	Transferrin	553788	44/53.8	-
2513	Transferrin	339685	19/12.8	-
4180	Transthyretin	72146	13/54.3	-
4648	Vitronectin	--	120/--	-
858	Unknown	--	105/--	-
1054	Unknown	--	100/--	-
1231	Unknown	--	80/--	-
1523	Unknown	--	75/--	-
5958	Unknown	--	70/--	-
1559	Unknown	--	65/--	-
1796	Unknown	--	58/--	-
2051	Unknown	--	53/--	-
2545	Unknown	--	41/--	-
2694	Unknown	--	35/--	-
3009	Unknown	--	33/--	-
3249	Unknown	--	27/--	-
3464	Unknown	--	24/--	-
3653	Unknown	--	23/--	-
5919	Unknown	--	23/--	-
3784	Unknown	--	19/--	-
4307	Unknown	--	18/--	-

Table 8.3 | 2DE spots that show a significant change in percent volume after six months of IVIg therapy followed by a sustained or reversed effect during washout. Spots are ordered with respect to *p* values.

ID#	Protein ID	NCBI [33] Accession #	MW (kDa)	Direction of Change	*p Value*
2179	EPC-1	1144299	53/40.1	0>6=9	0.0004
1169	Gelsolin	4504165	100/85.7	0>6=9	0.0005
2850	α-1 anti-trypsin	1942629	52/44.3	0>6=9	0.0005
1168	Gelsolin	4504165	100/85.7	0>6=9	0.0013
2193	Fibrinogen γ	223170	53/46.2	0>6<9	0.0017
1869	Albumin	113576	63/69.4	0>6<9	0.0028
2271	Complement Factor H	758073	70/51	0>6<9	0.0029
3232	Albumin	113576	32/69.4	0>6=9	0.0032
3260	Unknown	--	30/--	0>6<9	0.0033
858	Inter-α trypsin inhibitor	Q14624	120/103.3	0>6=9	0.0045
3384	Kallikrein 6 preprotein	4506155	27/26.9	0<6=9	0.0064
1177	Gelsolin	4504165	100/85.7	0>6=9	0.0068
1181	Gelsolin	4504165	100/85.7	0>6=9	0.0068
1488	Complement component 3	4557385	78/187	0>6<9	0.007
2858	Albumin	113576	40/69.4	0>6=9	0.0073
1762	Unknown	--	45/--	0>6<9	0.0076
3435	Unknown	--	28/--	0>6=9	0.0084
1048	Ig	226787	95/25	0<6>9	0.0089
1368	Transferrin	553788	85/53.8	0>6<9	0.0094
3548	Ig light chain	21669471	25/28.2	0<6>9	0.0098
1975	Albumin	113576	65/69.4	0>6=9	0.015
3204	Unknown	--	32/--	0>6<9	0.0167
1768	Unknown	--	68/--	0>6<9	0.0174
5863	Unknown	--	25/--	0<6=9	0.0198
4604	Transthyretin	339685	14/12.8	0<6=9	0.0396

Proteins in Table 8.3 can be categorized in two groups based on whether their concentration increased (green and black) or decreased (blue and red) during six months of therapy. Proteins within each of the above categories were further divided in two categories: those showing a sustained effect (black and blue) or those showing a reversion (green and red) during washout.

8.6 Discussion

In the initial analysis, several proteins appeared at least four times in Table 8.2. It is possible for a given protein to appear at multiple positions in a 2DE gel because of the presence of isoforms, post translational modifications or degradation fragments. The alternate statistical analysis identified 25 spots (Table 8.3) with CSF expression changes between t=0 and t=6, and a sustained or reversed change during IVIg washout. Besides those spots common to both tables (discussed below), Table 8.2 contains proteins linked to AD such as ApoE and ApoJ, with the later being recently implicated in AD [24-25].

Our analysis of the longitudinal changes in CSF protein expression using 2DE has resulted in exciting observations. First, all of the spots with a known protein identity in Table 8.3 (with some present in Table 8.2), have been previously implicated in AD. Second, the sensitivity of the experiments and thus the observed direction of changes for these proteins are consistent with previous reports regarding the changes in their concentration in AD. Third, two of the proteins, Ig light chain and complement component 3, have also been previously implicated as diagnostic biomarkers of AD [25]. For discussion, the proteins in Table 8.3 are arranged in two categories: proteins

with an increase in CSF expression after IVIg therapy, and proteins with a decrease in expression after therapy, respectively.

Ig, Ig light chain, kallikrein 6 preprotein, and transthyretin show elevated CSF expression after six months of IVIg therapy. In the case of the immunoglobulins, this increase is mitigated during washout which is consistent with the nature of immunotherapy and the transport of antibodies into CSF after peripheral administration. The increase in CSF expression of kallikrein 6 and transthyretin after therapy is consistent with previous reports regarding the reduced levels of these proteins in the CSF of patients with AD [26-28]. Kallikrein 6, a serine protease, is highly expressed in the brain and transthyretin has been shown to bind Aβ [26-27].

EPC-1,gelsolin, α-1 anti-trypsin, albumin, and inter-α trypsin inhibitor all show a decrease in CSF expression after IVIg treatment, with a sustained effect during IVIg washout. The decrease in expression of EPC-1, gelsolin, and α-1 anti-trypsin is consistent with previous studies showing increased expression of these proteins in the brain or CSF of AD patients [29-35]. Inter-α-trypsin inhibitor, a plasma protease inhibitor, has been shown to be related to the pathogenesis of AD, specifically by playing a role in the formation of senile plaques and neuronal degradation [36].

Fibrinogen γ, transferrin, complement factor H, and complement component 3 also show a decrease in CSF expression after IVIg treatment. However, this change is reversed after IVIg washout, which may imply that the effect of IVIg on these proteins is not as long term as on the proteins discussed above. The decrease in expression of fibrinogen, an Aβ binding protein, and transferrin is consistent with previous studies showing elevated levels of them in the brain or CSF of AD patients [37-39]. With respect to the

complement proteins, several studies have indicated that there is a change in complement activity in the brains of patients with AD [40], and that some of its isoforms are Aβ binding proteins.

This study is the first to report on the longitudinal analysis of CSF samples from a set of clinical trial subjects to monitor therapy-induced changes in the CSF proteome. It is also the first study to report on possible protein targets of IVIg in CSF of AD subjects. The results suggest that changes in the CSF proteome after IVIg therapy can be detected using 2DE when analyzed with robust statistical analyses. Thus, a proteomic analysis of the CSF may be useful in the search for biomarkers and possible surrogate endpoints to monitor a subject's response to therapy. Although additional studies with a larger cohort size are necessary to fully correlate the statistical results with clinical outcomes, we believe that longitudinal AD CSF studies proposed in the context of therapy-induced changes are critically needed to identify diagnostic and/or treatment biomarkers of AD.

8.7 Acknowledgments

This work was funded by the National Institute of Health (NIH) and the Institute for the Study of Aging (ISOA). We thank Leila Choe, Erin Finehout, Zsofia Franck, and Heather Roman for important contributions.

REFERENCES

1. 2009. Alzheimer's Disease facts and figures. *Alzheimer's & Dementia* 5, 234-270.
2. Price, BH, Gurvit, H, Weintraub, S, *et al.*, 1993. Neuropsychological patterns and language deficits in 20 consecutive cases of autopsy-confirmed Alzheimer's disease. *Arch Neurol*. 50(9), 931-937.
3. Schenk, D, Barbour, R, Dunn, W, *et al.*, 1999. Immunization with amyloid-beta attenuates Alzheimer-disease like pathology in the PDAPP mouse. *Nature* 400, 173-177.
4. Demattos, RB, Bales, KR, Cummins, DJ, *et al.,* 2001. Peripheral anti-amyloid-beta antibody alters CNS and plasma Aβ clearance and decreases brain Aβ burden in a mouse model of Alzheimer's disease. *PNAS* 98, 8850-8855.
5. Morgan, D, Diamond, DM, Gottschall, PE, *et al.,* 2000. Aβ peptide vaccination prevents memory loss in an animal model of Alzheimer's disease. *Nature* 408, 982-985.
6. Dodart, JC, Bales, KR, Gannon, KS, *et al.,* 2002. Immunization reverses memory deficits without reducing brain Aβ burden in Alzheimer's disease model. *Nature Neuroscience* 5, 452-457.
7. Bard, F, Cannon, C, Barbour, R, *et al.,* 2000. Peripherally administered antibodies against Aβ-peptide enter the central nervous system and reduce pathology in a mouse model of Alzheimer's disease. *Nature Med* 6, 916-919.

8. Kazatchkine, MD, Kaveri, SV, 2001. Immuno-modulation of autoimmune and inflammatory diseases with intravenous immune globulin. *N Engl J Med.* 345(10), 747-755.
9. Dalakas, MC., 2002. Mechanisms of action of IVIg and therapeutic considerations in the treatment of acute and chronic demyelinating neuropathies. *Neurology* 59(12 Suppl 6), S13-21.
10. Dodel, R, Hampel, H, Depboylu, C, *et al.*, 2002. Human antibodies against amyloid beta peptide: a potential treatment for Alzheimer's disease. *Ann Neurol.* 52(2), 253-256.
11. Bard, F, Cannon, C, Barbour, R, *et al.,* 2000. Peripherally administered antibodies against amyloid beta-peptide enter the central nervous system and reduce pathology in a mouse model of Alzheimer disease. *Nat Med.* 6(8), 916-919.
12. Lemere, CA, Spooner, ET, LaFrancois, J, *et al.,* 2003. Evidence for peripheral clearance of cerebral Aβ protein following chronic, active Aβ immunization in PSAPP mice. *Neurobiol Dis*. 14(1), 10-18.
13. Solomon, B, Koppel, R, Frankel, D, *et al.,* 1997. Disaggregation of Alzheimer beta-amyloid by site-directed mAb. *Proc Natl Acad Sci U S A*. 94(8), 4109-4112.
14. Frenkel, D, Katz, O, Solomon, B., 2000. Immunization against Alzheimer's beta -amyloid plaques via EFRH phage administration. *Proc Natl Acad Sci USA.* 97(21), 11455-11459.
15. Dodel, RC, Du, Y, Depboylu, C, *et al.,* 2004. Intravenous immunoglobulin's containing antibodies against beta-amyloid for the treatment of Alzheimer's disease. *J Neurol Neurosurg Psychiatry*. 75(10), 1472-1474.

16. Relkin, NR, Szabo, P, Adamiak, B, *et al.*, 2008. 18-Month study of intravenous immunoglobulin for treatment of mild Alzheimer disease. *Neurobiology of Aging*, in press.

17. McKhann, G, Drachman, D, Folstein, M, *et al.,* 1984. Clinical diagnosis of Alzheimer's-disease - report of the NINCDS-ADRDA Work Group under the auspices of Department of Health and Human Services task force on Alzheimers disease. *Neurolog.* 34, 939-944.

18. Hatzimanikatis, V, Choe, LH, Lee, KH., 1999. Proteomics: Theoretical and experimental considerations. *Biotechnol Prog*. 15, 312-318.

19. Milliken, GA, Dudley, AL, Sall, JP. Mixed Models Analysis Using JMP® Software 4.0. SAS Institute, Inc.

20. Finehout, EJ, Franck, Z, Lee, KH, 2004. Towards two-dimensional electrophoresis mapping of the cerebrospinal fluid proteome from a single individual. *Electrophoresis* 25, 2564-2575.

21. Finehout, EJ, Lee, KH., 2003. Comparison of automated in-gel digest methods for femtomole level samples. *Electrophoresis* 24, 3508-3516.

22. Perkins, DN, Pappin, DJ, Creasy, DM, Cottrell, JS., 1999. Probability-based protein identification by searching sequence databases using mass spectrometry data. *Electrophoresis* 20, 3551-3567.

23. NCBInr protein database, http://www.ncbi.nlm.nih.gov/entrez/query.fcgi?db=Protein &itool=toolbar. Last accessed 7/28/2005.

24. Harold, D, Abraham, R, Hollingworth, P, *et al.,* 2009. Genome-wide association study identifies variants at CLU and PICALM associated with Alzheimer's disease. *Nature Genetics* 41(10), 1088-1095.

25. Finehout, EJ, Frank, Z, Choe, L, *et al.,* 2007. Cerebrospinal fluid proteomic biomarkers for Alzheimer's disease. *Ann Neurol* 61, 120-129.

26. Zarghooni, M, Soosaipillai, A, Grass, L, *et al.,* 2002. Decreased concentration of human kallikrein 6 in brain extracts of Alzheimer's disease patients. *Clinical Biohchemistry* 35, 225-231.

27. Buxbaum, JN, Ye, Z, Reixach, N, *et al.,* 2008. Transthyretin protects Alzheimer's mice from the behavioral and biochemical effects of Aβ toxicity. *PNAS* 105, 2681-2686.

28. Sousa, JC, Cardoso, I, Marques, F, *et al.,* 2007. Transthyretin and Alzheimer's disease: Where in the brain? *Neurobiology of Aging* 28, 713-718.

29. Lee, KY, Lee, HS, Hong, JH, *et al.,* 2005. High-dose intravenous immunoglobulin down-regulates the activated levels of inflammatory indices except erythrocyte sedimentation rate in acute stage of Kawasaki Disease. *J Trop Pediatr*. 51(2), 98-101.

30. Gollin, PA, Kalaria, RN, Eikelenboom, P, *et al.,* 1992. Alpha-1-antitrypsin and alpha-1-antichymotrypsin are in the lesions of Alzheimer's-disease. *Neuroreport* 3, 201-203.

31. Puchades, M, Hansson, SF, Nilsson, CL, *et al.*, 2003. Proteomic studies of potential cerebrospinal fluid protein markers for Alzheimer's disease. *Brain Res Mol Brain Res.* 118, 140-146.

32. Yamagishi, S, Inagaki, Y, Takeuchi, M, Sasaki, N., 2004. Is pigment epithelium-derived factor level in cerebrospinal fluid a promising biomarker for early diagnosis of Alzheimer's disease? *Med Hypotheses*. 63(1), 115-117.

33. Qiao, H, Koya, RC, Nakagawa, K, Tanaka, H, Fujita, H, Takimoto, M, Kuzumaki, N., 2005. Inhibition of Alzheimer's amyloid-beta peptide-induced reduction of mitochondrial membrane potential and neurotoxicity by gelsolin. *Neurobiol Aging* 26(6), 849-855.

34. Matsuoka, Y, Saito, M, LaFrancois, J, Saito, M, Gaynor, K, Olm, V, *et al.,* 2003. Novel therapeutic approach for the treatment of Alzheimer's disease by peripheral administration of agents with an affinity to beta-amyloid. *J Neurosci.* 23(1), 29-33.

35. Chauhan, V, Ji, L, Chauhan, A., 2008. Anti-amyloidogenic, anti-oxidant and anti-apoptotic role gelsolin in Alzheimer's disease. *Biogerontology* 9, 381-389.

36. Yoshida, E, Yoshimura, M, Ito, Y, *et al.,* 1991. Demonstration of an active component of inter-α-trypsin inhibitor on the brains of Alzheimer type dementia. *Biochemical and Biophysical Research Communications* 174, 1015-1021.

37. Lee, JW, Namkoong, H, Kim, HK, *et al.*, 2007. Fibrinogen gamma-A chain precursor in CSF: a candidate biomarker for Alzheimer's disease. *BMC Neurology* 7, 1-6.

38. Loeffler, DA, Connor, JR, Juneau, PL, *et al.,* 1995. Transferrin and Iron in normal, Alzheimer's disease, and Parkinson's disease brain regions. *Journal of Neurochemistry* 65, 710-716.

39. Connor, JR, Menzies, SL, Martin, SM, *et al.,* 1992. A histochemical study of iron, transferrin, and ferritin in Alzheimer's diseased brains. *Journal of Neuroscience Research* 31, 75-83.

40. Finehout, EJ, Franck, Z, Lee, KH., 2005. Complement protein isoforms in CSF as possible biomarkers for neurodegenerative disease. *Disease Markers* 21, 93-101.

CHAPTER 9

CONCLUSIONS AND FUTURE WORK

9.1 Summary of Conclusions

The first objective of this research was to improve the utility of current *in vitro* blood-brain barrier (BBB) models for molecular transport studies by applying biochemical and nanofabrication techniques. Establishing a primary culture of brain microvascular endothelial cells (BMEC) is difficult and time intensive and therefore as a first attempt, bovine aortic endothelial cells were studied for the development of an *in vitro* BBB model. These cells are available commercially and they can be passaged while retaining their characteristic morphology. The aortic endothelial cells were co-cultured with primary rat astrocytes and model characterization studies including transendothelial electrical resistance (TEER), permeability of small molecules, and immunocytochemistry for the expression of tight junction proteins revealed that the endothelial cells are not an appropriate cell model for an *in vitro* BBB model. This led to studies to isolate BMEC from mouse brain and further co-culture them with primary rat astrocytes on commercially available polyester membranes with 400 nm pores. The isolation protocol is based on enzymatic digestion followed by density centrifugation steps. Moreover, biochemical additives such as puromycin, retinoic acid, cAMP, and hydrocortisone were used in a combinatorial fashion to ensure culture purity and barrier tightening. In contrast to contact co-cultures, the non-contact co-cultures showed astrocytic induction effects and produced a 98% drug permeability correlation coefficient with *in vivo* data from mouse.

In an attempt to assess the effects of membrane's physical parameters (chemistry, thickness, and pore size) on the co-cultures, custom 3 μm thick membranes based on poly(hydroxy styrene) (PHOST) were nanofabricated using electron beam lithography. As a first attempt to establish the lack of cytotoxicity, various cell lines were cultured on protein treated nanofabricated membranes and their attachment, proliferation, and differentiation were confirmed. Primary mouse BMEC and rat astrocytes were then co-cultured on membranes with 400 nm and 800 nm pores and model integrity was assessed using TEER and small molecule permeability. Once again, in contrast to contact co-cultures, the non-contact co-cultures showed astrocytic induction effects. These results indicate that astrocyte foot processes do not pass through 400 nm or 800 nm pores on a 3 μm thick PHOST membrane and may clog the pores to prevent the diffusion of soluble factors. On the other hand, the results indicate that the chemistry of the material has a significant effect on the physiological response of the cells.

The second objective of this research was to couple proteomics and statistical approaches to identify therapeutic targets of intravenous immunoglobulin (IVIg) in the cerebrospinal fluid (CSF) by analyzing samples from subjects with Alzheimer's disease (AD) who underwent IVIg immunotherapy. A detailed review was provided about active components of IVIg and its known disease-modifying mechanisms in autoimmune diseases. This review was followed by experimental examples of possible proteomics techniques, including immunoprecipitation with beads, one-dimensional, and two-dimensional westerns that may be utilized to understand how IVIg interacts with the CSF proteins in neurodegenerative disorders. Preliminary two-dimensional westerns indicated that IVIg may block the recognition of

some endogenous CSF antibodies and/or proteins by anti-human IgG. These results were then analyzed within the framework of immunology network theory, which concerns the ability of anti-idiotypes in IVIg to block autoantibodies and their inflammatory effects in autoimmune diseases.

Later, a Random Forest classification model was used to assess the potential use of IVIg as an immunotherapy for AD. CSF samples from AD subjects were analyzed using two-dimensional gel electrophoresis and further studied using a Random Forest classification model to identify effects of IVIg on a panel of 23 putative diagnostic AD biomarkers previously identified. The majority of the subjects showed improvements with respect to the 23 AD diagnostic biomarkers after six months of therapy compared to the samples taken before the trial. The observed improvements provide preliminary evidence regarding the potential use of IVIg as an AD immunotherapy.

Finally, in a separate study, CSF samples from the same group of AD subjects were analyzed to identify IVIg-induced changes. CSF samples collected at different time points (i.e. before the therapy, after six months of therapy, and after a three months drug washout period) were analyzed using a gel-based proteomics strategy and two different statistical approaches were used to identify IVIg-induced changes. The first analysis revealed sixty nine proteins that showed a considerable and consistent change during IVIg treatment. The second analysis identified 25 proteins that changed significantly after six months of therapy, and then the change was sustained or reversed during the washout period including Ig molecules, gelsolin, transferrin, transthyretin and other proteins. The proteins that showed a significant change during IVIg therapy have been previously implicated in AD and their direction of change at different time points is consistent with previous

reports in the literature. This study provides preliminary evidence regarding the potential group of CSF proteins that may be implicated in the treatment of AD.

9.2 Recommendations for Future Work

9.2.1 BMEC and Astrocyte Co-Cultures on Nanofabricated Membrane with Larger Pores

The co-culture results on commercial membranes and nanofabricated PHOST indicated that 400 nm or 800 nm pores are too small to promote the extension of astrocyte foot processes, and physical contact between the two cell types. These pore sizes are appropriate if the membranes are substantially thinner [1]. Due to the polymeric nature of PHOST, reducing its thickness from 3 μm will not be feasible because mechanical stability will be compromised. Therefore, a reasonable option is to employ photolithographic approaches to fabricate pores that are larger than 800 nm [2-4]. Although electron beam lithography can be used for this purpose, photolithography is more time efficient for high-throughput fabrication and is less expensive than electron beam lithography. However, this approach requires confirmation of the lack of cytotoxicity of the membranes to make sure that photolithography development solvents do not adversely affect the lack of cytotoxicity of the membranes. Alternatively different commercially available polymers such as polycarbonate or polyester may be used for nanofabrication. However, based on preliminary results polycarbonate creates translucent membranes which may not be suitable for microscopy.

9.2.2 Dynamic In vitro Model of the BBB

A major disadvantage of the static models of the BBB is the lack of physiologic shear stress due to the absence of intraluminal flow. The role played by intraluminal shear stress in BMEC differentiation, as well as maintenance and induction of a BBB phenotype is well recognized [5-13]. Therefore, it would be advantageous to transfer the co-cultures and biochemical techniques developed in this research to a dynamic model system.

Previous studies have already reported on the development of a dynamic *in vitro* BBB model based on a three-dimensional hollow fiber structure that enables co-culturing of EC with glial cells, with the endothelial cells exposed to shear stress [14]. However, none of these studies use primary brain endothelial cells. This dynamic model consists of variable number of hollow polypropylene fibers (capillaries) with trans-capillary pore size of 500 – 600 nm, inside a polycarbonate sealed chamber. The porosity of the hollow fiber allows gas and nutrient exchange between the two compartments but does not permit cells to pass (the wall thickness of each capillary is around 300 μm). Both compartments are accessible by ports in the circuit connected with a medium reservoir and a pulsatile pump apparatus.

Alternatively, microscale cell culture analog (μCCA), also known as ‘body-on-a-chip’ which is a microfluidic device to recreate various tissue environments in the body on a single chip, may be used for creating a dynamic BBB model. Brain EC, astrocytes, and possibly other neuronal or non-neuronal cell types can be cultured in separate chambers on a single chip, interconnected by channels mimicking the blood flow pattern [15-16]. Furthermore, this microfluidic system can be used for pharmacokinetics

studies of potential BBB drug targets while possibly incorporating other tissues in the body.

9.2.3 Understanding the Disease-Modifying Effects of IVIg in AD

Chapters 6-8 provided background on how proteomics approaches can be employed to identify protein targets of IVIg in CSF as well as a list of biomarkers that respond to IVIg therapeutically. IVIg is administered intravenously and thus some of its components, if not all, may be crossing the BBB. The static or dynamic *in vitro* model of the BBB can be a useful platform technology to study the pharmacodynamics of IVIg. Similar to a drug permeability study, IVIg may be added to the luminal compartment and the protein content of the abluminal compartment may be analyzed at various time points using mass spectrometry and compared to a control abluminal composition.

Chapter 8 provided a list of 25 IVIg induced biomarkers in the CSF of AD subjects. A simplified experimental approach to couple these results with *in vitro* data may be to first analyze the expression of these biomarkers in the abluminal compartment using ELISA or mass spectrometry. IVIg may then be added to the luminal compartment and possible changes in the amount of expression of these biomarkers will be studied using proteomics approaches.

9.3 Conclusion

This project has focused on two areas: development of a new *in vitro* model of the BBB based on a co-culture between primary mouse brain endothelial cells and astrocytes coupled with biochemical interventions and nanofabrication techniques, and identification of therapeutically relevant protein targets of IVIg

in the CSF of AD subjects. The BBB studies provide a comprehensive framework on the importance of using primary cultures as well as additional biochemical interventions that may be employed to improve barrier properties. The static model provides new opportunities to transfer the model components into a dynamic system in order to develop a more physiologically-based and authentic *in vitro* model. Furthermore, the studies on nanofabricated materials open doors to a more detailed characterization of cellular responses to nanopores. The second part of this thesis provides examples on how proteomics approaches coupled with advanced statistical modeling can be used to identify therapy induced biomarkers in the CSF. While the studies were mainly based on gel-based proteomics approaches, newer approaches such as shotgun proteomics can be coupled with these techniques to obtain a more comprehensive list of biomarkers. Together, these studies have proven the utility of proteomics for the diagnosis and treatment of AD, and possibly other neurodegenerative disorders.

REFERENCES

1. Harris Ma, S., Lepak, L.A., Hussain, R.J., Shain, W., Shuler, M.L., 2005. An endothelial and astrocyte co-culture model of the blood-brain barrier utilizing an ultra-thin, nanofabricated silicon nitride membrane. *Lab on a Chip* 5, 74-85.
2. Li, M., Douki, K., *et al.,* 2004. Spatially controlled fabrication of nanoporous block copolymers. *Chem. Mater*. 16, 3800-3808.
3. Ober, C.K., Li, M., *et al.*, 2003. Lithographic patterning with block copolymers. *J. Photopolym. Sci. Technol*. 16, 347.
4. Du, P., Li, M., Douki, K., *et al.*, 2004. Additive-driven phase-selective chemistry in block copolymer thin films: the convergence of top-down and bottom-up approaches. *Adv. Mater*. 16, 953.
5. Ando, J., Kamiya, A., 1996. Flow-dependent regulation of gene expression in vascular endothelial cells. *Jpn. Heart J*. 37, 19-32.
6. Ballermann, B.J., Ott, M.J., 1995. Adhesion and differentiation of endothelial cells by exposure to chronic shear stress: a vascular graft model. *Blood Purif.* 13, 125-134.
7. Brooks, A.R., Lelkes, P.I., *et al.*, 2004. Gene expression profiling of vascular endothelial cells exposed to fluid mechanical forces. *Endothelium* 11, 45-57.
8. Desai, S.Y., Marroni, M., *et al.*, 2002. Mechanisms of endothelial survival under shear stress. *Endothelium* 9, 89-102.
9. Krizanac-Bengez, L., Kapural, M., *et al.*, 2003. Effects of transient loss of shear stress on blood-brain barrier endothelium: role of nitric oxide and IL-6. *Brain Research* 977, 239-246.

10. Lin, K., Hsu, P.P., *et al.*, 2000. Molecular mechanism of endothelial growth arrest by laminar shear stress. *PNAS* 97, 9385-9389.
11. McAllister, M.S., *et al.*, 2001. Mechanisms of glucose transport at the blood brain barrier: an *in vitro* study. *Brain Research* 904, 20-30.
12. Ott, M.J., Ballermann, B.J., 1995. Shear stress-conditioned endothelial cell-seeded vascular grafts: improved cell adherence in response to *in vitro* shear stress. *Surgery* 117, 334-339.
13. Wasserman, S.M., Topper, J.N., 2004. Adaptation of the endothelium to fluid flow: *in vitro* analysis of gene expression and *in vivo* implications. *Vasc. Med*. 9, 35-45.
14. Santaguida, S., Janigro, D., *et al.*, 2006. Side by side comparison between dynamic versus static models of blood-brain barrier *in vitro*: A permeability study. *Brain Research* 1109, 1-13.
15. Esch, M.B., Sung, J.H., Shuler, M.L., 2010. Challenges, promises and future directions of μCCAs. *Journal of Biotechnology*, in press.
16. Sung, J.H., Kam, C., Shuler, M.L., 2010. A microfluidic device for a pharmacokinetics-pharmacodynamic (PK-PD) model on a chip. *Lab on a Chip* 10, 446-455.